UNIVERSITY OF CALIFORNIA,
IRVINE

Ion cyclotron emission on the DIII-D tokamak

DISSERTATION

submitted in partial satisfaction of the requirements
for the degree of

DOCTOR OF PHILOSOPHY

in Physics

by

Genevieve H. DeGrandchamp

Dissertation Committee:
Professor William W. Heidbrink, Chair
Professor Zhihong Lin
Professor Roger D. McWilliams

2022

DEDICATION

To Mom, Papa, and Giselle

TABLE OF CONTENTS

LIST OF FIGURES

LIST OF TABLES

ACKNOWLEDGMENTS

Foremost, I would like to thank my advisor Prof. Bill Heidbrink for his tutelage, instilling in me his holistic, pragmatic approach to experimental science. I have very much appreciated the opportunity to pursue a project at a national facility and have enjoyed unwavering support in doing so. I am grateful to my committee members Profs. Zhihong Lin and Roger McWilliams for their time and careful thought in revising this work. I would also like to thank Jan Strudwick and My Banh for their aid throughout this process. Finally, many thanks to my fellow group members Kenny Gage, Daniel Lin, Alvin Garcia, Wataru Hayashi, and Garrett Prechel.

I've been fortunate to work with a myriad of excellent scientists at DIII-D. Along with imparting vast amounts of technical knowledge (alongside healthy amounts of skepticism), Jeff Lestz, Xiaodi Du, Kathreen Thome, Bob Pinsker, Mike Van Zeeland, Tsuyoshi Akiyama, and Deyong Liu in particular have served as invaluable mentors, and I look forward to continued collaboration.

I would also like to thank Ian Holmes, Jim Kulchar, David Pace, Rick Lee, and Matt Wolde, without whom the diagnostic in this work would not exist. They have fielded my many questions with enthusiasm and made the machine hall a welcoming place, even in the face of two separate major water leaks. A special thanks goes to Will Carrig, who fast became a friend and mentor upon my arrival at DIII-D. He will be greatly missed, and his love of classic rock and audiobooks carried on.

I am very grateful for the friendship of my fellow anteaters Astrid, Jessica, Abby, Eric, Haytham, Ed, and Mike. I am also very fortunate for William, Becky, Ryan, Jessica, Jessica, Nathan, Shira, Igor, Shawn, and the rest of my San Diego posse. Aside from keeping me sane through various moves and COVID lockdowns, they have made California a home.

And finally, I would like to thank my family, whose love and support have enabled and emboldened me to pursue this degree.

This material is based upon the work supported by the U.S. Department of Energy, Office of Science, Office of Fusion Energy Sciences, using the DIII-D National Fusion Facility, a DOE Office of Science user facility, under Award Nos. DEFC02-04ER54698, DE-SC0018270, and DE-SC0021201.

Discussion from previously published works is presented in Chapter 3 (reproduced from [46]) with permission from AIP Publishing), as well as in Chapter 4 and Appendix B (reproduced from [45] with permission from IOP Publishing). Work in preparation for submission is presented in Chapter 5 [44].

CURRICULUM VITAE

Genevieve H. DeGrandchamp

Genevieve H. DeGrandchamp — Curriculum Vitae

University of California, Irvine
Ph.D. Physics, 2022
Advisor: W.W. Heidbrink

University of Colorado, Boulder
B.S. Engineering Physics, 2017

Research Experience

University of California, Irvine
Graduate Student Researcher **Mar. 2018–Dec. 2022**

Thesis topic: Ion cyclotron emission (ICE) on the DIII-D tokamak

- Upgraded and provided routine maintenance for ICE diagnostic on DIII-D
  - Designed new poloidal loop assembly, installed new poloidal and toroidal loops in-vessel, and implemented high-speed digitizer
  - Configured high-frequency ICE (HICE) to measure lower-hybrid frequencies, including injected helicon waves and associated parametric decay instabilities
  - Provided routine ICE diagnostic support, including data acquisition for high-frequency runaway electron experiments and support for the refurbished fast-wave interferometer/reflectometer system
- Designed and participated in various DIII-D experiments
  - Designed and served as session leader for half-day ICE mode structure experiment
  - Served as diagnostic coordinator for 2021 Frontier science experiment
- Analyzed neutron blip fitting data to determine deuterium concentration of mixed species plasmas from 2021 DIII-D isotope campaign and Frontier science experiments

ITER International School: Plasma Scenarios and Control
Student **Jul. 2022**

PPPL Graduate Summer School
Student **Aug. 2019**

Tech-X Corporation
Intern **May 2017–Sept. 2017**

- Revised documentation for VSim particle-in-cell electromagnetics and plasma simulation code
- Made 3D model of customer designed microwave device, using VSim for troubleshooting

Boulder Environmental Sciences and Technology
Intern **May 2016–May 2017**

- Modeled passive remote sensing radiometer behavior in atmosphere using radiative transfer code
- Performed statistical analysis of radiometer data

Skills

Laboratory: RF instrumentation, including basic usage of vector network analyzer and spectrum analyzer
Software: Python, IDL, MATLAB, LaTeX; OMFIT, TRANSP, FIDASIM; SolidWorks

Awards and Scholarships

USBPO Travel Scholarship for 11th ITER International School	2020
University of Colorado Esteemed Scholars President Joseph A. Sewall Award	2013–2017
Engineering Merit Scholarship (Gillespie Scholarship Fund)	2013–2017

Outreach

Science and Technology Education Partnership Conference	Aug. 2021–Oct. 2021
	July 2020–Oct. 2020
American Association of University Women Tech Trek	June 2021–July 2021
UC Irvine Physics & Astro Blog Team	Dec. 2017–Aug. 2018
Partnerships for Informal Science Education in the Community	Aug. 2014–Dec. 2014

Publications and Conference Papers

G.H. DeGrandchamp et al., "Ion cyclotron emission dependence on the evanescent layer on the DIII-D tokamak," ***In preparation***

G.H. DeGrandchamp et al., "Mode structure measurements of ion cyclotron emission and sub-cyclotron modes on DIII-D," ***Nuclear Fusion*, 62(10):106033, 2022**

G.H. DeGrandchamp et al., "Upgrades to the ion cyclotron emission diagnostic on the DIII-D tokamak," ***Review of Scientific Instruments*, 92(3):033543, 2021**

N.A. Crocker et al., "Novel internal measurements of ion cyclotron frequency range fast-ion driven modes," ***Nuclear Fusion*, 62(2):026023, 2022**

T. Akiyama et al., "Fast wave interferometer for ion density measurement on DIII-D," ***Journal of Instrumentation*, 17(01):C01052, 2022**

W.W. Heidbrink et al., "Isotope dependence of beta-induced Alfvén eigenmode (BAE) and low frequency mode (LFM) stability in DIII-D," ***Nuclear Fusion*, 61(10):106021, 2021**

S.R. Haskey et al., "Radially resolved active charge exchange measurements of the hydrogenic isotope ratios on DIII-D," ***Review of Scientific Instruments*, 92(4):043535, 2021**

Selected Conference Presentations

G.H. DeGrandchamp et al., "Mode structure measurements of ion cyclotron emission and sub-cyclotron modes on DIII-D," **Contributed Oral, APS-DPP, 2022**

G.H. DeGrandchamp et al., "Characterization of ion cyclotron emission in the DIII-D tokamak," **Invited Oral, IAEA EP Technical Meeting, 2021**

G.H. DeGrandchamp et al., "Characterization of ion cyclotron emission in L- and H-mode plasmas on the DIII-D tokamak," **Poster, APS-DPP, 2021**

W.W. Heidbrink et al., "Low frequency instabilities and Alfvén eigenmodes in mixed species DIII-D plasmas," **Contributed Oral, APS-DPP, 2021**

B.G. Van Compernolle et al., "Commissioning and first results of the DIII-D helicon system," **Contributed Oral, APS-DPP, 2021**

G.H. DeGrandchamp et al., "Upgrades to the high-frequency ion cyclotron emission (ICE) diagnostic on DIII-D," **Poster, HTPD, 2020**

G.H. DeGrandchamp et al., "Ion species mix, magnetic field, and distribution function dependence of instabilities in the ion cyclotron range of frequencies," **Poster, IAEA EP Technical Meeting, 2019**

ABSTRACT OF THE DISSERTATION

Ion cyclotron emission on the DIII-D tokamak

By

Genevieve H. DeGrandchamp

Doctor of Philosophy in Physics

University of California, Irvine, 2022

Professor William W. Heidbrink, Chair

Diagnosis of the fast ion population, which is necessary for heating but can drive dangerous instabilities, is crucial in achieving and maintaining a burning plasma regime. Present fast ion diagnostic methods tend to rely on delicate components unlikely to survive in a reactor environment, motivating exploration into alternative diagnostic methods. One candidate, the subject of this thesis, entails measurement of collective ion cyclotron emission (ICE) spectra via robust magnetic pickup loops integrated with the first wall, making it potentially compatible with ITER and other reactor-relevant devices [116, 69]. ICE, distinct from thermal electron cyclotron emission, manifests as narrowband peaks at harmonics of the ion cyclotron frequency f_{ci} and is generally localized near the core or the edge of the plasma. These modes have been observed to be sensitive to the fast ion population, be they introduced by auxiliary heating systems or fusion products. However, the connection between observed ICE spectra and the fast ion population has not been sufficiently established, meriting diagnostic upgrades and dedicated experiments.

This work aims to characterize ICE mode structure and fine-scale phenomena in L- and H-mode plasmas on DIII-D using the ICE diagnostic, which was recently upgraded to include additional channels and consequently new measurement capabilities. In addition to basic frequency and amplitude information, measurements of mode polarization at the plasma edge,

amplitude as measured at the centerpost and outer wall of the machine, and toroidal mode number are now possible and will be demonstrated through this work. Additionally, mode sensitivity to the vacuum region, plasma shape, and particularly the fast ion distribution is explored. The detailed mode structure measurements and phenomenology presented in this work can be used to test and validate theoretical models en route to developing a more complete physical understanding of ICE, so that it can be leveraged as a passive fast ion diagnostic in future burning plasmas.

The outline of this thesis is as follows: an overview of fusion and fast ion studies in particular is outlined in Chapter 1, followed by an overview of ICE research (Chapter 2). The experimental setup used in this thesis follows in Chapter 3, which includes both an overview of the DIII-D tokamak and the ICE diagnostic. Initial measurements of mode structure are presented in Chapter 4, providing the basis for evanescent layer and frequency splitting investigations presented in 5. Conclusions, discussion, and an outlook for ICE research are provided in Chapter 6.

Chapter 1

Introduction

The recent slew of natural disasters, including the ever-present drought here in San Diego, CA, serve as a reminder that our reliance on fossil fuels must cease. Research into renewable energy sources has made great strides in recent decades, with wind and solar becoming commercially viable on a small-scale basis. However, these energy sources are generally dependent on weather conditions and/or terrain, and the grid-scale battery storage capabilities necessary to make them competitive as baseline power solutions have yet to be developed. Nuclear fission boasts a high energy production density and is indifferent to daily weather fluctuations, but the highly radioactive waste it produces requires strict regulation. Further, high-profile accidents such as those at Cherynobyl, Three-Mile Island, and Fukushima Daiichi have tainted public perception and have made zoning significantly more difficult. At present, there is no clear option that can largely replace declining fossil fuel reserves.

Nuclear fusion represents a possible alternative, which may have the requisite high energy output to be a baseline energy source and is indifferent to the environment, similar to fission. The two-part fuel required for fusion reactions can be generated from sea-water and bred in the machine environment, and the ensuing radioactive products are not long-lived. However,

achieving terrestrial fusion requires taming a multiscale, nonlinear system through advanced physics, engineering, and diagnostic solutions.

1.1 Fusion energy

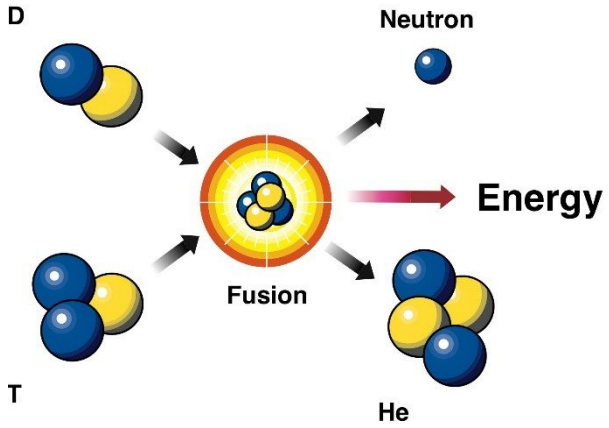

Figure 1.1: D-T fusion reaction whereby 3 MeV α particles and 14 MeV neutrons are produced. Figure taken from [52].

Nuclear fusion is in essence the opposite reaction to nuclear fission. For light atomic particles (e.g., those lighter than iron or nickel), energy is released when nucleons are combined to form larger nuclei. This process requires the constituent particles' kinetic energies to overcome the Coulomb force that would otherwise repel like charges, after which the strong nuclear force takes over. The resultant particles have a lower combined mass than the input particles and, most importantly, higher kinetic energies. However, not all fusion reactions are equally

D + D	$\longrightarrow$ (50%)	0.8 MeV ^{3}He	+	2.4 MeV n
	$\longrightarrow$ (50%)	1.0 MeV T	+	3.0 MeV p
D + ^{3}He	$\longrightarrow$	3.7 MeV α	+	14.6 MeV p
D + T	$\longrightarrow$	3.5 MeV α	+	14.0 MeV n

Table 1.1: Main fusion reactions encountered in a tokamak environment. Table taken from [138].

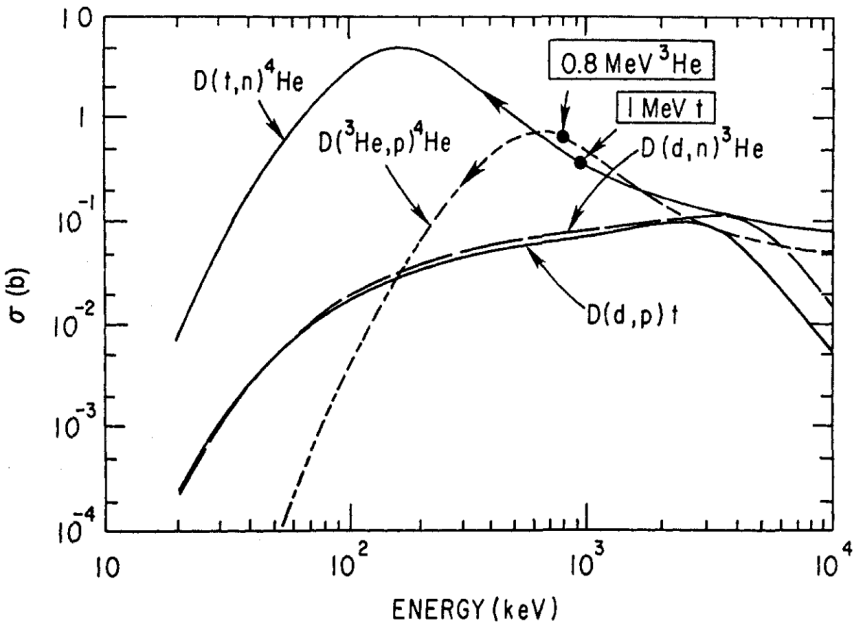

Figure 1.2: Cross section vs. energy for the hydrogenic fusion reactions listed in Table 1.1. Figure taken from [82].

accessible. The most commonly observed fusion reactions are listed in Table 1.1. The cross-section, a measure of the likelihood of fusion occurring for particles at a given kinetic kinetic energy, is presented for each combination in Fig. 1.2, and the D-T reaction is clearly favorable as it has the largest cross-section at the lowest energies. However, D-T fusion experiments are rare as the use of D-T fuel results in a radiated environment and tritium itself is scarce. Instead, many high-performing experiments use pure deuterium plasmas.

In the sun's core, immense gravitational forces confine particles, giving rise to temperatures in excess of 15 million C and pressures of roughly 265 billion bar and as a result, self-sustaining fusion reactions. As gravity cannot be leveraged in man-made devices, two alternate approaches have been developed: inertial and magnetic confinement. Inertial confinement fusion exists in the high-energy density regime, relying on high-intensity lasers to heat and compress partially frozen hydrogen particles contained in a small capsule called a hohlraum [99]. This sudden reaction relies on fusion to occur before the fuel in the target has time to disperse, hence the term "inertial" confinement. Magnetic confinement fusion

(MCF), which is the method of interest in this work, relies on magnetic fields to confine hot plasmas typically comprising heavy hydrogen isotopes listed in Table 1.1. For terrestrial fusion, the aim is to optimize the plasma such that fusion reactions are self-sustaining and auxiliary heating can be turned off, a point deemed "ignition." J. Lawson famously developed an ignition criterion by considering power balance (i.e., input vs. output power in the face of losses like those from bremsstrahlung radiation) in D-T tokamak plasmas [100]. This initial condition was dependent on both the density and energy confinement time of the plasma[1]. Since, criteria more specifically applicable to both inertial and magnetic confinement schemes have been developed.

Assessing ignition criteria for inertial confinement schemes is a difficult endeavor, as measurements are scarce and power balance is particularly difficult to ascertain. To the former point, currently few measurements can be made of the fuel assembly, namely the hot spot ion temperature T_i^h, total areal density ρR_{tot}, and neutron yield [1, 182]. Most other parameters must be inferred and/or simulated. Phenomena such as hydrodynamic instabilities in the capsule further complicate power balance assessments. Multiple ignition criteria have been devised to account for (or ignore) various factors, one being the generalized Lawson criterion [1, 108] that is given by:

$$\text{GLC}_\text{L} = \frac{\bar{P}_\text{HS}}{420\ \text{Gbar}} \frac{\bar{R}_\text{HS}}{50\ \mu\text{m}} \tag{1.1}$$

A value of $\text{GLC}_\text{L} > 1$ here indicates ignition and depends on the time-averaged hotspot pressure $\bar{P}_\text{HS}$ and radius $\bar{P}_\text{HS}$. This regime was reached in recent experiments at the National Ignition Facility (Fig. 1.3), in which 2.05 MJ of laser power was deposited on a target and yielded a record 3.15 MJ of output energy on a time scale of $\mathcal{O} \lesssim 10$ ns [1, 166][2].

[1]Lawson did not account for plasma self-heating, which is anticipated to be non-negligible.

[2]It is worth noting, as may be evident by the 322 MJ of energy consumed by NIF's 192 lasers in pursuit of this result, that NIF is not efficient nor intended to be a fusion energy device [166]. While these findings may help inertial fusion to become viable path, these experiments were instead intended to inform the national stockpile research program.

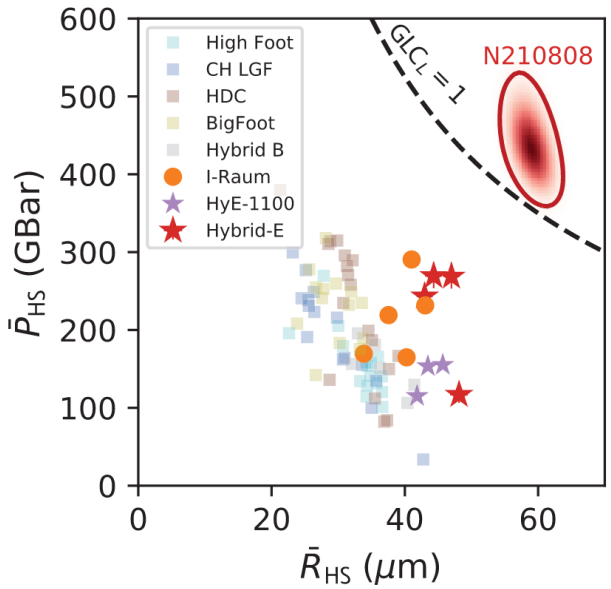

Figure 1.3: Probability distribution for time-averaged hotspot pressure and radius for the NIF DT record shot N210808 (red ellipse at top right of figure), compared with data calculated from previous experiments. The distribution lies above the curve delineating the generalized Lawson criterion(black dashed line). Figure taken from [1].

In contrast, the main ignition criterion commonly cited in tokamak research, known as the triple product, can be expressed as [176]:

$$\hat{n}\tau_E\hat{T} > 5 \times 10^{21} \text{ m}^{-3} \text{ s keV} \tag{1.2}$$

where the peak ion density ($\hat{n}$), peak ion temperature ($\hat{T}$)[3], and energy confinement time (τ_E) must be considered (and thankfully can be routinely measured). This latter quantity is given by:

$$\tau_E = \frac{W}{P_{\text{lost}}} \tag{1.3}$$

where $W = 3\overline{nT}V$ is the total energy of the plasma of a certain volume (V) and P_{lost} is the rate of energy loss [176].

In practice, there must be balance between $\hat{n}$, $\hat{T}$, and τ_E. For example, though raising

[3]Note, temperatures are typically converted from K to eV via multiplication by the Boltzmann constant, $k_B = 1.38 \times 10^{-23}$ m^2 kg s^{-2} K^{-1}.

density would nominally increase fusion output, high density regimes can be difficult to heat to high enough temperatures where fusion reactions are most likely (Fig. 1.2). To date, sufficiently high values of all three of these quantities have not been achieved simultaneously, and P_{lost} is generally equivalent to the auxiliary heating power. Tokamaks have yielded the best performance out of all MCF devices, with the JET[4] tokamak recently achieving a record 59 MJ of total fusion energy (10 MW of fusion power sustained for 5 seconds) with a D-T plasma [42, 67, 87] and a value of Q = 0.33 (which is the ratio of input to output power) [67][5]. The general concept of the tokamak is presented in the following section, and specific details regarding the DIII-D tokamak used in this work can be found in Chapter 3.1.1.

1.2 The tokamak

In the presence of a magnetic field, charged particles will orbit around the magnetic field lines with what is called a cyclotron frequency

$$\omega_{cs} = \frac{|q|B}{m} \tag{1.4}$$

and a gyroradius (or Larmor radius) of

$$\rho_s = \frac{mv_\perp}{|q|B} \tag{1.5}$$

where q is the particle charge, B the magnetic field strength, m the particle mass, $v_\perp$ the perpendicular velocity component, and the subscript s is used to denote the particle species. Tokamaks (as illustrated in Fig. 1.4) generate a strong toroidal magnetic field ($\overrightarrow{B_\phi}$) by running

[4]Note, a list of common expressions and acronyms can be found in Appendix A for convenience, particularly as many device names may not be clarified in the text.

[5]As of yet, figures for peak density, temperature, and energy confinement from this record experiment have yet to be published. Previously, the closest a tokamak has gotten to scientific breakeven was in 1997, when a triple product of $n_{DT}(0)\tau_E^{\text{dia}}T_i(0) = 8.7 \times 10^{20} \pm 20\%$ m^{-3} s keV was achieved and maintained for roughly $0.5\tau_E$ in a JET D-T plasma that yielded 16.1 MW of output power [89].

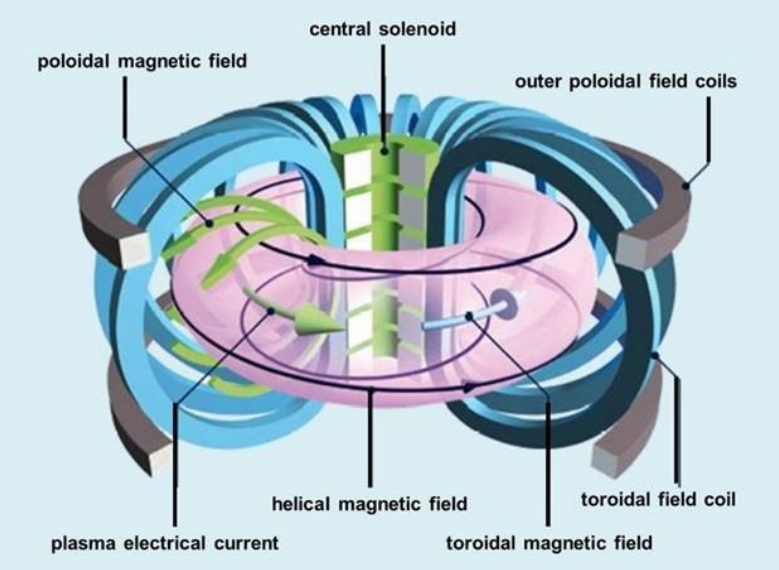

Figure 1.4: Basic concept of a tokamak, where the toroidal and poloidal field coils (grey and blue) work with the central solenoid (green) to produce helical magnetic fields (black arrows) that contain the plasma (pink). Figure taken from [53].

current through large external toroidal field coils (Fig. 1.4, blue) to confine the particles in a toroidal region (pink). However, this field alone is insufficient to contain particles in the plasma, as the combination of the magnetic field (oriented radially outward) and the pressure gradient $\overrightarrow{\nabla p}$ (pointed in the toroidal direction) means that diamagnetic currents, which can be expressed as:

$$\overrightarrow{j_D} = -\frac{\overrightarrow{\nabla p} \times \overrightarrow{B}}{qB^2} \tag{1.6}$$

will form. The current on the inboard side tends to be stronger, leading to charge separation and a vertical electric field $\overrightarrow{E}$. This electric field gives rise to $\overrightarrow{E} \times \overrightarrow{B}$ drifts,

$$\overrightarrow{v_E} = \frac{\overrightarrow{E} \times \overrightarrow{B}}{B^2} \tag{1.7}$$

which push the particles radially outward. Twisting the magnetic field lines eliminates this issue by allowing the particles to flow through both the upper and lower half of the torus, negating the $\overrightarrow{E} \times \overrightarrow{B}$ drift. Tokamaks use a central solenoid to twist the magnetic field lines. The solenoid acts like the primary winding in a transformer, where the plasma is the second

winding. By changing the flux in the solenoid, a toroidal current and a poloidal magnetic field ($\overrightarrow{B_p}$) is introduced in the plasma. This toroidal current also serves to heat the plasma in the early stages of plasma formation.

However, plasma resistivity declines with temperature ($\propto T_e^{-3/2}$), so ohmic heating must be augmented with auxiliary heating techniques[6]. One major heating mechanism in modern devices is neutral beam injection (NBI), whereby ions are produced and accelerated to high energies (typically $50 \sim 95$ keV on DIII-D) before being neutralized. These neutral particles do not respond to the magnetic field and are able to penetrate deep into the plasma before becoming fast ions, either through charge exchange or ionization (via collisions with ions or electrons). The fast ions created through NBI, or "beam ions", that are of primary concern in this work are born with a specific energy and pitch relative to the magnetic field ($v_\parallel/v$). These ions subsequently transfer energy to the thermal ion and electron populations through Coulomb collisions.

Radiofrequency (RF) waves are also used to both heat the plasma and drive current. Rather than relying on collisional heating, RF techniques employ resonant heating whereby electromagnetic waves are generated by a high-power source, travel through low-loss transmission lines, and are either injected directly or coupled via antennae built into the first wall. These waves are then absorbed in a target region in the plasma. Ion cyclotron resonance heating (ICRH) and electron cyclotron resonance heating and/or current drive (ECRH/ECCD) involve launching waves at harmonics of the ion or electron cyclotron frequencies, which serves to accelerate the particles as they gyrate around field lines [129]. The other main heating mechanism is Landau damping [129], where the wave must have an electric field component in the same direction as the particle's velocity. Lower hybrid current drive (LHCD) and helicon heating/current heat using this mechanism[7]. Particles subjected to RF heating do

[6]On the DIII-D tokamak, for example, ohmic heating gets the plasma to roughly 10 million degrees C, 10% of the ∼100 million degrees needed for fusion.

[7]Wave-particle interactions and collisions complicate this picture, requiring the use of quasilinear theory.

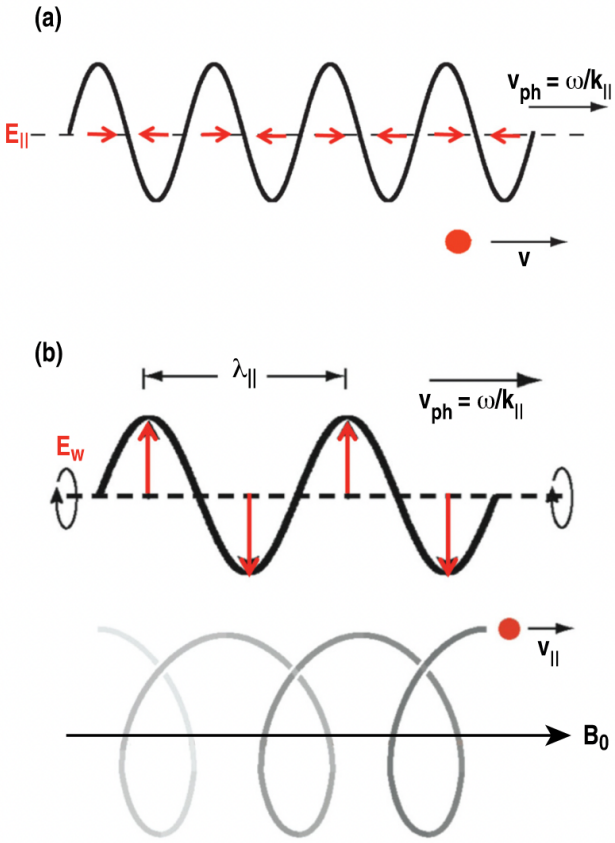

Figure 1.5: (a) Landau interaction, where energy can be passed between a particle of velocity v and a wave with an electric field in that same direction, and (b) cyclotron interaction between a particle gyrating around a magnetic field line and a wave with non-zero perpendicular wave vector such that the resonance condition $\omega - k_{\|} v_{\|} = l\omega_{ci}$ is satisfied. Figure taken from [129].

not have "birth" energy like their NBI contemporaries but still introduce a fast tail into the general distribution function. Both NBI and RF heating mechanisms result in anisotropic particle distribution functions, in contrast to fusion products, which are peaked in the core of the plasma and largely isotropic [82].

Though the energetic particle (EP) populations (be they created through auxiliary heating systems or fusion products) are necessary for plasma heating, they introduce new physics that must be treated separately from thermal populations. A major concern is that they can destabilize instabilities and be expelled from the plasma, which at best means a waste of heating power and a cooler plasma. At worst, ejected fast particles can damage plasma-

facing components [55, 66]. As such, understanding EP behavior is an active area of study in fusion research, and it is within the particular scope of fast ion physics that this thesis dwells[8].

1.3 Fast ions

Fast ions can stabilize or destabilize a variety of plasma waves (some of which are depicted in Fig. 1.6), depending on whether gradients in the fast ion distribution function are positive or negative. This energy exchange can only occur when there is an electric field component to the wave that aligns with the particle velocity and overall imparts a net force during each orbit, i.e., $\overrightarrow{v} \cdot \overrightarrow{E} \neq 0$. Generally, this resonance between the wave and a particle in a tokamak over the course of an orbit is given by[9]:

$$\omega - n\langle\omega_\phi\rangle - p\langle\omega_\theta\rangle = l\langle\omega_{ci}\rangle \tag{1.8}$$

where ω is the frequency of the instability; ω_ϕ the frequency of toroidal motion (or bounce frequency); ω_θ the frequency of poloidal motion; ω_{ci} the ion cyclotron frequency, and n, p, and l integers. The integer n, which in a tokamak geometry is known as the toroidal mode number, is defined as

$$n = \frac{k_\phi}{R} \tag{1.9}$$

where R is the radius and k_ϕ the toroidal wavenumber of the plasma wave. If this condition is satisfied, the change in particle canonical toroidal momentum $P_\zeta = mrv_\phi + qrA_\phi$ can be expressed as [30]:

$$\Delta P_\zeta = (n/\omega)\Delta E \tag{1.10}$$

[8]Runaway electrons are also of great concern and have been known to cause damage in tokamaks [114] but are not explored in this work.

[9]This orbit-averaged resonance condition applies to "slow" instabilities, whose growth rates are much lower than the frequency of the mode, i.e., $\gamma << \omega_\phi$. "Fast" or local resonance is explored in Chapter 2.2.1.

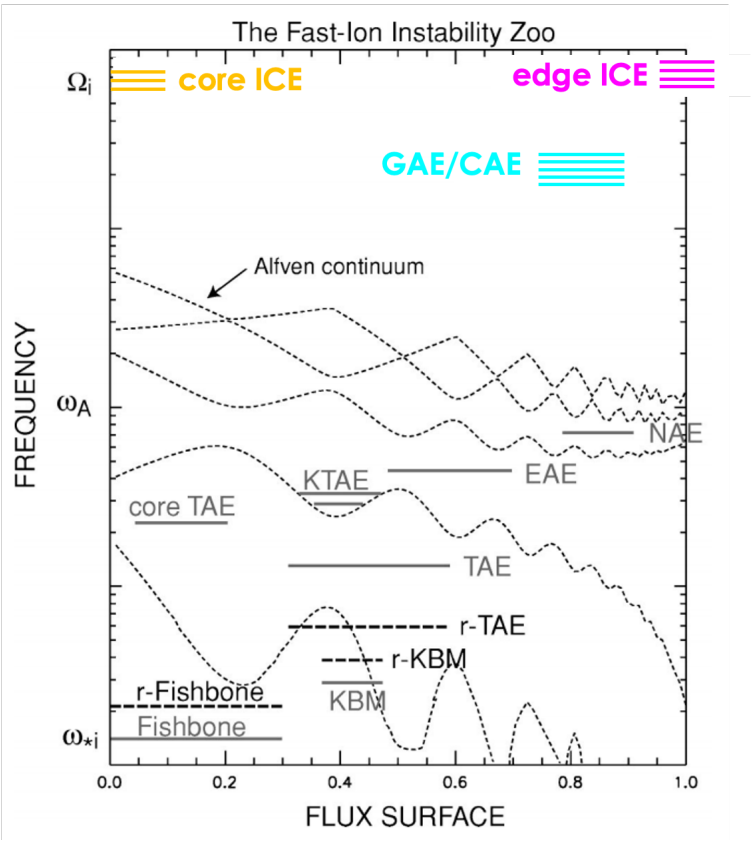

Figure 1.6: EP modes observed in tokamaks in terms of approximate frequency, location, and mode width. Of particular interest in this work are high-frequency modes such as CAEs and ICE. Figure taken from [77].

where ω is the wave frequency and ΔE the particle energy.

Much focus in the EP community is given to low-frequency instabilities (such that $l \simeq 0$ in Eq. 1.8) that can drive significant spatial fast ion transport [**?** 83]. In these cases, a low wave frequency ω results in large ΔP_ζ that manifests as radial transport.

However, there also exist innocuous EP-driven instabilities that may be leveraged for diagnostic purposes. These modes occur at high enough frequencies that ΔP_ζ is small, meaning negligible spatial transport[10]. Thus, the presence of these instabilities is not deleterious for the plasma, and the observed spectra are directly dependent on the fast ion population. One such mode is coherent ICE, a collective phenomenon wherein narrow peaks are excited at

[10]Though negligible spatial transport is suspected for ICE, this has yet to be proven experimentally.

ion cyclotron frequency (f_{ci}) harmonics of an energetic ion population.

Contrary to many other fast ion diagnostic techniques that rely on sensitive components like scintillating plates or cameras, ICE can be measured via robust magnetic pickup loops integrated with the first wall and so may be compatible with the harsh radiation environments in ITER and other reactor relevant devices [69, 116]. Historically, both measurement and modeling of ICE have been somewhat stymied by technological limitations, but the advent of ample data storage and computational power have recently reinvigorated ICE research. In the former case, advanced digitizers and room for requisite data storage has enabled simultaneous high temporal and frequency resolution, and increased computational power has facilitated analysis of the measured signal. For modeling, high-performance computer clusters have enabled theoretical models to advance beyond analytical descriptions and into linear and even nonlinear models. Even still, our current understanding of ICE is insufficient to extrapolate information about the fast ion population from observed ICE spectra alone, and both further experimental observations and modeling efforts are required. This thesis concerns the former, implementing upgrades to the ICE diagnostic on the DIII-D tokamak in an effort to better characterize ICE modes and provide constraints for future simulation efforts.

The outline of this thesis is as follows: a general background of ICE is provided in Chapter 2, followed by the a description of the DIII-D tokamak and the upgraded ICE diagnostic in Chapter 3. Initial measurements of ICE mode structure are presented in Chapter 4, and investigations into fine splitting and the effect of the evanescent layer width in Chapter 5. The work is summarized and potential future directions are detailed in Chapter 6.

Chapter 2

Ion cyclotron emission

Anticipated in magnetic confinement devices as early as 1959 [76], ICE[1] has been seen in both MCF devices (including tokamaks [18, 24, 37, 54, 56, 61, 92, 101, 130, 162], and stellarators [142, 147]) and space plasmas [7, 48]. Four general categories of ICE have been observed: fusion product ICE, beam-driven ICE, minority ICE, and core ICE, and all are typically localized either in the core of the plasma or near the last closed flux surface (LCFS)[2]. Mode frequency has been observed to depend on magnetic field strength, but no direct frequency dependence on density has been reported.

Interest in ICE as a potential diagnostic tool in tokamaks piqued following observations of spectral peaks corresponding to cyclotron harmonics of fusion products near the outer midplane of the tokamak during D-T experiments on JET [37, 38] and TFTR [23, 24, 25]. Though subsequent research has largely focused on edge ICE, which likely will be present in reactor scenarios, ICE roughly localized in the core of the plasma (core ICE) is a burgeoning

[1]The nomenclature is unfortunate; recall that ICE is a coherent wave rather than single particle emission like ECE. Perhaps future researchers may yet rename it so we can discuss this tokamak instability in the same breath as waves seen in space, which bears the name "equatorial noise".

[2]This rough mapping is generally determined by finding roughly where the separation between observed spectral peaks matches f_{ci} of a local region in the plasma (ignoring Doppler shifts) and will be discussed further in Chapter 4.5.

area of study. Several driving mechanisms have been proposed to explain edge ICE, though recent efforts have considered core ICE as well. Highlights of experimental observations are presented in this chapter, followed by overviews of theoretical descriptions.

2.1 Experimental observations

A thorough review of historical (pre-2000) ICE observations is presented in detail in S.R. Cauffman's thesis work [25], including results from TFR [56], PDX [18], PLT [130]. This overview will describe the JET and TFTR results that served as major catalysts for further ICE research, followed by modern edge ICE observations and core ICE.

2.1.1 Edge ICE

2.1.1.1 D-T experiments

In JET deuterium ohmic discharges, radiation corresponding to harmonics of the ion cyclotron frequency was detected (measured through an ICRF antenna on the LFS of the tokamak) and was far stronger than the anticipated blackbody ion cyclotron radiation level [38]. Harmonics of ω_{ci} in the range $f \leq 180$ MHz were found to be excited in the plasma edge by super-Alfvénic particles with large excursion orbits. Upon transitioning from ohmic deuterium plasmas with hydrogen beams to D and D-T plasmas with deuterium beams, ICE intensity was observed to increase with the neutron rate, as illustrated in Fig. 2.1 [37]. This key observation provided the first inkling that ICE could be driven by fusion product populations. Note, ICE power was *not* dependent in these cases on the actual beam species injected. Correlations in ICE amplitude were also observed between edge-localized modes (ELMs) [37] and sawteeth [144].

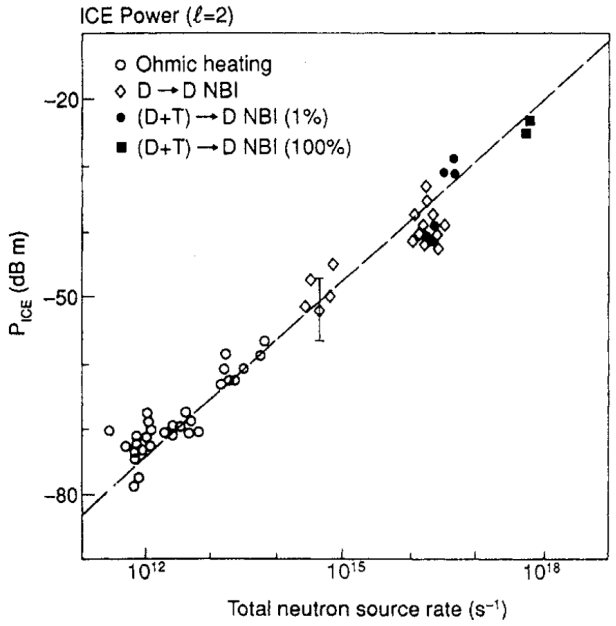

Figure 2.1: ICE power (P_{ICE}) vs. neutron rate in both ohmic and NBI-heated JET plasmas, where the dependence is nearly linear ($P_{ICE} \propto R_{neutrons}^{0.9\pm0.1}$). Figure taken from [37].

Soon after, ICE observations in TFTR were made using probes comprising a pair of orthogonal single-turn $\dot{B}$ loops that simultaneously measured toroidal and poloidal fluctuations in the magnetic field $\dot{B_T}$ and $\dot{B_P}$ [23, 74]. Though narrowband ICE driven by super-Alfvénic beam particles was observed within the first 50 ms of beam injection (deemed "early" ICE), these modes quickly stabilized. Subsequent modes excited by sub-Alfvénic deuterium and tritium populations ("late" ICE) were much broader and persisted until the beam heating was turned off (Fig. 2.2). Both types of ICE were observed in the outer midplane region of the plasma, with early ICE existing just outside the LCFS and late ICE at a slightly smaller radius. Both early and late emission depended on either deuterium or tritium present in the injected beam ion population. Notably, there was no clear relationship between ICE intensity and neutron rate, contrary to the aforementioned results from JET [24, 25]. Though the early ICE intensity was found to increase with neutron rate and not with beam power, this was attributed to differences in plasmas with and without tritium beams rather than any sort of uniform fusion dependence [25].

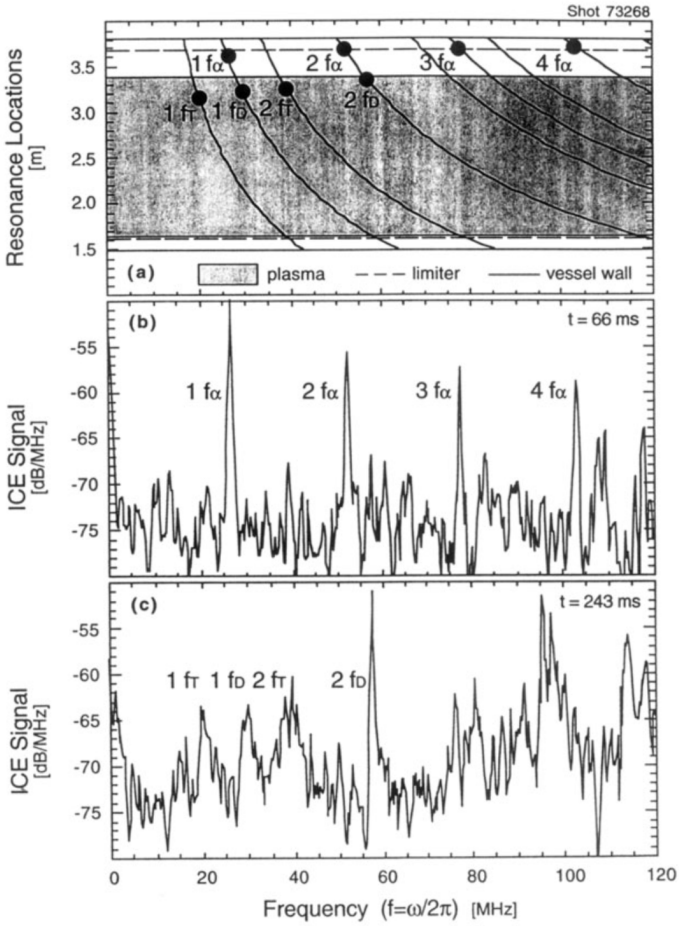

Figure 2.2: (a) ICE emission locations, (b) early ICE, and (c) late ICE in a TFTR D-T supershot. Figure taken from [24].

It also should be noted that the high fusion yield plasmas on JET and TFTR were quite different. In JET, H-mode plasmas were used, which possess temperature and density transport barriers called a "pedestal" near the edge of the plasma. These particular discharges featured initial H-mode phase with increasing neutron rate and large stored energy, followed by a secondary phase in which both parameters declined [37]. In stark contrast, TFTR observations were made in supershot D-T plasmas, which were L-modes that did not feature a pedestal but instead achieved high fusion rates through careful wall conditioning practices that reduced carbon and deuterium recycling rates [154, 155, 176].

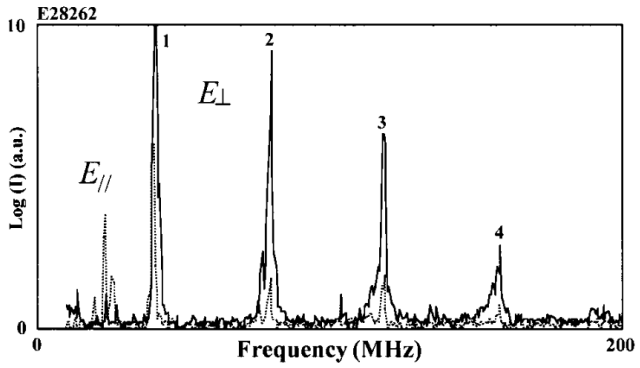

FIG. 15. $E_\perp$ (full line) and $E_\parallel$ (dotted line) spectra: emission from protons at the midplane outer edge.

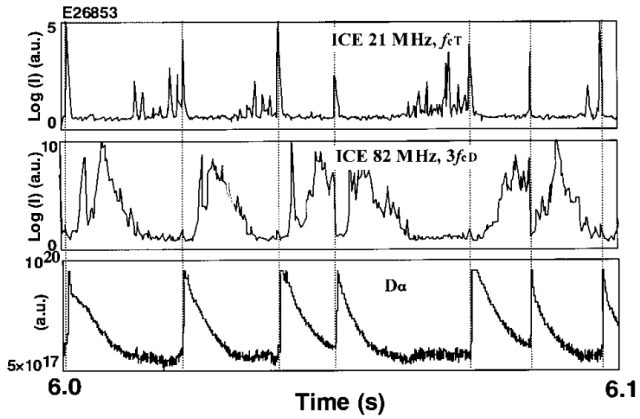

Figure 2.3: (Top) ICE $E_\parallel$ and $E_\perp$ measurements at the plasma edge and (bottom) tritium and deuterium ICE harmonics that are anticorrelated and correlated with ELM peaks, respectively. Figure taken from [92].

2.1.1.2 Modern observations

ICE excited by perpendicular NBI and localized near the LCFS was observed on JT-60U in 1989[3]. In these H plasmas, only the second harmonic was seen and was presumed to be driven by fast ions with an anisotropic velocity space distribution. Subsequent studies again saw edge ICE [92], now in conjunction with core ICE (discussed in the next section). This edge ICE was accompanied by measurements of the parallel and perpendicular electric fields emitted from protons from the midplane LCFS, and the relatively low amplitude $E_\parallel$ was

[3]ICE was initially measured with an electrostatic probe and a perpendicular charge exchange analyzer [92, 146], and later with retired ICRH straps in receiving mode [85, 143, 158, 159].

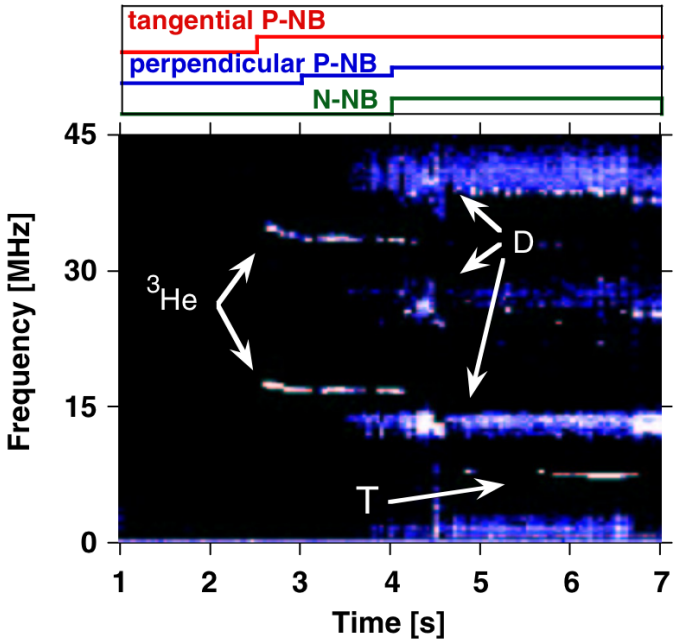

Figure 2.4: ICE in JT-60U driven by perpendicular and tangential positive-ion NBI (P-NB) and negative-ion NBI (N-NB) corresponding to D, ^{3}He, and T ion cyclotron harmonics. Figure taken from [85].

taken as evidence that the observed ICE harmonics were fast magnetoacoustic modes [92]. ELMs were also observed to suppress ICE in these early experiments [92].

In recent years, ICE in JT-60U that is driven by both fusion product populations (namely ^{3}He and T ions) and beam ions via positive- and negative-ion NBI has been reported [85, 143]. Notably, the temporal differences in ^{3}He and D ICE echoed the "early" and "late" ICE observed in TFTR [85] (Fig. 2.4). Subsequent analysis has explored the ^{3}He fast ion distribution, where destabilized modes correlated with a more peaked bump-on tail, compared to similar distributions that were broader in energy and failed to drive ICE [159]. Finally, modes lower than the fundamental ion cyclotron harmonic (deemed "L-ICE" modes) have been observed and negative-ion NBI D ions, rather than tritium from D-D fusion reactions, have been identified as the likely driver [158].

Very similar measurements have been obtained in AUG, where edge ICE was driven by both fusion products and beam ions at harmonics of D and ^{3}He [54]. However, these peaks rarely

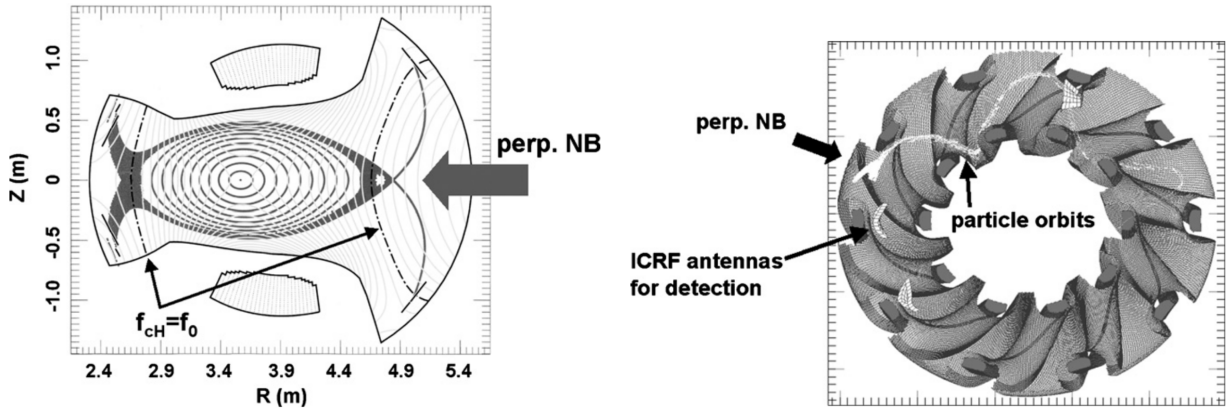

Figure 2.5: (Left) Cross section of LHD a plasma equilibrium and cyclotron frequencies matching that of observed ICE marked by dashed lines. (Right) Aerial view depicting 40 keV hydrogen ion orbits that are born in the outer region of the plasma. Both figures taken from [141].

occurred above the sixth harmonic, contrary to JT-60U and TFTR measurements in which continua of high harmonics were observed and which constituted the majority of the signal power [54]. There was also a discernible spectral difference between fusion product and beam-driven ICE, in that the former was much narrower in frequency ($\Delta f < 100$ kHz) and bursty compared to the low-intensity, noisy beam-driven with a spectral width of $\Delta f \sim 2$ MHz. Generally, edge ICE was observed to be sensitive to ELMs and sawteeth, though limited trigger accuracy made it difficult to discern which preceded the other [54]. Finally, ICRF-driven ICE was observed, which had excitation criteria of at least 3 MW of injected power and $n_e < 3 \times 10^{19}$ m^{-3} [54].

In KSTAR, a fast RF spectrometer (nominal bandwidth 100 MHz–1 GHz) has allowed for finely detailed measurements of ICE spectra. Initial studies in H-mode plasmas found ICE spectra to be a bellwether for ELMs, with high-frequency spectral lines and then wideband RF bursts contaminating the ICE spectra just before the crash [28, 29, 91, 162]. During the crash, ICE harmonics were seen to rapidly chirp [29, 91, 162]. Subsequent studies saw nonlinear wave coupling give rise to chirping ICE near the lower hybrid range of frequencies on submillisecond time scales [28].

ICE has also been observed in helical devices. ICE on the periphery of H plasmas has been observed in LHD, driven by perpendicular NBI (Fig. 2.5) [141] and ions expelled from the core via TAEs [142]. Tangential NBI has also excited ICE, alongside nonlocalized modes in the lower hybrid range whose frequencies tended to increase with n_e [140]. Transient ICE has been excited by fusion-born protons rather than beam ions [137]. Ongoing studies include investigation of ICE dependence on the species mix in the bulk plasma [105]. Beam-driven ICE has also been observed on the W7-AS stellarator [147].

As of writing, there are no ICE observations in literature from the 2021 JET D-T campaign, but observations may yet be published.

2.1.2 Core ICE

Some of the first observations of core ICE were made in the JFT and JFT-2M tokamaks in 1984 [124, 177]. Second harmonic beam-driven core ICE in JFT-2M appeared ∼2 ms after beam injection and lasted roughly 20 ms, followed by fourth harmonic ICE [124]. Hydrogen beam injection into a deuterium plasma destabilized ICE, but a hydrogen bulk plasma did not [124]. Subsequent experiments with short pulse NBI found that ICE was excited above a positive critical value of $df(v_\parallel)/dv_\parallel$ [177].

Contrary to the typical edge ICE seen on JT-60U and its predecessor JT-60 [146], 1–3f_{ci} tritium harmonics emitted from the center of the plasma have been reported on JT-60U in high-β_P plasmas [92]. Somewhat surprisingly, these modes were anticorrelated with ELMs. They also did not correlate with TAE-induced losses, in contrast to observations made earlier in DIII-D [55].

In AUG, core ICE was also suspected to be driven by fusion products, though this is ambiguous as the fundamental hydrogen cyclotron harmonic coincides with the second deuterium

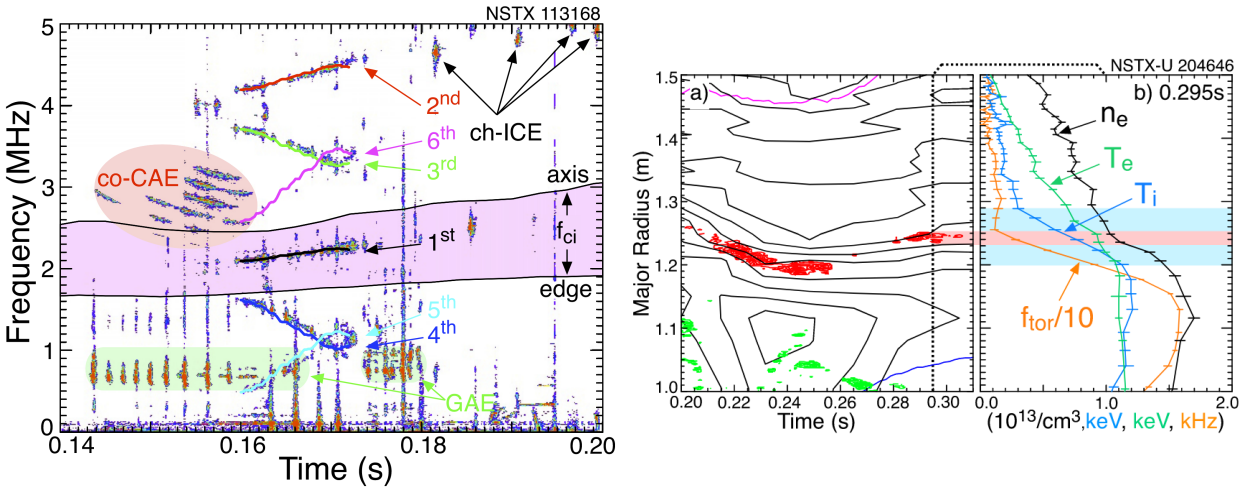

Figure 2.6: (Left) ICE, ch-ICE, CAEs, and GAEs observed on NSTX-U and (right) ICE mapped to an internal transport barrier, where the fundamental ICE harmonic is shown in red and higher harmonics in green. Figures taken from [60] and [61], respectively.

harmonic [123]. This was not the case in TUMAN-3M, in which core ICE was excited in the absence of fusion products in hydrogen plasmas and in spite of ill-confined fusion products in deuterium plasmas [4]. This ICE exhibited fine-scale frequency splitting on the order of 100–300 kHz, and higher frequencies were destabilized ahead of the fundamental harmonic [4]. In EAST, frequencies corresponding to either the fundamental hydrogen or second deuterium cyclotron harmonic were observed near the core of the plasma, along with edge ICE driven by deuterium ions [110, 111].

ICE on NSTX(-U) presents an interesting break in pattern, both in terms of mode characteristics and localization. Rather than emission radii near the core or edge of the plasma, the observed 1–6f_{ci} ICE harmonics instead were localized near an internal transport barrier [60, 61]. These modes often manifested as short bursts on the order of ∼10 ms, with fine-scale splitting on the order of $^{\delta\omega}/_{\omega} \approx 2.7\%$ (ω being the wave frequency) [61]. Subsequently, ICE exhibiting simultaneous upward/downward chirping was observed and deemed "chirping-ICE" (ch-ICE), with modes lasting ∼1 ms [60].

Finally, ICE has recently been observed in predominantly hydrogen JET plasmas via the

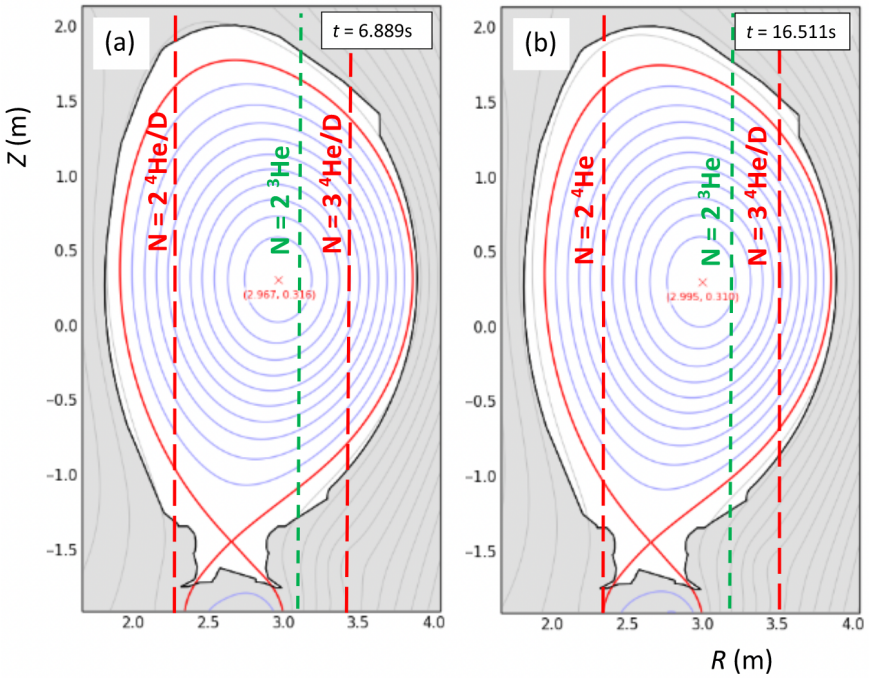

Figure 2.7: Likely emission radii for ICE observed via the sub-harmonic arc detection system in an ICRH transmission line in JET, where minority ICE is excited by energetic minority ^{3}He and possibly deuterium ions. Figure taken from [115].

subharmonic arc detection system in the transmission line of ICRF antennae [88, 115], which constitutes a likely avenue for ICE measurements on ITER. Harmonics of the minority species ^{3}He ($n_{He} < 12\%$) have been observed in both L- and H-mode plasmas, though some of these peaks overlap with those of deuterium. In initial results, ICE was mapped back to the periphery of the plasma [88], but subsequent spectra corresponded to the core of the plasma (green line in Fig. 2.7) or regions between the axis and LCFS (red lines) [115]. Accompanying simulation work, both in linear and nonlinear regimes, is discussed in Chapter 2.2.1.

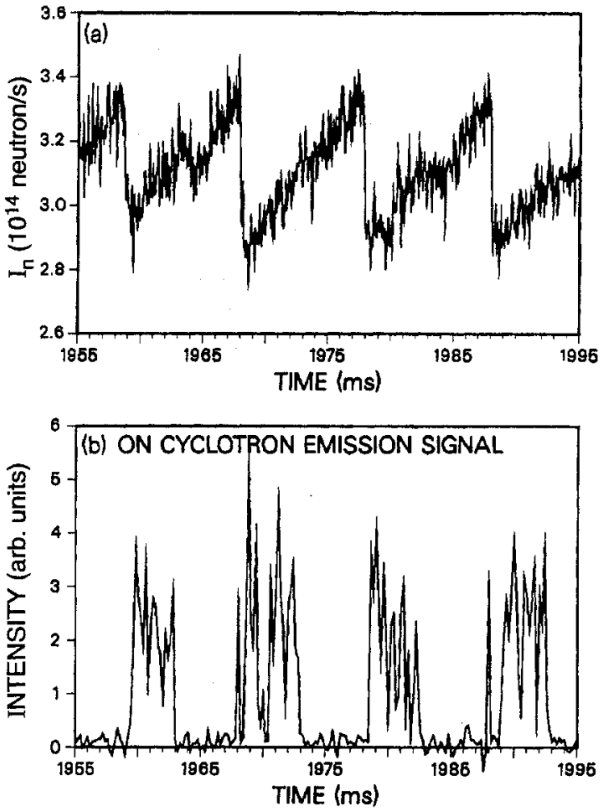

Figure 2.8: (a) D-D neutron emission during a period with TAE activity and (b) corresponding ion cyclotron emission intensity in the frequency range 16.8 ± 0.3 MHz. Figure taken from [55].

2.1.3 Observations on DIII-D

Initial observations on DIII-D[4] saw ICE excited via TAE-induced losses (Fig. 2.8), whereby the expulsion of fast ions from the core of the plasma gave rise to multiple harmonics of the deuterium cyclotron frequency in the edge [55]. Since, off-axis fishbones [78], ELMs [163, 164, 165], and prompt losses [127] have all been seen to excite ICE, generally in the edge of the plasma. This latter result was the first inkling that ICE in DIII-D may depend on NBI geometry, as beams with near-tangential injection angles with respect to the centerpost

[4]All early measurements were made using small wire loops installed behind the first wall armor by Ikezi et al. [86]. Remnant tile loops from the first fast wave interferometer/reflectometer diagnostic [78, 173] and then retired ICRH antennae straps in receiving mode were implemented, with these latter two being combined to be the first iteration of a dedicated ICE diagnostic. ICE diagnostic history and upgrades are discussed in more detail in Chapters 3.2.1 and 3.2.2.

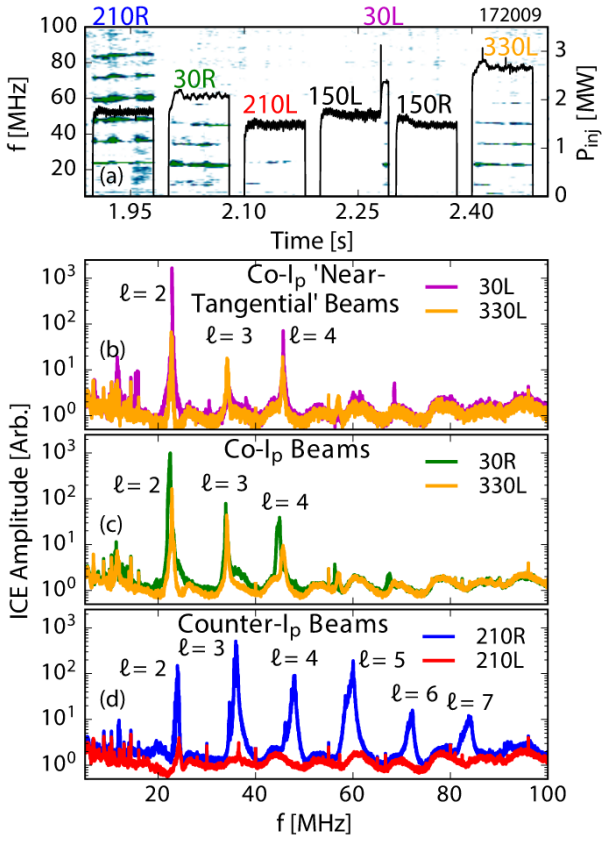

Figure 2.9: An example of core ICE spectra excited by different beam geometries and energies on DIII-D, where (a) depicts the beam injection powers overlaid with time/frequency spectra and (b–d) are ICE diagnostic data averaged over the course of each beam pulse. Figure taken from [165].

drove strong second harmonic edge ICE, contrary to their near-perpendicular counterparts, which at best produced weak, scattered spectral lines. The first core ICE observations were made by Axley and Pinsker, with core ICE appearing in solely deuterium plasmas and edge ICE observed in both deuterium and He plasmas [6].

These fairly sparse studies finally culminated in full-fledged dedicated experiments in 2017[5]. These experiments explored high-frequency modes using the previous version of the ICE diagnostic, the first examining ICE and the second investigating high-frequency sub-cyclotron modes. The ICE experiment explored core and edge ICE in both L- and H-mode plasmas,

[5]Conveniently, the 2017 ICE experiment occurred in the morning and was followed by compressional and global Alfvén eigenmode (GAE and CAE) studies later that same day.

starting with investigations in inner wall-limited oval L-mode plasmas in which beams of different injection geometries were cycled to investigate ICE dependence on fast ion distribution. As pictured in Fig. 2.9, the on-axis beams injected against the plasma current (counter- or ctr-I_P) excited numerous harmonics of the deuterium cyclotron frequency near the magnetic axis, with the third being dominant [165]. The co-I_P beams, however, largely excited harmonics $f = 1$–$4f_{ci}$ with a pronounced second harmonic [165], and off-axis co-I_P beams (those tilted with respect to the midplane) did not excite any ICE. In comparison, edge ICE on DIII-D was not heavily dependent on NBI geometry, appearing instead with the drop in D_α signal marking the L-H transition in H-mode plasmas [165]. These spectral peaks spanned harmonics $\gtrsim 9f_{ci}$ and were relatively broadband in nature (reminiscent of the late ICE described on TFTR), with widths of roughly 3 MHz.

Other high-frequency modes such as global and compressional Alfvén eigenmodes have also garnered attention at DIII-D. The free energy available in velocity space gradients of the fast ion distribution, which is known to drive ICE, can also resonantly excite MHD instabilities such as CAEs and GAEs at frequencies approaching or just slightly exceeding f_{ci}. While these sub-cyclotron modes are more commonly observed on spherical tokamaks such as NSTX(-U) [59, 157] and MAST [148] due to their large super-Alfvénic fast ion populations, they have also been seen in conventional tokamaks. A dedicated experiment (also in 2017) explored these eigenmodes on DIII-D, cycling through various neutral beam geometries in simple oval-shaped L-mode plasmas to explore the modes' dependence on fast ion distribution alongside general phenomenology. These studies identified these high-frequency sub-cyclotron modes as shear-polarized GAEs rather than the previously reported CAEs [123], and determined a threshold neutral beam injection rate above which the modes were destabilized [161]. These modes are most consistently observed at low B_T (≤ 1.8 T). Sub-cyclotron modes have subsequently been detected in other conventional tokamaks, including AUG [121], and JT-60U [158]. Realistic simulations have accompanied detailed measurements of sub-cyclotron modes on other devices, most notably NSTX [11, 12, 58, 63, 103] and DIII-D [10, 11, 161],

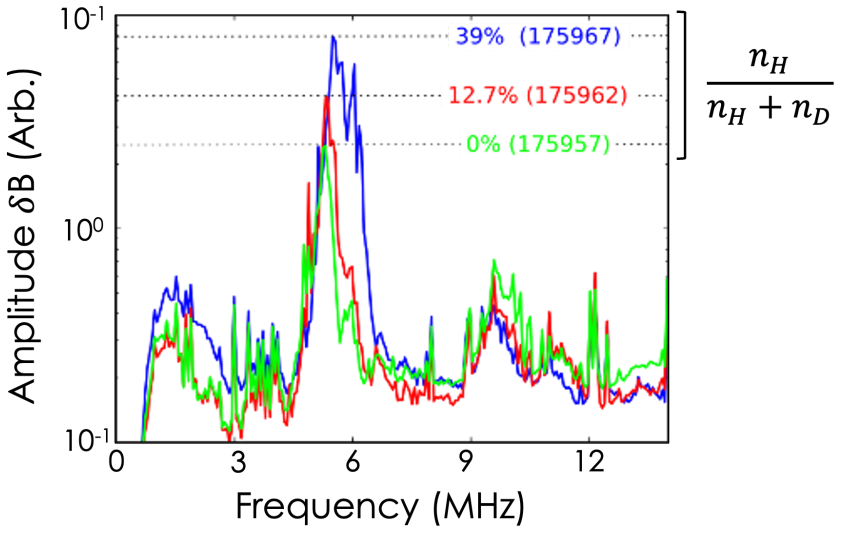

Figure 2.10: Amplitude of sub-cyclotron modes excited by a 2.5 MW co-I_p, near-tangential D beam in $B_T = 1.25$ T plasmas with different bulk species mixes ($\frac{n_H}{n_H+n_D}$). Figure adapted from [43].

providing reference points for the new DIII-D measurements discussed in Chapter 4.

ICE and sub-cyclotron modes were probed again in a 2018 during a Frontier Science experiment [172], serving as proxies for equatorial noise and electromagnetic ion cyclotron (EMIC) instabilities found in the earth's radiation belt [9, 139]. In addition to the beam-cycling technique described above, the species of both the plasma and beams were altered and the magnetic field strength varied. Though results are preliminary, sub-cyclotron mode amplitude appeared sensitive to the bulk species mix in H-D plasmas as higher amplitude modes corresponded with higher hydrogen fractions [43], contrary to observations of sub-cyclotron modes in D and H-D plasmas made in MAST [125, 149]. As for ICE, the dominant harmonic excited by the co-I_P beams was observed to change from the second to the fourth as $\frac{n_H}{n_H+n_D}$ was increased; no similar trend was observed for dominant harmonics excited by counter-injecting beams [43]. Data from high-B_T shots early in this experiment, when the bulk ion species was $> 95\%$ deuterium, are used for comparison in work presented in Chapter 4.2 as the beams at 210° were not yet permanently tilted off-axis. Follow-up experiments were conducted in 2020 using the upgraded ICE diagnostic; however, results have yet to be

published. As briefly mentioned in Chapter 2.1.1, species mix investigations similar to these Frontier Science experiments were recently performed on LHD [105].

These 2017 and 2018 sub-cyclotron and ICE studies provided the basis for the experiment performed in the course of this thesis work, which is described in more detail in Chapter 4.1.

2.2 Theoretical models

Multiple excitation mechanisms have been devised to explain ICE. Many of these theoretical explanations concern the interaction between fast ion populations and fast magnetoacoustic waves (FMWs), with the two predominant descriptions being the magnetoacoustic cyclotron instability (MCI) and the Alfvén cyclotron instability (ACI). Though their names may be unsettlingly similar, they diverge by considering the local (fast) and the global (slow) resonance conditions, respectively. Overviews of both theories and highlights of associated modeling are presented in the following two sections.

2.2.1 Magnetoacoustic cyclotron instability

The MCI description, which is covered extensively in both S.R. Cauffman's [25] and B.C.G. Reman's Ph.D theses [134], arises from considering fast ions against a uniform plasma background [8, 49, 50]. Initial theory concerned super-Alfvénic fusion products in JET [51], and the particles were believed to excite waves on the fast Alfvén-ion Bernstein branch. This description was necessarily reconsidered and expanded following observations of ICE driven by sub-Alfvénic fusion products and beam ions on TFTR [23, 24, 25], as these populations' speeds are often low enough that only electrostatic modes need be considered [47, 65].

In the first super-Alfvénic scenario, it is supposed that the wave is perpendicularly prop-

agating with respect to the magnetic field and that there is a resonance between the fast wave and cyclotron harmonic waves. This is described through the ***local*** dispersion relation, which is valid in cases where the mode growth rate is greater than that of the poloidal motion of the resonant particles ($\gamma > \omega_\theta$):

$$\omega = v_A k = l\omega_{ci} \tag{2.1}$$

where ω is the frequency of the wave, v_A is the Alfvén speed, l is an integer, and ω_{ci} the ion cyclotron frequency. Of course, this is reminiscent of the resonance condition (Eq. 1.8) expressed in Chapter 1.3, reprinted here for convenience:

$$\omega - n\langle\omega_\phi\rangle - p\langle\omega_\theta\rangle = l\langle\omega_{ci}\rangle$$

In this case, however, we are interested in the instantaneous matching between the wave phase velocity and the particle velocity. This expression, sans averaging, can be rewritten in terms of wave parameters where k is projected onto the background magnetic field to get $k_\parallel$ and $k_\perp$. Similarly, the fast ion velocity can also be projected onto $\mathbf{B}$ to get the (resonant) particle $v_\parallel$ and v_{Dr}, and incorporated to get:

$$\omega - k_\parallel v_\parallel - k_\perp \cdot v_{Dr} = l\omega_{ci} \tag{2.2}$$

This is the Doppler shifted resonance condition. Here, $v_{Dr} = \frac{\frac{1}{2}v_\perp^2 + v_\parallel^2}{\omega_{ci}} \frac{\mathbf{B}\times\nabla\mathbf{B}}{B^2}$ is the drift velocity for a particle in a tokamak.

MCI analysis originated through analytic descriptions wherein the dispersion relation is calculated for Maxwellian bulk plasma species $\left(f_s(v) = \frac{1}{\pi^{3/2}v_s^3}\exp\left(-\frac{v^2}{v_s^2}\right)\right)$ and anisotropic fast ions, starting with the general dispersion relation:

$$\mathbf{n}\times(\mathbf{n}\times\mathbf{E}) + \epsilon\cdot\mathbf{E} = 0 \tag{2.3}$$

whose solution is determined by setting the determinant to zero. Here, $\mathbf{n} = \mathbf{k}c/\omega$ is the wave index of refraction, $\mathbf{E}$ is the wave electric field, and $\epsilon = 1 + \sum_s \chi_s(\omega, \mathbf{k})$ the plasma dielectric tensor for each species s. $\mathbf{B}$ is taken to be in the $\hat{z}$ direction and $\mathbf{k}$ in the (x, z) plane. The anisotropic fast ion population is often described by a either a ring-beam distribution (illustrated in various coordinate systems in Fig. 2.11) or a shell distribution. Though the latter is isotropic like the expected birth profile of NBI ions, little difference in ICE from the ring-beam and shell distributions has been observed in recent modeling studies [26] and the ring-beam is easier to handle analytically. It takes the following form in 3D Cartesian coordinates:

$$f^{3D}_{\text{Cart}} = \frac{n}{2\pi v_\perp}\delta(v_\parallel - v_{\parallel 0})\delta(v_\perp - v_{\perp 0}) \tag{2.4}$$

where n is the density ($n = \int f^{\text{3D}}(\mathbf{v})d\mathbf{v}$) and $v_\parallel$ and $v_\perp$ are velocities with respect to the magnetic field. In 2D energy, pitch (E, p) coordinates (used commonly in experiment) this becomes:

$$f^{2D}_{\text{Ep}} = n\delta(E - E_0)\delta(p - p_0) \tag{2.5}$$

where $E = \frac{1}{2}mv^2 = \frac{1}{2}m\sqrt{v_\parallel^2 + v_\perp^2}$ is the particle kinetic energy and the pitch is defined as

$$p = \frac{\mathbf{v}\cdot\mathbf{B}}{|\mathbf{v}||\mathbf{B}|} = \frac{v_\parallel}{\sqrt{v_\parallel^2 + v_\perp^2}} \tag{2.6}$$

In the particular derivations cited here, the following ring-beam distribution is used:

$$f_f(v_\parallel, v_\perp) = \frac{1}{2\pi^{3/2}uv_r}\exp\left(-\frac{(v_\parallel - v_d)^2)}{v_r^2}\right)\delta(v_\perp - u) \tag{2.7}$$

where u is the unique perpendicular speed (typically determined by the birth energy), v_d the average parallel drift speed, and v_r the parallel velocity spread.

The full derivation is described elsewhere, but the dispersion relation generally hinges on the following assumptions: i) $E_z = 0$ so the wave is not subject to significant Landau damping;

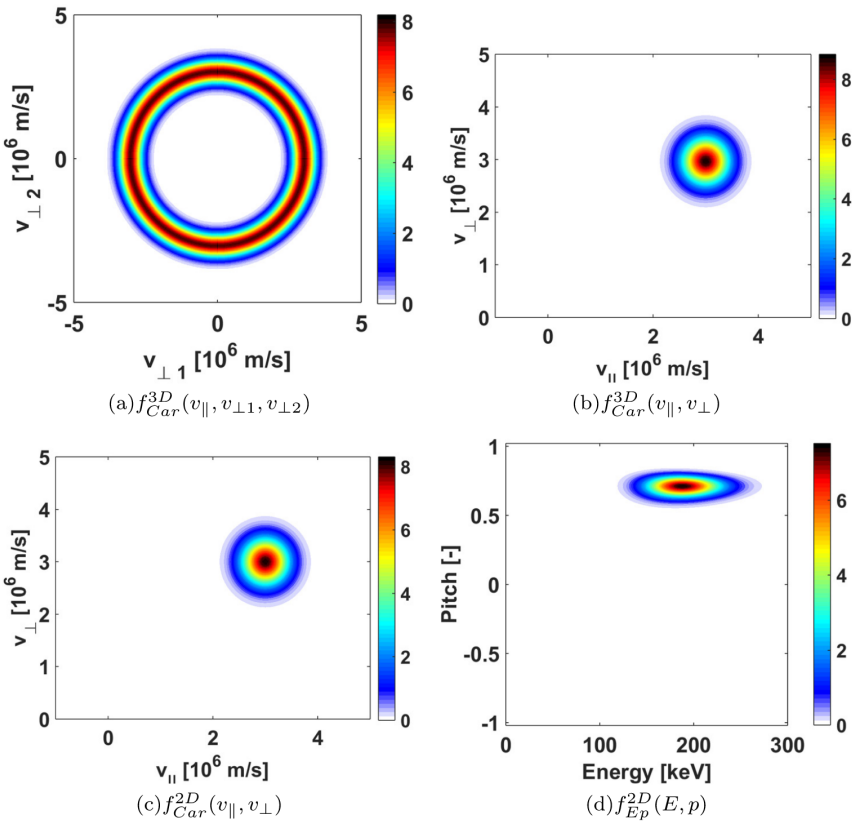

(a) $f^{3D}_{Car}(v_{\parallel}, v_{\perp 1}, v_{\perp 2})$ (b) $f^{3D}_{Car}(v_{\parallel}, v_{\perp})$

(c) $f^{2D}_{Car}(v_{\parallel}, v_{\perp})$ (d) $f^{2D}_{Ep}(E, p)$

Figure 2.11: Example of a simple ring-beam distribution in (a) 3D Cartesian space where $v_{\perp 1}$ and $v_{\perp 2}$ are the perpendicular velocities w.r.t the magnetic field; (b) 3D Cartesian space without gyrophase information ($v_{\perp} = \sqrt{v_{\perp 1}^2 + v_{\perp 2}^2}$, where $v_{\perp 1}$ and $v_{\perp 2}$ are orthogonal to the magnetic field); (c) 2D Cartesian coordinates; and (d) 2D Energy, pitch (E, p) space. Figure taken from [119].

ii) the frequencies of concern are in the ion cyclotron range, i.e., $\omega < \omega_{ce}$; iii) $k_{\parallel} \geq 0$; and iv) the fast ion density is much lower than that of the bulk plasma. This dispersion relation is given by [25, 51]:

$$\begin{aligned}
\omega^2 - a^2 k_{\perp}^2 c_A^2 = & -\omega_{ci}^2 \frac{(\omega - \omega_{ci})[(\omega + \omega_{ci})(\frac{1}{2}N_{\perp}^2 + N_{\parallel}^2) - \omega_{ci}]}{[\omega_{ci} + (\omega - \omega_{ci})N_{\parallel}^2][\omega_{ci} - (\omega + \omega_{ci})N_{\parallel}^2]} \frac{s^2}{2^{s-1}s!} z_i^{2(s-1)} \zeta_0 Z(\zeta_s) \\
& - 2\omega_{ci}^2 \frac{\omega_{pe}^2}{\omega_{pi}^2} a^2 z_e^2 \zeta_e Z(\zeta_e) \\
& + \frac{\omega_{p\alpha}^2}{\omega_{pi}^2} \frac{\omega_{ci}^2}{[\omega_{ci} + (\omega - \omega_{ci})N_{\parallel}^2][\omega_{ci} - (\omega + \omega_{ci})N_{\parallel}^2]} \\
& \times \left([-1 + (\eta_0 - \eta_l) Z(\eta_l)] M_l - \frac{2u^2}{v_r^2} [1 + \eta_l Z(\eta_l)] N_l \right)
\end{aligned} \tag{2.8}$$

where the subscripts i and α refer to the bulk plasma and energetic ion populations, and e to the bulk electrons. The following terms are also defined:

- $N_\parallel = \frac{k_\parallel v_A}{\omega}$ (Alfvén parallel index of refraction)
- $N_\perp = \frac{k_\perp v_A}{\omega}$ (Alfvén perpendicular index of refraction)
- $\eta_l = \frac{\omega - k_\parallel v_d - l\omega_{c\alpha}}{k_\parallel v_r}$
- $z_i^2 = \frac{k_\perp^2 v_\perp^2}{2\omega_{ci}^2}$
- $z_e^2 = \frac{k_\perp^2 v_\perp^2}{2\omega_{ce}^2}$
- $z_\alpha = \frac{k_\perp u}{\omega_{c\alpha}}$
- $a^2 = \frac{\omega_{ci}^2 + (\omega^2 - \omega_{ci}^2)}{[\omega_{ci} + (\omega - \omega_{ci})N_\parallel^2][\omega_{ci} - (\omega + \omega_{ci}^2)N_\parallel^2]}$
- $\zeta_s = (\omega - s\omega_{ci})/(k_\parallel v_i)$
- $M_l = 2l\frac{\omega}{\omega_{ci}}\left(J_l'^2 + \frac{1}{z_\alpha^2}(l^2 - z_\alpha^2)J_l^2\right) - 2\frac{\omega^2 - \omega_{ci}^2}{\omega_{ci}^2}\frac{J_l J_l'}{z_\alpha}[l^2 N_\perp^2 - (z_\alpha^2 - 2l^2)N_\parallel^2] + \frac{2J_l J_l'}{z_\alpha}(z_\alpha^2 - 2l^2)$
- $N_l = -2l\frac{\omega}{\omega_{ci}}\frac{J_l J_l'}{z_\alpha} + \frac{\omega^2 - \omega_{ci}^2}{\omega_{ci}^2}\left[N_\parallel^2\left(\frac{l^2 J_l^2}{z_\alpha^2} + J_l'^2\right) + N_\perp^2\frac{l^2 J_l^2}{z_\alpha^2}\right] + \frac{l^2 J_l^2}{z_\alpha^2} + J_l'^2$

and l is a positive integer chosen such that $l\omega_{ci}$ is closest to the observed wave frequency ω. Similarly, only values of s for which $s\omega_{ci} \sim \omega$ and the "cold" terms $s = \pm 1$ are assumed to contribute significantly [25]. J_l is the Bessel function of order l, and J_l' is its derivative with respect to z.

In the aforementioned case where either the fusion products or beam ions are sub-Alfvénic, the electrostatic limit may be considered. In this case, the general dispersion relation [25, 47]:

$$\sum_s \frac{\omega_{ps}^2}{k^2} \sum_{l=-\infty}^{+\infty} \int d^3v \frac{J_l^2(k_\perp v_\perp/\omega_s)}{k_\parallel v_\parallel + l\omega_{cs} - \omega}\left(\frac{l\omega_{cs}}{v_\perp}\frac{\partial f_s}{\partial v_\perp} + k_\parallel \frac{\partial f_s}{\partial v_\parallel}\right) = 1 \tag{2.9}$$

can be used with the familiar assumptions of Maxwellian bulk species and the drifting ring distribution established in Eq. 2.7 to get the following dispersion relation [25]:

$$\begin{aligned} 1 = &- \frac{\omega_{pe}^2}{\omega_{ce}^2}\frac{k_\perp^2}{k^2} - 2\frac{\omega_{pe}^2}{k^2 v_e^2}[1+\zeta_e Z(\zeta_e)] - \frac{\omega_{pi}^2}{\omega_i^2}\frac{k_\perp^2}{k^2}\sum_{n=-\infty}^{+\infty}\frac{e^{-z_i^2}I_n}{z_i^2}[1+\zeta_0 Z(\zeta_n)] \\ &- \frac{\omega_{pb}^2}{\omega_{cb}^2}\sum_{l=-\infty}^{+\infty}\left(\frac{l\omega_{cb}}{k_\parallel v_r}\frac{k_\perp^2}{k^2}Z(\eta_l)\frac{1}{z_b}\frac{dJ_l^2}{dz_b} + \frac{2\omega_{cb}^2}{k^2 v_r^2}[1+\eta_l Z(\eta_l)]J_l^2\right) \end{aligned} \tag{2.10}$$

where the subscript α has been replaced with b to indicate the slower ion species (e.g., beam ions) are involved here.

In both the electromagnetic and electrostatic cases, the growth rate can either be determined analytically via perturbative analysis or solved for numerically and becomes explicitly a function of the wave propagation angle and experimental parameters, including: local fast ion concentration ($\xi \equiv {}^{n_\alpha}/_{n_i}$), local bulk ion plasma beta ($\beta_i \equiv (1-\xi){}^{v_i^2}/_{v_A^2}$), ratio of fast ion speed to v_A ($\kappa \equiv {}^{v_{\alpha 0}}/_{v_A}$), fast ion pitch angle ($\theta_\alpha \equiv \tan^{-1}({}^{u}/_{v_d})$), ratio of parallel velocity spread to fast ion $v_\perp$ ($\sigma \equiv {}^{v_r}/_{u}$), and T_e/T_i [25, 51]. An example of linear growth rates calculated for conditions similar to those observed in JET is presented in Fig. 2.12, where various wave propagation angles θ are considered for the following parameters: $\xi = 10^{-4}$, $\beta_i = 1.6 \times 10^{-3}$, $\kappa = 1.72$, $\tan(\theta_a) = 4$, and $a = 0.05$ [25, 51]. These parameters largely describe the fast ion population; recall, the bulk plasma is assumed to be homogeneous in this theoretical description.

Subsequent increases in computing power have given rise to fully self-consistent MCI simulations, employing particle-in-cell (PIC) codes (e.g., the fully PIC code EPOCH [3] and hybrid PIC code PROMETHEUS++ [20, 21]) largely in a 1D3V (one periodic spatial domain, three-component velocity space) geometry. The self-consistent Maxwell's equations

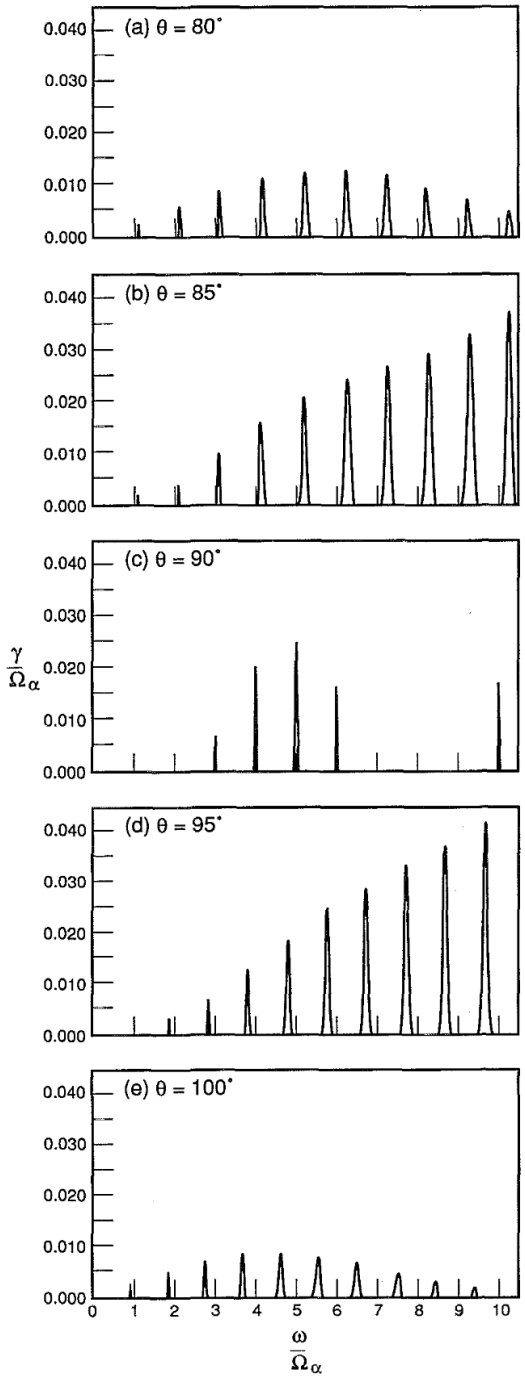

Figure 2.12: Growth rates calculated for various angles of propagation, with energetic alpha particle and deuterium plasma conditions similar to those observed in JET. Figure taken from [51].

and the relativistic Lorentz equation[6]:

$$\begin{aligned}
\nabla \cdot \mathbf{J} &= -\frac{\partial \rho}{\partial t} \\
\nabla \cdot \mathbf{B} &= 0 \\
\nabla \times \mathbf{E} &= -\frac{\partial \mathbf{B}}{\partial t} \\
\nabla \times \mathbf{B} &= \mu_0 \mathbf{J} + \mu_0 \epsilon_0 \frac{\partial \mathbf{E}}{\partial t} \\
\frac{\mathrm{d}\mathbf{p}}{\mathrm{d}t} &= q(\mathbf{e} + \mathbf{v} \times \mathbf{B})
\end{aligned} \tag{2.11}$$

are used to evolve the electromagnetic fields and either fully kinetic particle populations (electrons, bulk ions, and energetic ions) [33, 115] or a fluid electron population and kinetic ions [20, 115]. These simulations recover peaks at harmonics of f_{ci} that resemble both experimental observations and the peaks with appreciable growth rates as predicted by analytic theory [33] (Fig. 2.13). Modeling efforts have since been extended past the initial linear regime to capture nonlinear dynamics and mode saturation.

Nonlinear simulations can better resolve lower harmonics ($1 \sim 4f_{ci}$) that may arise from wave-wave interactions between higher harmonics. Multiple studies have shown higher amplitudes for these peaks than are seen for linear simulations or analytic predictions [20, 115] and thus better agreement with experimental ICE spectra (as seen in the comparison between linear and nonlinear simulations for JET conditions presented in Fig. 2.13). The somewhat default JET case has been extensively studied [20, 33, 34], and subsequent modeling has sought to replicate ICE on KSTAR [27, 28, 29], AUG [109], LHD [136, 134, 135], and DIII-D[7] [179, 180]. Recent hybrid 2D simulations have been performed for JET D-T similar conditions [19], recovering somewhat worse agreement than their 1D counterparts but with future development planned.

[6]Here, $\mathbf{J}$, $\mathbf{E}$, and $\mathbf{B}$ are the current, electric field, and magnetic field vectors, and q, v, and $\mathbf{p}$ are the particles' charge, velocity, and relativistic momentum.

[7]For 1D3V fully kinetic linear modeling of ICE in a DIII-D H-mode plasma, see Chapter 5 in "Simulations of Ion Cyclotron Emission from Energetic Ions in DIII-D tokamak plasmas," A. Zalzali's recently submitted PhD thesis.

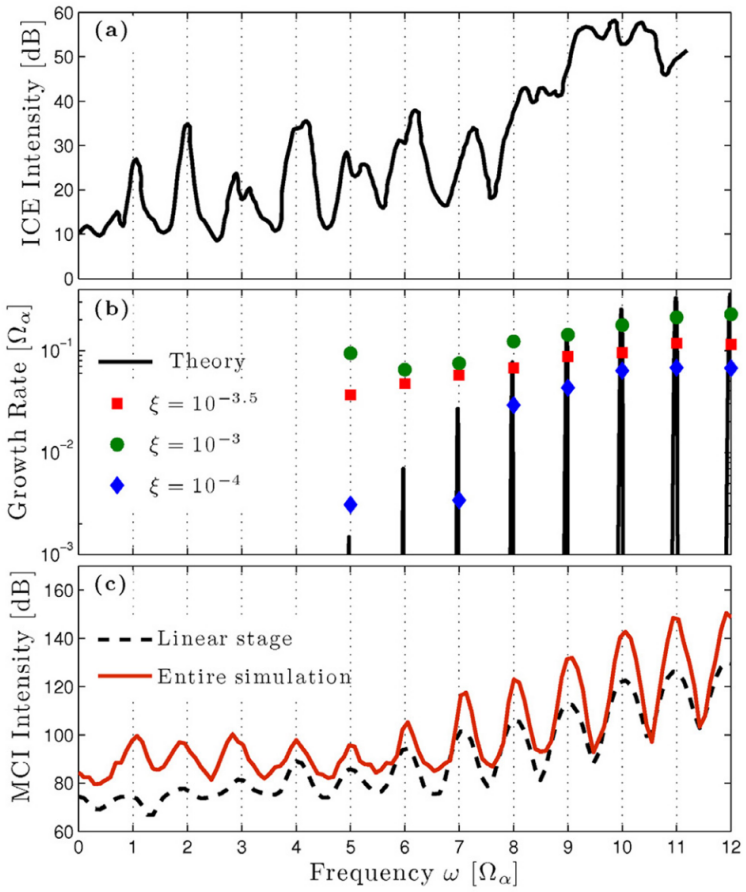

Figure 2.13: (a) ICE intensity measured in JET and (b) growth rates calculated using rough experiment parameters via analytic calculations (black lines) and hybrid simulations (colored symbols). (c) MCI intensity calculated during the linear phase (black) and full simulation duration (red) from hybrid simulations. Figure taken from [20].

In addition to the aforementioned PIC simulations, the global gyrokinetic toroidal code (GTC) [107] has been modified [97, 178] to investigate ICE using a six-dimensional Vlasov equation for ion dynamics and drift kinetic equation for the electrons [178]. These simulations aim to improve upon the simplified models described above by capturing mode spatial structure, time evolution, and realistic fast ion populations.

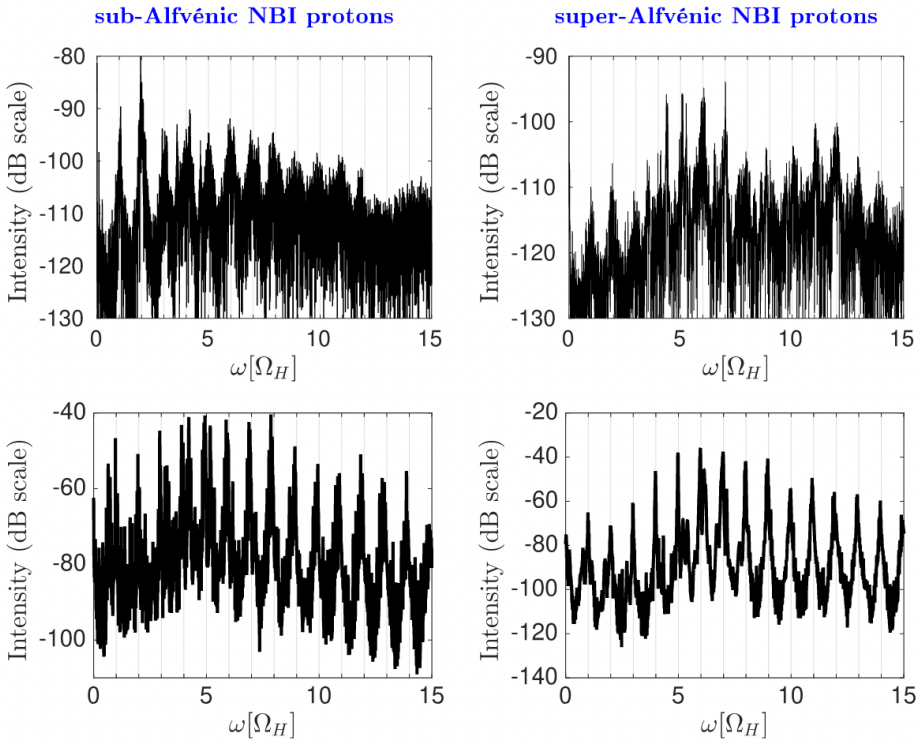

Figure 2.14: Comparison of measured ICE spectra (top panels) and simulated ICE (bottom) in LHD for super- and sub-Alfvénic ions. Figure taken from [136].

2.2.2 Alfvén cyclotron instability

The ACI[8] dissents from the local MCI theory and is instead predicated on the resonance between fast particles and fast Alfvén waves, which in a 2D tokamak geometry are known as compressional Alfvén eigenmodes. The additional condition that the particles must resonate "globally" with the wave can be added to Eq. 2.2 to get [9]:

$$\omega - l\langle\omega_{ci}\rangle = m\omega_\theta - n\omega_\phi + s\omega_b \tag{2.12}$$

where m is the poloidal mode number, n the toroidal mode number, s is an integer, ω_b is the bounce or transit frequency of the fast ions, and $\langle ...\rangle$ denotes orbit-averaging. This is the ***global*** resonance condition, and is valid for slow instabilities when $\gamma < \omega_b$. Specifying the

[8]The nomenclature is somewhat confusing in literature. N.N. Gorelenkov and C.Z. Cheng refer to the MCI as the ACI, though later Cauffman refers to the global theory as ACI. In this work, MCI will represent the local theory and ACI the global.

fast ions' pitch angles and considering those close to their maximum energy, this equation can be rewritten as [9]:

$$\omega - l\langle\omega_{ci}\rangle = k_{\parallel}\langle v_{\parallel}\rangle + s\frac{\langle v_{\parallel}\rangle}{qR_0} \tag{2.13}$$

where q is the safety factor and R_0 is the magnetic axis radius. In contrast to the MCI description, this 2D model naturally takes into account the spatial structure of the modes, which are localized to a distinct region in the plasma. A brief overview is provided here, but the interested reader is referred to the more detailed reviews given in [68] and [69] and/or the detailed derivations in [9, 35, 36, 70, 71, 148].

2.2.2.1 Compressional Alfvén eigenmodes

We can start by considering the wave equation from the two-fluid cold plasma picture for a uniform, slab plasma [104, 153]:

$$\left|\epsilon_{ij} - n^2\left(\delta_{ij} - \frac{k_i k_j}{k^2}\right)\right| = 0 \tag{2.14}$$

and applying the fusion-relevant low pressure ($\beta = {}^{2\mu_0 P_0}/_{B_0^2} \ll 1$) and high conductivity ($E_{\parallel} \ll E_{\perp}$) limits. This, in conjunction with our interest in frequencies $\omega \ll \omega_{pe}$, gives rise to the general dispersion relation [104, 153]:

$$N^2 = \frac{AG}{2F^2}\left[1 \pm \sqrt{1 - \frac{4F^2}{AG}}\right] \tag{2.15}$$

where the Alfvén index of refraction is defined as $N = {}^{kv_A}/_{\omega}$, $\bar{\omega} = {}^{\omega}/_{\omega_{ci}}$ $A \equiv \frac{1}{1-\bar{\omega}^2}$, $F^2 = {}^{k_{\parallel}^2}/_{k^2}$, and $G = 1 + F^2$. Here, in the case of $\omega > \omega_{ci}$, the "+" solution is the compressional wave and the "-" solution is the shear wave and does not propagate[9]. In the single fluid limit

[9]The shear wave does propagate if a hot plasma is considered. Further, in the case of frequencies $\omega < \omega_{ci}$, the "+" and "-" solutions are swapped such that they correspond to the shear and compressional waves, respectively [102].

($\omega/\omega_{ci} \ll 1$), Eq. 2.15 simplifies to the familiar $\omega \approx k v_A$ for the CAE, whereby the heuristic expression stems from writing $k^2 = k_\theta^2 + k_r^2 + k_\phi^2$ and then rewriting k_θ, k_r, k_ϕ in terms of mode numbers in each direction.

Though there are multiple approaches detailed in literature (see [68] and the references therein), the heuristic version of the CAE dispersion relation is useful both for the basic purposes here and in assessing experimental observations [62]. The mode frequency can be approximated as a function of quantum mode numbers m (poloidal mode number), n (toroidal mode number), S (radial mode number), and the characteristic radial width of the potential well L_r [62, 72]:

$$\omega_{CAE}^2 \simeq v_A^2 \left(\frac{m^2}{r^2} + \frac{S^2}{L_r^2} + \frac{n^2}{R^2} \right) \tag{2.16}$$

and the potential well thus takes the form [63, 102]:

$$\left[\nabla_\perp^2 - V_{\text{eff}}(r, \theta) \right] = 0 \tag{2.17}$$

where the potential is given by:

$$V_{\text{eff}}(r, \theta) = k_\parallel^2 - \frac{\omega^2}{v_A^2} \approx \left(\frac{n}{R} \right)^2 - \left(\frac{\omega}{v_A} \right)^2 \tag{2.18}$$

This potential well, aside from spatially bounding the modes, also plays an important role in terms of kinetic effects. When $V_{\mathbf{eff}} = 0$, the Alfvén resonance conditions of the compressional and shear Alfvén waves ($\omega_{SA} = k_\parallel v_A(r, \theta)$) are equal, and the CAE is able to mode convert into the kinetic Alfvén wave (KAW). Allowing for the inclusion of finite Larmor radius effects

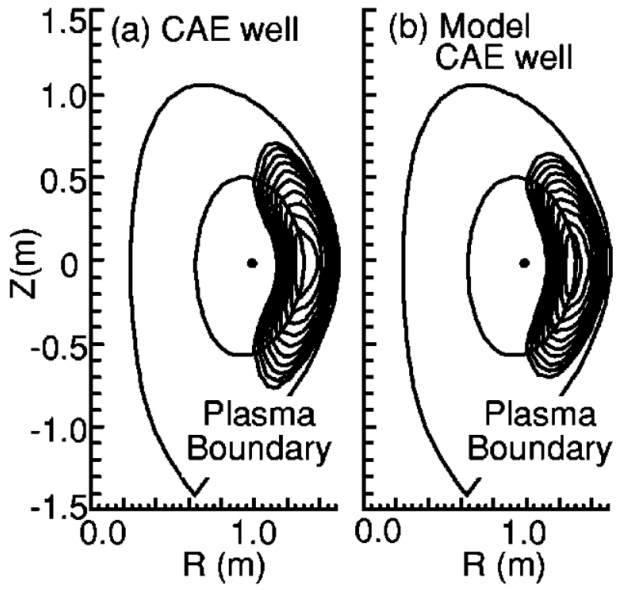

Figure 2.15: Example of a 2D CAE potential well calculated in NSTX. Figure taken from [62].

and shear Alfvén resonances, the CAE dispersion relation can be written as [68, 102]:

$$k_\parallel^2 v_A^2 \rho^2 \frac{\partial^4}{\partial r^4}\phi + \frac{\partial}{\partial r} r(\omega^2 - k_\parallel^2 v_A^2)\frac{\partial}{\partial r}\frac{\phi}{r} = (\omega^2 - k_\parallel^2 v_A^2)\left[-\frac{1}{r^2}\frac{\partial^2}{\partial\theta^2} - k_\parallel^2 - \frac{\omega^2}{v_{A0}^2}\frac{n(r)}{n_0}(1+\epsilon\cos\theta)^2 \right]\phi \quad (2.19)$$

where

$$\rho^2 = \left[{}^{3\omega^2}/_{4k_\parallel^2 v_A^2} + (1 - i\delta)^{T_e}/_{T_i} \right]\rho_i^2 \quad (2.20)$$

and ρ_i is the ion Larmor radius (Eq. 1.5). Analysis of the CAE/KAW solution can introduce energy channeling terms to the thermal electron population [14, 13, 68, 94, 96, 95]—for example, the KAW was determined to be the primary damping source for CAEs in hybrid simulations in NSTX [13]. This CAE/KAW mode conversion results in energy being channeled from the beam ions, and is a candidate explanation for the decreased heating in the core observed experimentally in NSTX [13]. Though no similar phenomenon has been reported for ICE, the effect of CAE/KAW mode conversion may still be a damping source that could affect ICE spectra [68] and should be investigated.

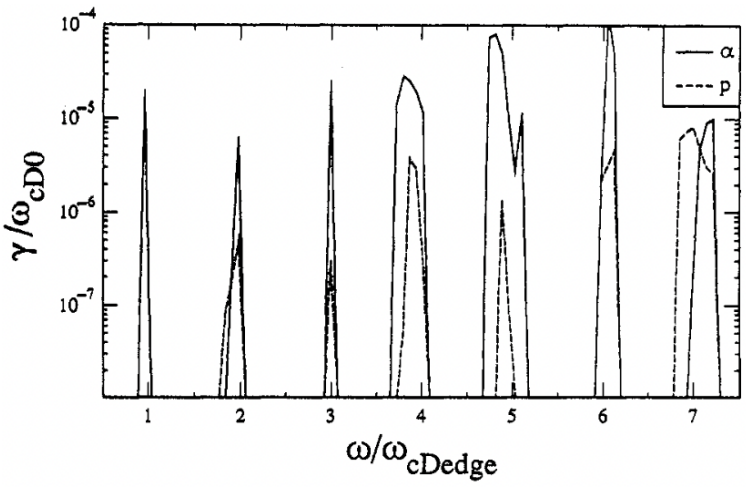

Figure 2.16: ACI growth rates calculated for proton and α particle populations in JET D-T plasma conditions. Figure taken from [70].

2.2.2.2 ICE spectra from CAEs

The derivations that explore ICE due to 2D eigenmodes begin by considering somewhat more complex models for CAEs [73, 151, 150, 152] that arise from Hall MHD and account for plasma ellipticity κ. The modes' eigenfrequencies are given by [69, 93]:

$$\omega_{\mathrm{CAE}} = k(\kappa) v_{A0} \left[\frac{\sigma_m v_A (\ln n)'}{2\omega_{ci}(\kappa)} + \sqrt{1 + \left(\frac{v_A n'}{2\omega_{ci}(\kappa) n} \right)^2} \right]_{r_*} \tag{2.21}$$

and are dependent on the cyclotron frequency (which as a function of elipticity can be written as $\omega_{ci}(\kappa) = \frac{eB}{Mc}\sqrt{\frac{1+k^2}{2}}$), sign of the poloidal wave number $\sigma_m = m/|m|$, and the poloidal wave vector $k(\kappa) = |m|\sqrt{\frac{1+k^{-2}}{2}}/r$. The location of the CAEs is given by [69]:

$$2 + r(\ln n)' - \sigma_m \frac{v_A}{\omega_{ci}(\kappa)} (r(\ln n)')' \times \sqrt{1 - \frac{2 + r(\ln n)'}{(r(\ln n)')'}} = 0 \tag{2.22}$$

where $()' = {}^{\partial}/_{\partial r}$ notation is carried from [68].

Typically, in a linear fast ion instability, the fast ions are only assumed to affect the imaginary part of the frequency (i.e., the growth and damping terms) and not the real frequency, as

the anti-Hermitian term they contribute to the dielectric tensor is assumed to be small[10]. The derivation is detailed in [68], but the resultant growth rate for CAEs interacting with a fast ion distribution $\tilde{f}$ can be written as:

$$\frac{\gamma}{\omega_{ci}} = \frac{\omega^3}{\omega_p^2 \omega_{ci}^2} \frac{\sqrt{2} ecB}{\sqrt{\pi} \Delta r_0 R_0} \sum_{l,\sigma} \int \mathrm{dP}_\phi \mathrm{d}\varepsilon \mathrm{d}\mu I^2 \frac{E_I^2}{E_0^2} \frac{\mu l J_l^2(k_\perp \rho_f)}{(k_\perp \rho_f)^2} \Big[\frac{\partial}{\partial \varepsilon} + \frac{l\omega_{ci}}{\omega B} \frac{\partial}{\partial \mu} \Big] \tilde{f} \tag{2.23}$$

where ω_p is the plasma frequency, $E_1 = E_0 f(r,\theta)$ the component of the CAE electric field, Δ the CAE radial width, J_l the Bessel function of order l, ρ_f the fast ion Larmor radius, and $I^2 = 8\pi / |{}^{\mathrm{d}}/_{\mathrm{d}t}(l\omega_{ci} + \omega_{\mathrm{Drift}})$ is a function that involves the time derivative of fast ion local frequencies [68] to account for the amount of time a particle is in resonance with the mode during its orbit. Here, the Bessel functions arise from finite Larmor radius effects, and the drive comes from the existence of gradients in the distribution function f. The constants of motion ε (particle energy), P_ϕ (toroidal canonical momentum), and μ (adiabatic moment) are evaluated where the mode resonates with the fast particles along their drift trajectory, the condition for which is given by:

$$\omega - l\omega_\alpha(r(\theta),\theta) - \omega_{D\alpha}(r(\theta),\theta) = 0 \tag{2.24}$$

It might be somewhat hidden in Eq. 2.23, but the growth rates notably depend linearly on the fast particle density as the expression stems from linear analysis (which is valid for $\gamma/\omega \ll 1$) [70]. This linear trend differs somewhat from that determined for MCI, where the growth rate was predicted to asymptotically approach $\gamma \propto \sqrt{n_f/n_i}$ as n_f increased [64] (which has reproduced in simulations since, most recently using GTC [178]). Growth rates in this linear have been calculated for tokamak plasma conditions, with an example shown in Fig. 2.16 depicting growth rates for both proton and α particle populations in JET D-T conditions [70]. However, there is little work in the nonlinear regime as of yet.

[10]Note, the instability is close enough to thermal ion cyclotron frequencies that thermal ion effects might in fact affect the real mode frequency in addition to the imaginary part. This has not been explored extensively in literature but may be of future interest.

Chapter 3

Experimental setup

3.1 DIII-D Tokamak

3.1.1 Overview

Since 1986, the DIII-D tokamak [112, 113] has been operated by General Atomics on behalf of the Department of Energy. Featuring copper toroidal field coils from the previous Doublet III machine, it can achieve an on-axis magnetic field strength of up to 2.2 T—oriented either clockwise or counterclockwise around the centerpost—and can routinely reach plasma currents of up to 2.0 MA. The poloidal field is generated through the ohmic heating coil and the poloidal field coils [113]. Multiple non-axisymmetric coils, both in- and ex-vessel, aid in error field correction, tearing mode stabilization, ELM suppression, and more [176]. The water-cooled inconel vacuum vessel encloses a first wall armor of composite graphite tiles, behind which the ICE diagnostic discussed in section 3.2 is hidden. Plasmas in DIII-D regularly last for 5–10 s and can reach ion temperatures of $\sim$ 20 keV in high-performance plasmas [176]. DIII-D boasts multiple auxiliary heating sources, the main workhorses being

Major radius (R)	Minor radius (a)	Magnetic field (B_T)	Plasma current (I_P)	NBI power (P_{NBI})	ECH power (P_{ECH})
1.67 m	0.67 m	2.2 T	3.0 MA	14 MW	2.5 MW

Table 3.1: Maximum nominal operating parameters for the DIII-D tokamak as of 2022. Table taken from [176].

the NBI and electron cyclotron resonance heating/current drive (ECRH/ECCD) systems. During the course of this thesis work, nominally 2.5 MW of ECRH has been available using four 110 GHZ gyrotrons at maximum power, though in the near future this figure is expected to improve with additional gyrotrons. The NBI system nominally can achieve in excess of 20 MW injected power in deuterium, with beam energies of up to 81 keV.

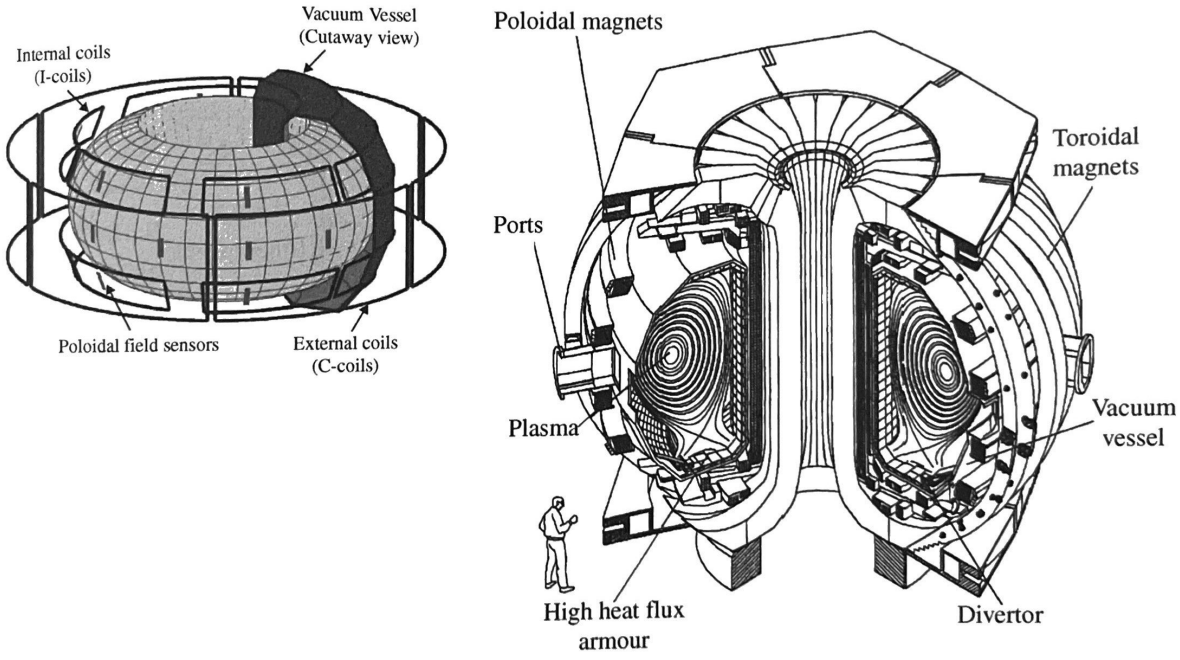

Figure 3.1: DIII-D tokamak external view with coils (left) and cutaway of vacuum vessel (right). Figure taken from [176].

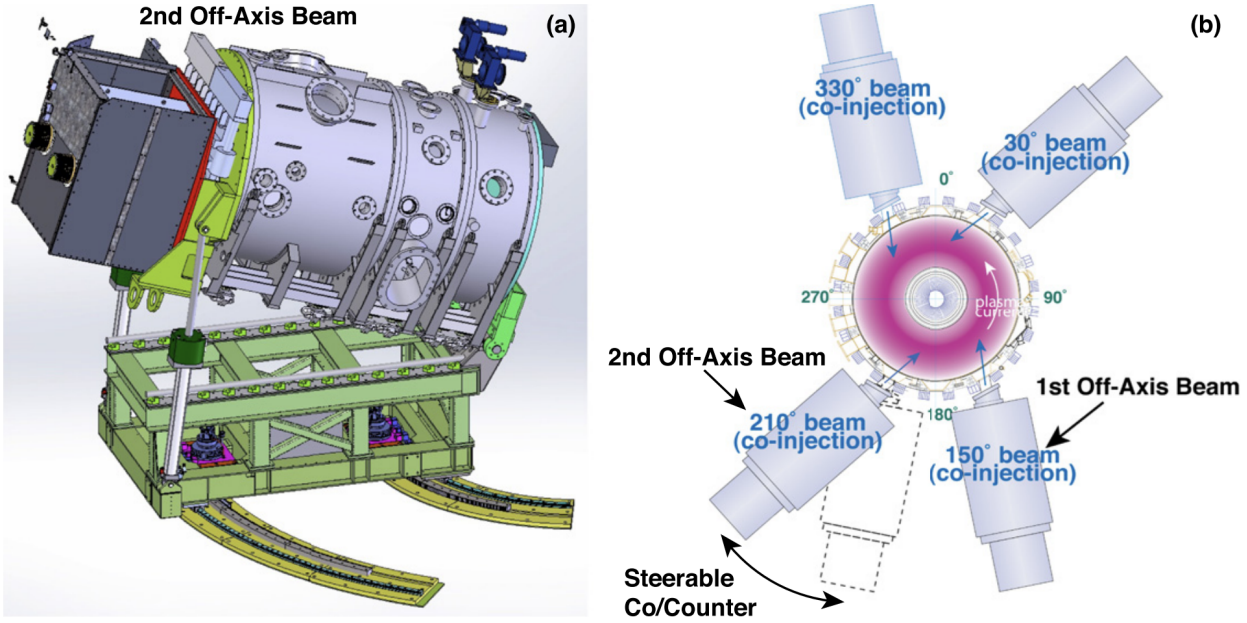

Figure 3.2: (a) Rendering of the 210° beam that was tilted off-axis permanently in 2019, alongside (b) an aerial view of the DIII-D beams. Figure taken from [75].

3.1.2 Neutral beam injection

DIII-D has an extraordinarily flexible NBI system that enables up to eight unique configurations. There are four main beams, each with two beamlines that inject either nearly tangential or nearly perpendicular with respect to the centerpost. The beam at $\phi = 150°$ can be tilted with respect to the vessel equatorial plane as of 2011 [120]. The most recent major upgrade was in 2019, where the formerly on-axis 210° counter-injecting beam was tilted off-axis and now has the capability to rotate and inject either with or against the plasma current [75, 145]. Assuming deuterium injection, the injection energy range for each beam is ∼45–81 keV, resulting in injected powers of roughly 1.0–2.5 MW. Though the beams typically operate at an optimal perveances and fixed energies, both variable beam energy and variable beam perveance can be achieved on DIII-D [145], allowing for even more control over the injected fast ion population.

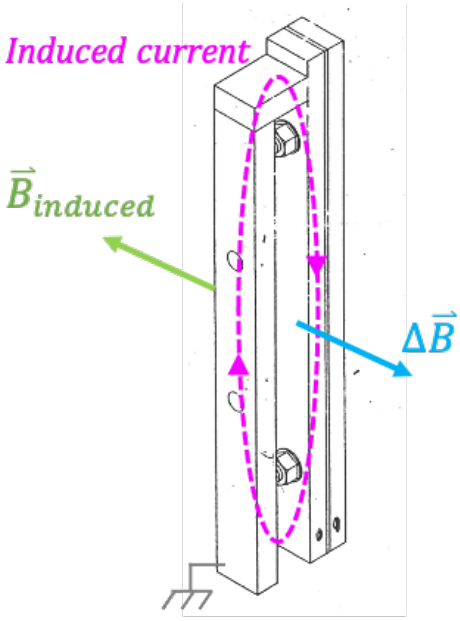

Figure 3.3: Fluctuations in the magnetic field induce opposing currents in a tile loop.

3.2 ICE Diagnostic

The ICE diagnostic on DIII-D is a set of passive magnetic pickup loops installed behind the first wall armor. Fluctuations in the magnetic field result in a changing flux in the loops, thus inducing an opposing voltage via Faraday's law:

$$\varepsilon = -\mathrm{N}\,\frac{\Delta\Phi}{\Delta t} \tag{3.1}$$

where N = 1 for the typical single-turn ICE loops. These voltage fluctuations are then transmitted from the in-vessel loops to a digitizer via a network of coaxial cables. The resulting time series data is typically subjected to a fast Fourier transform and analyzed in frequency space.

A brief overview of the many iterations of the ICE diagnostic on DIII-D are discussed in section 3.2.1, followed by recent hardware upgrades in Chapter 3.2.2, and calculation techniques for auto- and cross-spectral density estimates are presented in Chapter 3.3. The expansion of the ICE system into the lower hybrid frequency range is discussed in section 3.4.

3.2.1 Origins of ICE measurements on DIII-D

The first iteration of the ICE diagnostic on DIII-D was a set of small loops implemented by H. Ikezi to measure injected RF signal during low power (10 W) testing of the 60 MHz ICRH system [86]. A total of 15 2.5–5 cm diameter wire loops were installed behind the existing graphite wall tiles, often in pairs with one loop oriented vertically and the other horizontally so as to measure both δB_t and δB_p. Pairs were installed both on the centerpost and the outer wall. The first EP study using these loops was H.H. Duong's work investigating TAE-induced losses in 1993 [55], where signal from one outboard pair of loops was split eight ways before passing through a variety of bandpass filters at different frequencies before being digitized. The next major upgrade came in the form of tile loops (example shown in Fig. 3.3), whose intended use was for a main-ion interferometry/species mix reflectometry system [173, 174, 175]. These longer loops were installed on the low-field side (LFS) of the machine, and a pair of smaller tile loops on the high-field side (HFS). These tile loops were subsequently used in pickup mode to measure CAEs [79] and ICE driven by losses due to off-axis fishbones [78].

Historically, collection of ICE data has been limited by both computational power and data storage limits. Measurement of a wide range of frequencies (via spectrum analyzer or similar) has often required sacrificing temporal resolution, whereas high temporal resolution has meant digitizing specific frequency bands and using triggers or slow digitizers to record the signal amplitude at various points in the plasma discharge. Increases in computational power (which manifests in hardware as increased sampling rates and upload speeds) alongside greater data storage capabilities have enabled simultaneous temporal and frequency resolution, rekindling interest in high-frequency mode studies. A broadband, high-speed digitizer was first used to measure ICE on DIII-D in 2006, where signal from four remaining wire loops was digitized using a 4-channel 500 MSample/s GaGe digitizer [6]. Since then, 200

MSample/s, 16-bit digitizers have allowed for 5 seconds of continuous data. Studies using this new digitizing power have used the retired ICRH antenna straps in receiving mode [127] and most recently have used a mix of both ICRH straps and tile loops [165, 163, 164].

3.2.2 Diagnostic upgrades

The aforementioned advances in computational power have reinvigorated ICE modelling efforts and highlighted a need for experimental measurements of ICE mode structure, thus motivating upgrades to the ICE diagnostic on DIII-D [46]. These upgrades include the installation of additional in-vessel loops to resolve toroidal mode number, determine polarization at the plasma edge, and enable comparison of signal between the LFS and HFS of the plasma. Simultaneously, the majority of the cables in the system have been replaced and a new high-speed 8-channel digitizer has been implemented.

In-vessel tile loops were installed on both the outer wall (Fig. 3.5a) and the centerpost (Fig. 3.5b), in addition to the existing long toroidal loops at 231.7° and 249.3° [164]. The three long toroidal loops on the outer wall are approximately 51 cm^2 in area[1]. Two small ($\sim$19 cm^2) orthogonal loops of the same design are located near 249°, just below the midplane. The two loops on the centerpost are roughly 15 cm^2 in area. New in-vessel vacuum cables from Times Microwave Systems (Wallington, CT) were installed and connected to the loops. These custom, semi-rigid cables have 0.66 mm ($\sim$0.03") copper inner conductors, 2.29 mm (0.09") diameter 304L stainless steel outer conductors, and loosely packed SiO2 as the dielectric. Nominal electrical and mechanical characteristics are listed in Table 3.2. The SMA end of each cable is affixed to the bottom of a vacuum flange at 255 V+2. The cables then continue down and are spot welded to the vessel wall (underneath the graphite tiles), either passing across the ceiling and down the centerpost or continuing directly down the outer wall side of the vessel. The other cable end has been specially manufactured such that the

[1]For my fellow Americans, 51 $cm^2 \approx$ 1.26e-6 acres.

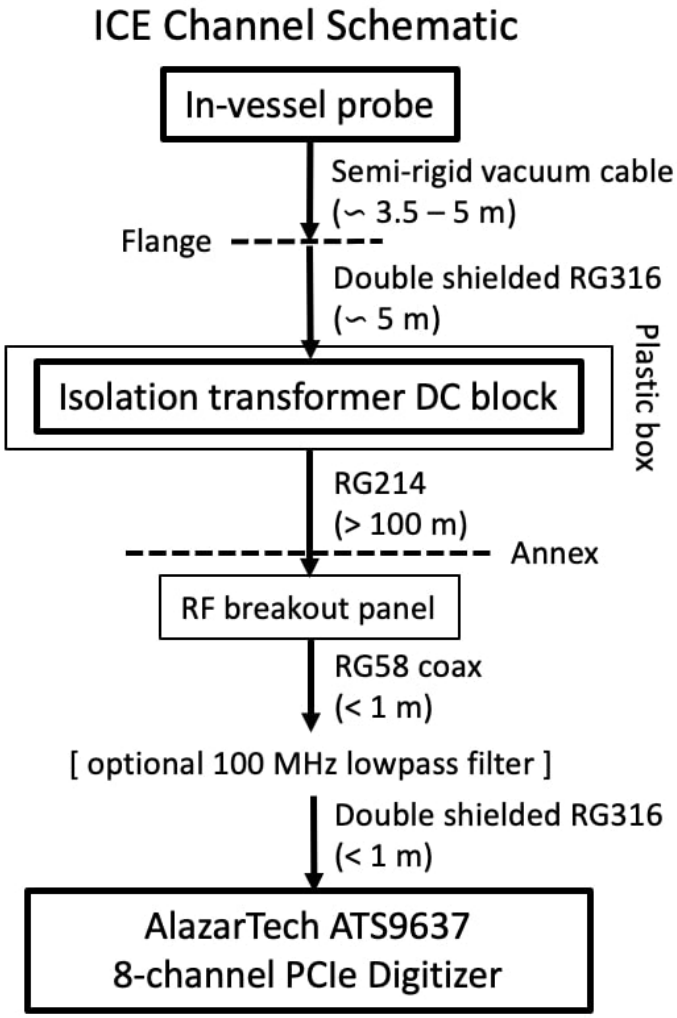

Figure 3.4: Schematic illustrating the components in an ICE channel, from the in-vessel loops to the final digitizer channel. Figure taken from [45].

inner conductor extends roughly 5 cm (just shy of 2") past the outer conductor, and this inner conductor is sandwiched between two washers that are then screwed into the mounting bracket (Fig. 3.6).

At the air side of the flange, double-shielded RG316 cables are screwed to the SMA feedthroughs and travel under a wooden floor until they reach the ICE box. Inside the ICE box, these cables attach to one end of a series of isolation transformer DC blocks from Ikezi's time comprising 15 pF shunt capacitors and ferrite cores.

The DC blocks are one of two main components that impose a bandwidth limitation on

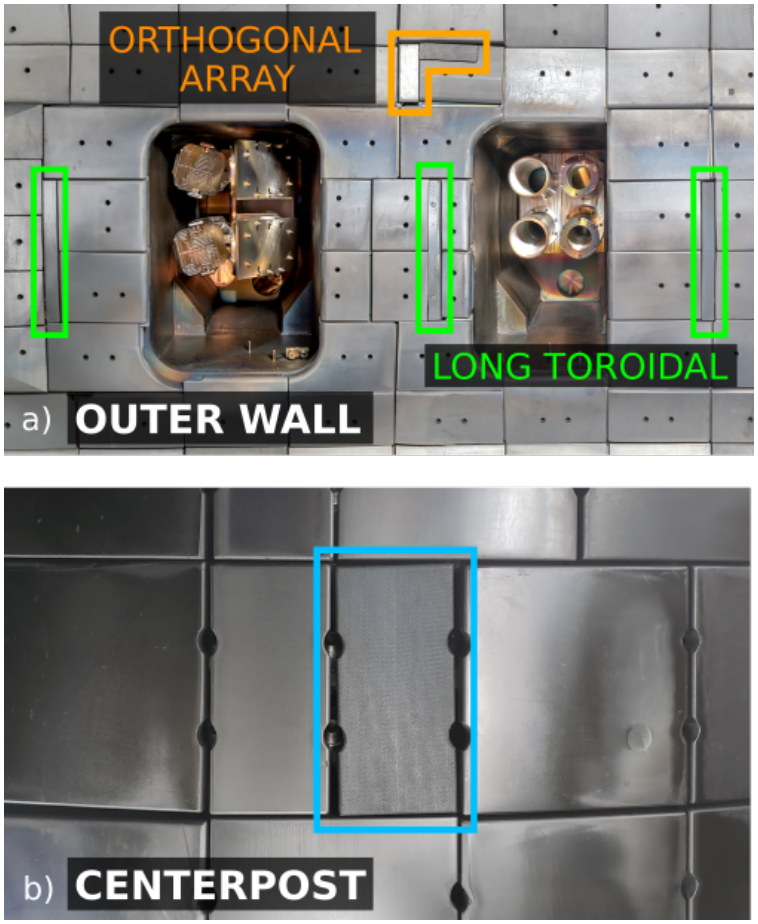

Figure 3.5: (a) In-vessel ICE loops installed on the outer wall of the vessel, including both long loops and a smaller orthogonal loop array; (b) centerpost ICE loops. Figure adapted from [46].

Parameter	Nominal value
Operating temperature	-270° – +900°C
Characteristic impedance	50 Ω
Capacitance	250.0 pF/ft
Velocity of propagation	80%
Maximum frequency	60 GHz
Minimum shielding	-90 dB

Table 3.2: Nominal values for in-vessel mineral-insulated cables.

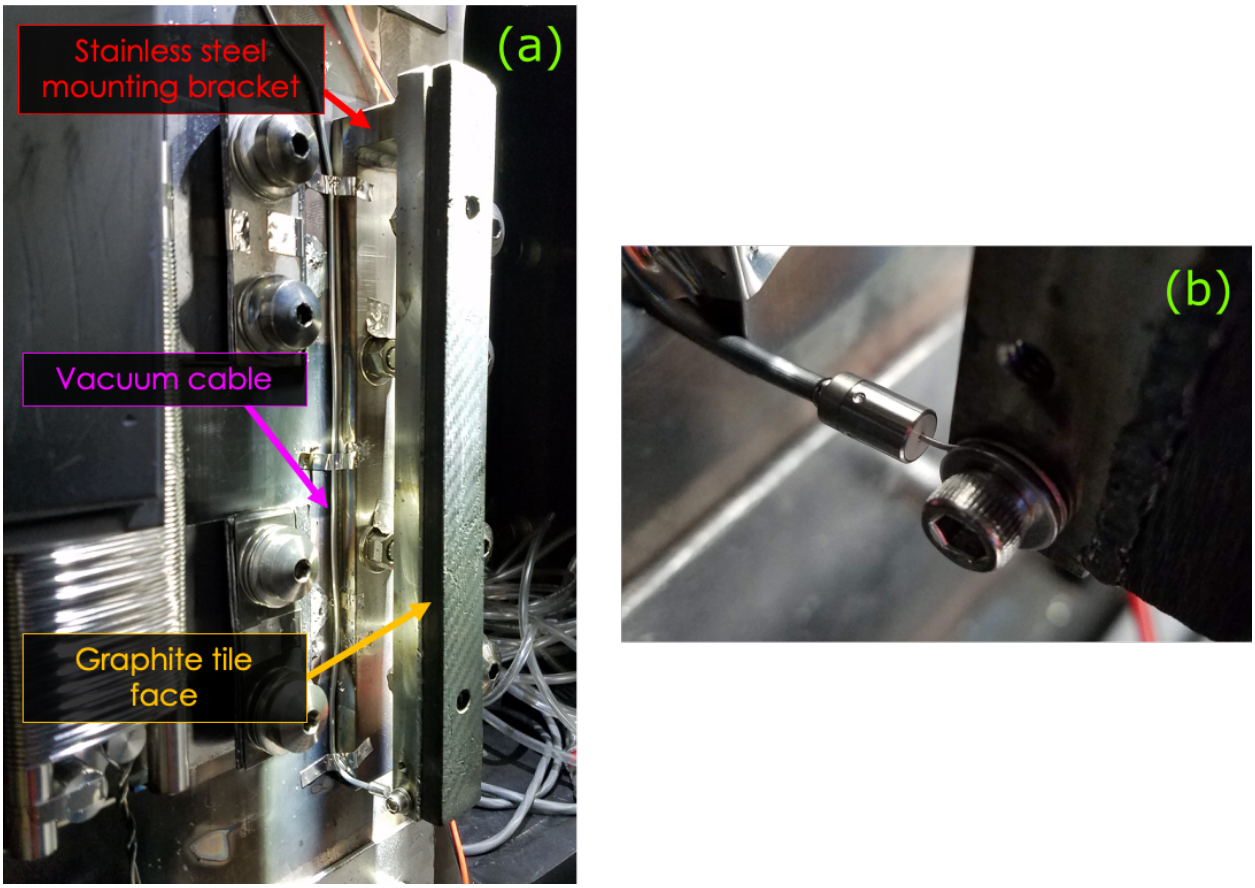

Figure 3.6: Long toroidal ICE loop at 249.3° on the outer wall. (a) Loop assembly including stainless steel mounting bracket, vacuum cable, and graphite tile face. (b) Zoom-in of inner conductor connection to mounting bracket.

the system, the other being the digitizer. Basic alterations to the Ikezi-style blocks were investigated in an attempt to increase bandwidth, namely changing the shunt capacitor value and the type of ferrite core (the effects of which are both depicted in Fig. 3.7.) Unfortunately, these initial studies determined that ferrite-core style isolation transformers generally are not able to achieve bandwidths of more than roughly 120 MHz. Other types of DC blocks were investigated, including two analog coaxial blocks from Spinner (Munich, Germany) and fiber-optic transmitter/receiver units from Liteway, Inc. (Hicksville, NY). The two analog blocks feature nominal 3 kV standoffs and have similar nominal bandwidths, ranging from 80–3800 MHz and 33–4000 MHz. The Liteway fiber-optic system has a nominal bandwidth of 300 kHz–1200 MHz and an input voltage allowance of 0.1–1.0 V_{pp}. A comparison between the

three types of blocks as measured by a network analyzer is shown in Fig. 3.8 (ahead of hi-pot testing), where the transmission coefficient for the Spinner blocks is by far the most favorable even at low frequencies ($f \lesssim 10$ MHz). The ICE diagnostic defaults to using the Ikezi-era ferrite-core isolation transformer blocks, and the high-frequency ICE configuration (Chapter 3.4) employs both ferrite-core and analog RF blocks.

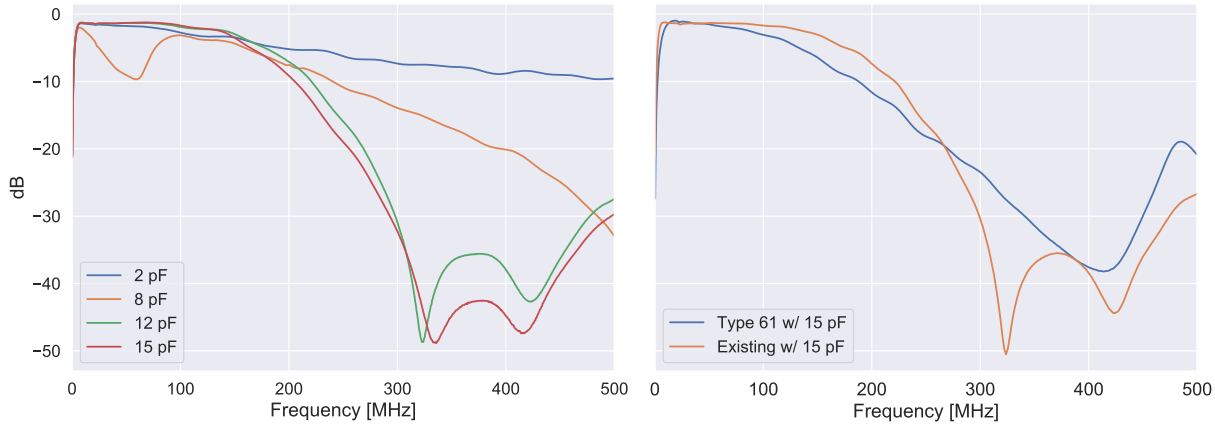

Figure 3.7: Transmission coefficient as a result of changing (a) shunt capacitance value (2 pF in blue, 8 pF in orange, 12 pF in green, and exiting 15 pF in red) and (b) ferrite core type (Fair-rite Type 61 iron core in blue, existing core in orange).

Signal travels from the machine hall via RG52 coaxial cables, which each have one end affixed to the aforementioned DC blocks and the other to a BNC breakout panel in the annex. These BNCs are typically connected to Mini-Circuits BLP-100+ lowpass filters and then to double-shielded RG316 cables that feed directly into an Alazar Tech ATS9637 digitizer. Featuring

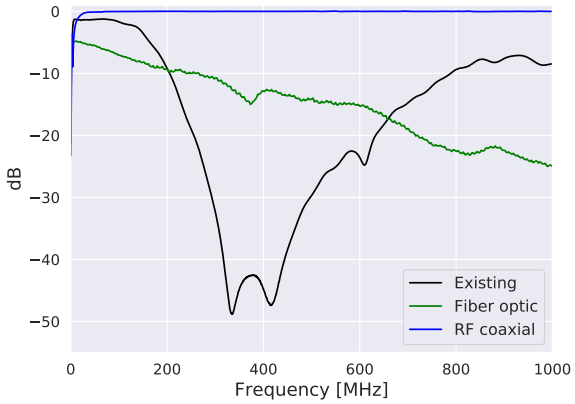

Figure 3.8: Transmission coefficient for each of the three types of DC blocks.

eight channels with 16-bit resolution, the digitizer operates at a default sampling rate of 200 MSamples/s, though expansion to 250 MSamples/s is possible. The raw signal is transferred between shots from the data acquisition computer and ultimately stored in 80 ms segments on the PTDATA server. This data is typically subjected to a fast Fourier transform (FFT) and the resultant spectra can be accessed by a number of tools, including the DIII-D inspect module and the OMFIT ICE module [117, 164].

An example of said spectra for each loop is depicted in Fig. 3.9. Core ICE is excited by a near-tangential 2.5 MW neutral beam in an L-mode plasma (explored further in Chapter 4) and measured by all seven ICE channels and an ICRH strap, which served as a comparison to the previous ICE diagnostic iteration [164]. The time-averaged data from all loop types are in Fig. 3.9(b-e), which all see similar amplitudes when compared to loops of the same category. Major differences in signal amplitude between categories stem from two aspects, the first being that the loop sizes differ, and ones with larger areas (e.g., the outer toroidal loops) will be more sensitive. The second factor is cable losses from the pit to the annex; cables were chosen such that loops within a category have comparable losses. The electrical lengths for each channel are routinely measured with a vector network analyzer (VNA) as discussed in Chapter 3.3.1, which is of particular importance when accounting for phase differences between channels for toroidal mode number calculations (Chapter 4.4).

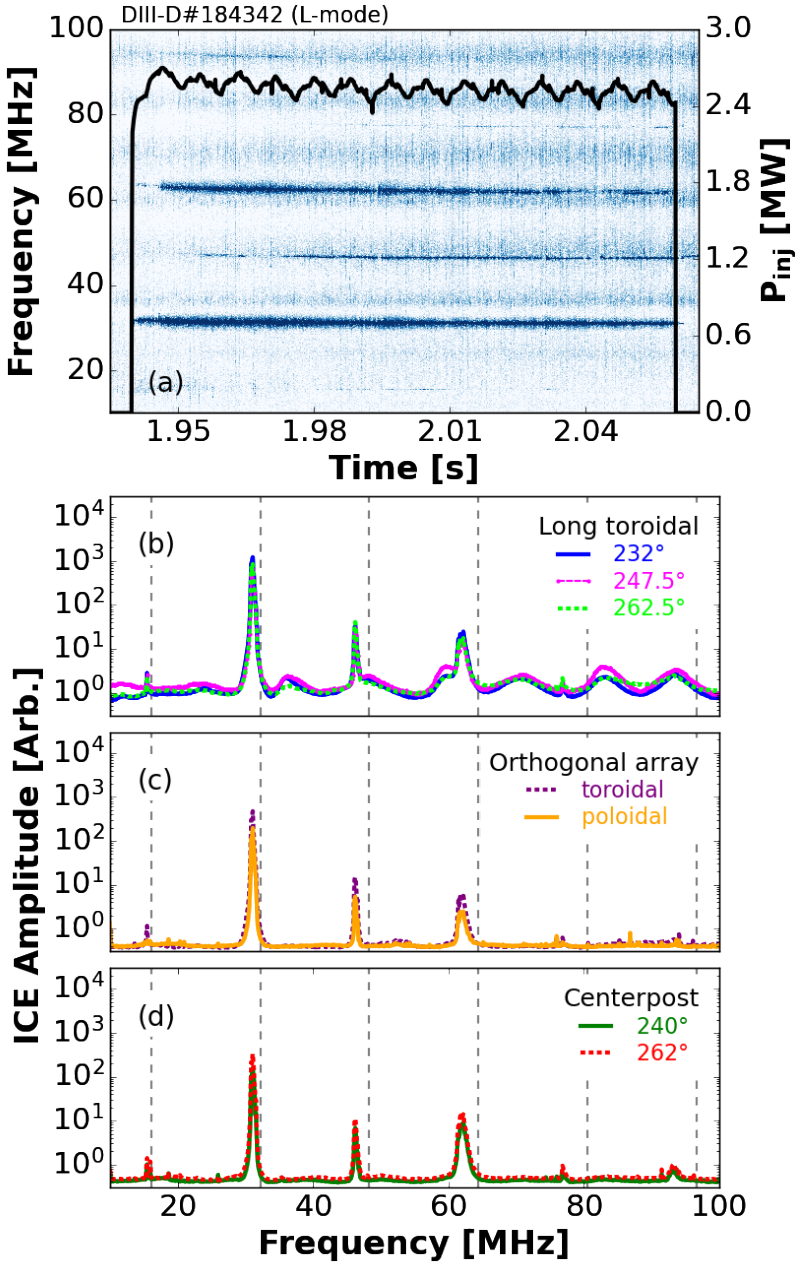

Figure 3.9: (a) Autopower spectrum (via a long outer wall toroidal loop) of core ICE excited by the high-powered, co-I_P, on-axis neutral beam (overlaid black time-trace) in an L-mode plasma at $B_T = 2.17$ T. This autopower spectrum is then averaged over the course of the beam pulse (1940–2060 ms) for each probe type, including: (b) long toroidal, (c) orthogonal, and (d) centerpost ICE loops. Dashed vertical lines (b–d) indicate harmonics of the deuterium ion cyclotron frequency ($f_{ci} = 16.1$ MHz) as evaluated at the magnetic axis. Figure taken from [45].

3.3 Calculation of spectra

Power spectral density analysis, wherein the time-series data mapped into the frequency domain, is a common technique within plasma physics and used to better understand a swath of phenomena, ranging from EP and MHD modes to turbulence [90, 106]. Two methods to calculate auto- and cross-spectra were employed in this work, particularly in an effort to verify toroidal mode number calculations that are further explored in Chapter 4.4. As detailed below, these two methods involve averaging over either time or frequency to achieve a balance between reasonable error estimates and adequate time and frequency resolution.

3.3.1 Time averaging

As each segment of ICE data contains 200 MHz $\times$ 0.08 s $= 16 \times 10^6$ data points, attempting to apply an FFT directly to the raw data is not only computationally expensive, but the low sample size of N = 1 means that the calculated quantities of interest are very susceptible to random noise. The time-averaging (or ensemble averaging) procedure outlined by J.S. Bendat and A.G. Piersol in [15, 16] has thus been implemented to both increase the number of samples for improved statistics and smooth the data by averaging out random noise.

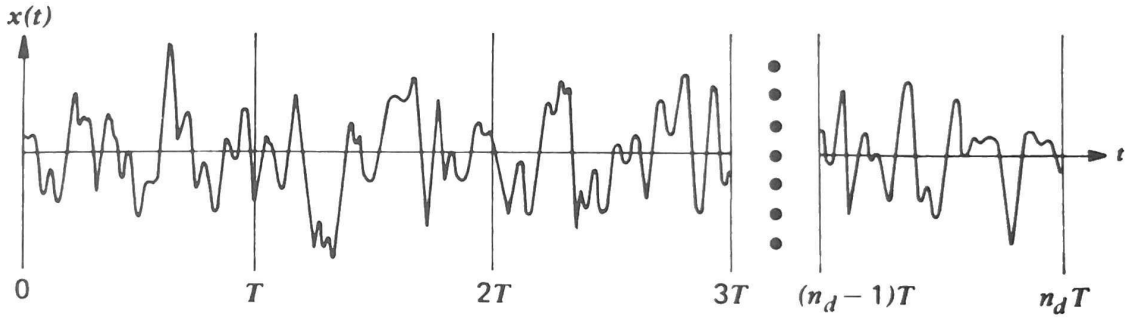

Figure 3.10: Sectioning data into n_d independent subdivisions of time duration T, where there are n_d subdivisions per pixel. Figure taken from [15].

Auto- and cross-power spectral density estimates can be made by collecting some number

of subsequent time subdivisions and then taking the average of the subdivisions' Fourier transformed quantities. An example is illustrated in Fig. 3.10, where a number of n_d subdivisions of time length T are collected for a pixel from some stationary, zero-mean time series dataset $x(t)$. The total length of data analyzed $T_{\text{total}} = n_{\text{pixels}} n_d T$, and the minimum frequency resolution of the analysis is given by[2]:

$$\Delta f = \frac{1}{T} \tag{3.2}$$

In practice, the choice of frequency resolution and number of subdivisions are then used to calculate T and other parameters:

- The number of pixels needed to describe the total time range of interest, $n_{\text{pixels}} = \frac{T_{\text{total}}}{n_d T}$
- Number of points in each subdivision within a pixel, $n_d = \frac{T}{dt} = \frac{1}{\Delta f}\frac{1}{dt}$
- Number of FFT points in each subdivision (2^m for each subdivision ($\ln n_{FFT} = \ln n_T$, rounded up to nearest integer)

where $dt = (200\text{ MHz})^{-1} = 5$ ns is the time difference between digitized points.

The autospectral density function can be estimated by:

$$\hat{G}_{xx}(f) = \frac{2}{n_d T} \sum_{k=1}^{n_d} |X_k(f,T)|^2 \ \ (\text{V}^2/\text{Hz}) \tag{3.3}$$

where $X_k(f,T)$ is the Fourier transformed data over each subdivision. The cross-spectral density function $\hat{G}_{xy}(f)$ can similarly be estimated from two collections of n_d pair subdivisions $x(t)$ and $y(t)$:

$$\hat{G}_{xy}(f) = \frac{2}{n_d T} \sum_{k=1}^{n_d} X_k^*(f,T) Y_k(f,T) \tag{3.4}$$

[2]Note, the frequency resolution is dependent only on the subdivision time length T, not the size of the total time window of interest T_{total}.

Estimated quantity	Random error
Autospectral density $\hat{G}_{xx}$	$\frac{1}{\sqrt{n_d}}$
Cross-spectral density $\left\|\hat{G}_{xy}\right\|$	$\frac{1}{\lvert\hat{\gamma}_{xy}(f)\rvert\sqrt{n_d}}$
Coherence $\hat{\gamma}^2_{xy}(f)$	$\frac{\sqrt{2}\ (1-\gamma^2_{xy}(f))}{\lvert\hat{\gamma}_{xy}(f)\rvert\sqrt{n_d}}$
Cross-phase $\hat{\varphi}_{xy}(f)$	$\frac{(1-\gamma^2_{xy})^{1/2}}{\left\lvert\gamma^2_{xy}\right\rvert\sqrt{2n_d}}$

Table 3.3: Estimated quantities and their associated statistical errors. Table adapted from [15, 16].

where $X^*_k(f,T)$ is the conjugate FFT of signal from the first channel over a subdivision and $Y_k(f,T)$ is Fourier transformed data from the second channel. The coherence between two channels can be calculated using both the autospectral and cross-spectral density estimates from above:

$$\hat{\gamma}^2_{xy}(f) = \frac{\left|\hat{G}_{xy}(f)\right|^2}{\hat{G}_{xx}(f)\hat{G}_{yy}(f)} \quad (\mathrm{V}^2/\mathrm{Hz}) \tag{3.5}$$

Finally, the last estimate of interest is the cross-phase between channels, which relies on the complex cross-spectrum $G_{xy}(f) = C_{xy}(f) - jQ_{xy}(f)$ rather than power spectral density functions. The cross-phase is given by:

$$\hat{\varphi}_{xy}(f) = \tan^{-1}\left[\frac{Q_{xy}(f)}{C_{xy}(f)}\right] \tag{3.6}$$

All of these estimates have associated random errors (ε_r) that all depend on the number of independent averages n_d [15, 16], as listed in Table 3.3.

Uncertainty from measuring the difference in electrical lengths between channels EL_{xy} mandates another term in the total cross-phase error. The electrical length of any ICE channel, which have all been observed to be roughly dispersionless in the default 1–100 MHz frequency

range, is given as:

$$EL = \tau \times f \times 360^{\circ} \tag{3.7}$$

where the time delay τ can be measured using a vector network analyzer [126]. The uncertainty in these measurements, $\varepsilon_m = \delta\tau$, can be added in quadrature with the random error from Table 3.3 such that

$$\varepsilon^2_{\varphi_{xy}} = \varepsilon^2_r + \varepsilon^2_m = \frac{(1-\gamma^2_{xy})}{|\gamma^2_{xy}|^2 2n_d} + (\delta\tau)^2 \tag{3.8}$$

For the toroidal mode number measurements, the electrical lengths and associated errors were measured for each channel. Moving left to right for the three long toroidal loops as depicted in Fig. 3.5(a) (green), the electrical lengths were measured to be $\tau = 289.5 \pm 1.0$, 274.5 ± 1.0, and 278.0 ± 1.0 ns, respectively for the dedicated experiment in this thesis.

3.3.2 Frequency smoothing

An alternate method to the time averaging technique is that of frequency smoothing, which is explained in finer detail (again by Bendat and Peirsol) in section 11.5.5 of [16]. Like in the time-averaging method, the number of subdivisions n_d in a pixel is some power of 2 (2^m). The FFT of $x(t)$ is taken over the entire pixel length and has the time resolution of Δt and Δf, where there are frequencies

$$f_k = k\Delta f, \quad k = 0, 1, 2, ..., (n_d N - 1) \tag{3.9}$$

in the resulting transform $X(f_k)$. The spectral density estimates $\hat{G}_{xx}(f_k)$, $\hat{G}_{xy}(f_k)$, and $\hat{G}_{yy}(f_k)$ can then be computed:

$$\tilde{G}_{xx}(f_k) = \frac{2}{T_r}|X(f_k)|^2, \quad k = 1, 2, ..., (N/2)n_d \ \ (\mathrm{V}^2/\mathrm{Hz}) \tag{3.10}$$

$$\tilde{G}_{xy}(f_k) = \frac{2}{T_r} X^*(f_k) Y(f_k), \quad k = 1, 2, ..., (N/2)n_d \ \ (\mathrm{V}^2/\mathrm{Hz}) \tag{3.11}$$

where $Y(f_k)$ is data from a second channel, as in the previous chapter. These raw estimates are then smoothed. Bendat and Peirsol outline a general method whereby the average of the raw $\hat{G}_{xx}$ and $\hat{G}_{xy}$ estimates is taken over n_d neighboring frequency points, where the resultant center frequencies are at $f_{(1/2)n_d}$, $f_{(3/2)n_d}$, ..., $f_{((N-1)/2)n_d}$. In the frequency-smoothed estimate calculation used in this work (and as is commonly used elsewhere), the IDL `smooth` algorithm is implemented instead, which is a boxcar or moving average that smooths over a width w chosen by the user. Applying this to the raw autospectral density estimate in Eq. 3.11, we can write:

$$G_{xx}(f_k) = \begin{cases} \frac{1}{w} \sum_{j=0}^{w-1} G_{xx}(f_{k+j-w/2}) & \text{if } \ \frac{(w-1)}{2} \leq k \leq N - \frac{(w+1)}{2} \\ G_{xx}(f_k) & \text{otherwise} \end{cases} \tag{3.12}$$

Note, there are not new center frequencies in this case but instead estimates at the same frequencies f_k. This algorithm can equally be applied to $\hat{G}_{xy}$ and $\hat{G}_{yy}$, which in turn can be used to calculate coherence and cross-phase estimates as in the prior section. The frequency-smoothing method achieves the same random error (Table 3.3) and bandwidth resolution ($1/T$) as that of the time-averaging technique. However, the spectral windows and thus the needs for signal processing between these two methods can be quite different, as discussed below.

3.3.3 Overlapping and windowing

Unless $x(t)$ is periodic (with period length T_P) and the subdivision length is some integer multiple of that period length ($T = kT_p$ where $k = 1, 2, 3...$), there can be spectral leakage in the Fourier transformed spectral data. This is more than likely to be the case in observed ICE data, where a superposition of frequencies are observed simultaneously and a (relatively

arbitrary) subdivision length is chosen by the user. Some simple pre-processing techniques can be applied ahead of taking the FFT to mitigate spectral leakage and preserve reasonable resolution.

A step-function window is inherently applied in taking finite sample lengths as depicted in Fig. 3.10, where appreciable discontinuities can be observed at iT and $(i+1)T$ ($i = 0, 1, 2, ..., n_d$). Tapered windows can be applied to eliminate these discontinuities, the most common being the Hanning window that was used in the work presented here:

$$w_h(t) = \begin{cases} \frac{1}{2}(1 - \cos\frac{2\pi t}{T}) & \text{if } 0 \leq t \leq T \\ 0 & \text{otherwise} \end{cases} \tag{3.13}$$

In addition to windowing, overlapping time windows is another technique that can help improve resolution. By choosing time windows that overlap by some percentage (typically in the range of 50–90%), the edge of the subdivision that is suppressed by the windowing function is in the center of the next subdivision. It is of particular use in cases where it is undesirable or not possible to increase the time subdivision length. Higher overlapping rates result in smoother output spectra.

Overlapping and windowing are particularly important for the time-averaging scheme. However, the sidelobes in the spectral window become significantly smaller as the number of subdivisions n_d becomes large in the frequency-smoothing method, and thus tapering and overlapping is not as crucial as it is for the time-averaging method [16]. Nonetheless, overlapping of 60% was used in conjunction with the Hanning window above in both time-averaging and frequency-smoothing codes used in this work.

Overlapping can also affect the computational expense exacted by computing Fourier transforms in either method. Without any overlapping, the time-averaging method is less taxing as it requires FFTs over lengths of n_d as compared to the full subdivision length N in

the frequency-smoothing scheme. However, this can change in the event of overlapped windows [16], e.g., in the case of 50% overlap, the ratio of computations needed for the frequency smoothing vs. time averaging technique is 0.8, and so the former is slightly less expensive. All that said, computational expense is much less an issue now compared to prior decades and thus has not been a factor in choosing one method over another in this work.

3.4 High-frequency ICE configuration

The installation of the high-powered helicon system prompted additional minor upgrades to the ICE diagnostic beyond those detailed in Chapter 3.2.2, which aimed to measure both the injected waves at 476 MHz and potential quasimodes. This non-standard ICE diagnostic configuration has since been dubbed the high-frequency ICE (HICE) configuration.

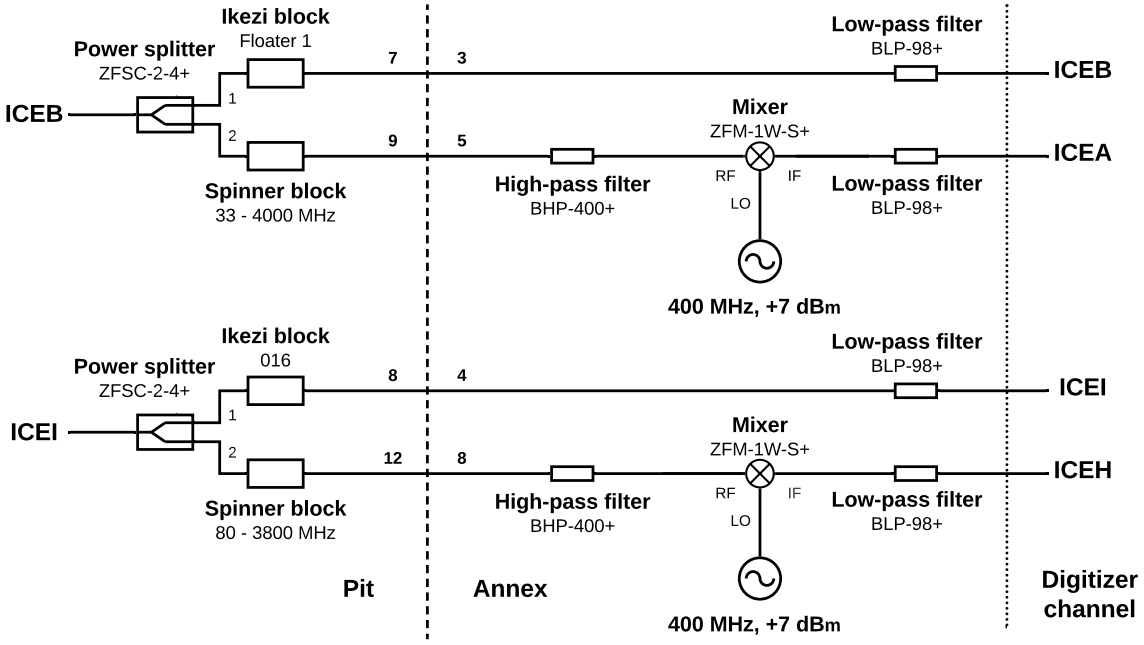

Figure 3.11: Example of a high-frequency ICE configuration, in which two ICE channels are split and mixed down from the 400-500 MHz range to be digitized.

The schematic for the original HICE configuration is shown in Fig. 3.11, where signal from

two ICE channels is split in the machine hall using Mini-Circuits ZFSC-2-4+ power splitters, as shown on the left-hand side of the figure. This signal then either passes through the default ICE DC blocks (marked as Ikezi blocks in the figure) or through broadband DC blocks (manufactured by Spinner GmbH in Munich, Germany) that feature an upper cutoff frequency of $\sim$4 GHz. The latter broadband signal passes into the annex and through a highpass filter before becoming the RF input into a Mini-Circuits ZFM-1W-S+ mixer. The local oscillator (LO) signal comes from a signal generator set at 400 MHz at +7 dBm. The resulting intermediate frequency (IF) output passes through a Mini-Circuits BLP-98+ 100 MHz low-pass filter before being digitized. In total, the above configuration results in two channels that can observe frequencies above the Nyquist frequency of the digitizer in 100 MHz intervals.

Initial measurements using this configuration during early helicon experiments are detailed in Appendix C, and analysis of said data is presented in [133, 132, 160]. Additional DC blocks have been purchased, and this configuration has become more variable. This and similar HICE configurations have been used in continued helicon studies [160] and to look at runaway electron-driven modes.

Chapter 4

Mode structure measurements of ICE and sub-cyclotron modes

This work aims to augment measurements of frequency and amplitude that have been made previously on DIII-D [6, 55, 78, 127, 165, 163, 164] with estimates of mode polarization and spatial structure. Moreover, upgrades to the NBI system on DIII-D (detailed in Chapter 3.1.2) have allowed for greater flexibility in tailoring the properties of the injected fast ion population [75]. A dedicated experiment took place in January 2021 on DIII-D to explore both core and edge ICE in deuterium L- and H-mode plasmas with deuterium NBI, building on previous studies (as described in Chapter 2.1.3) by implementing new diagnostic capabilities to determine mode structure [46]. While the main focus of this work is to investigate the spatial mode structure of ICE, the theory is not yet developed and as such it is useful to examine sub-cyclotron modes as comparison cases, as discussed in Chapter 2.1.3.

Chapter 4.1 outlines the L- and H-mode plasmas in this particular experiment. Chapter 4.2 explores the effects of vertically tilting the neutral beams. Chapter 4.3 explores polarization measurements of ICE and sub-cyclotron modes, followed by Chapter 4.5 discusses centerpost

and outer wall loop comparisons to evaluate the poloidal extent of the mode structure for both core and edge ICE. Chapter 4.4 explores toroidal mode number calculations for sub-cyclotron modes and core ICE.

4.1 Dedicated experiment on DIII-D

The L-mode plasmas in this experiment were of a diverted upper single null (USN) shape (Fig. 4.1(a)) with the ion ∇B and curvature drifts directed away from the divertor to prevent accessing H-mode. These shots had toroidal magnetic field strengths of $B_T = 1.25$ and 2.17 T, plasma current of $I_P = 0.6$ MA, core electron densities of $n_e \in [1.5, 3] \times 10^{13}$ cm^{-3}, and core electron temperatures of roughly $T_e \in [1, 3]$ keV (Fig. 5.1(c)). The effective ion charge of the plasma was $Z_{eff} \simeq 2$ throughout the main phase of the shot, which is expected of a largely deuterium plasma with slight amounts of carbon from the first wall armor and a negligible hydrogen population ($^{n_H}/_{(n_H+n_D)} < 5\%$). The ratio of the beam ion speed to Alfvén speed $^{v_b}/_{v_A}$ (evaluated at the magnetic axis) was varied by changing B_T, n_e, and the beam energy. For the 81 keV co-I_P, on-axis, near-tangential beam considered for much of this paper, $^{v_b}/_{v_A}$ ranged from roughly 0.4–0.6.

The H-mode plasmas in this experiment were of a diverted lower single null (LSN) shape (Fig. 4.1(a)), with B_T of either 1.65 or 1.95 T, $I_P = 0.95$ MA, $q_{95} \in [5, 5.8]$, $\beta_N \in [1.75, 3]$, $n_e \in [1.5, 6] \times 10^{13}$ cm^{-3}, and $T_e \in [1, 2.5]$ keV. These shots started in L-mode and transitioned to H-mode around 1550–1600 ms (determined by a sharp decrease in D_α signal), and consequently ICE localization shifted from near the magnetic axis to around the LCFS. In the shot in which much of the subsequent analysis was focused, it should be noted that an n = 2 tearing mode arose in concert with the L-H transition and was present throughout the rest of the discharge—however, the ratio of energy stored in the fast ion population to the total plasma energy remained at roughly $^{W_{\text{fast}}}/_{W_{\text{MHD}}} \sim 15\%$ for the entirety of the H-mode

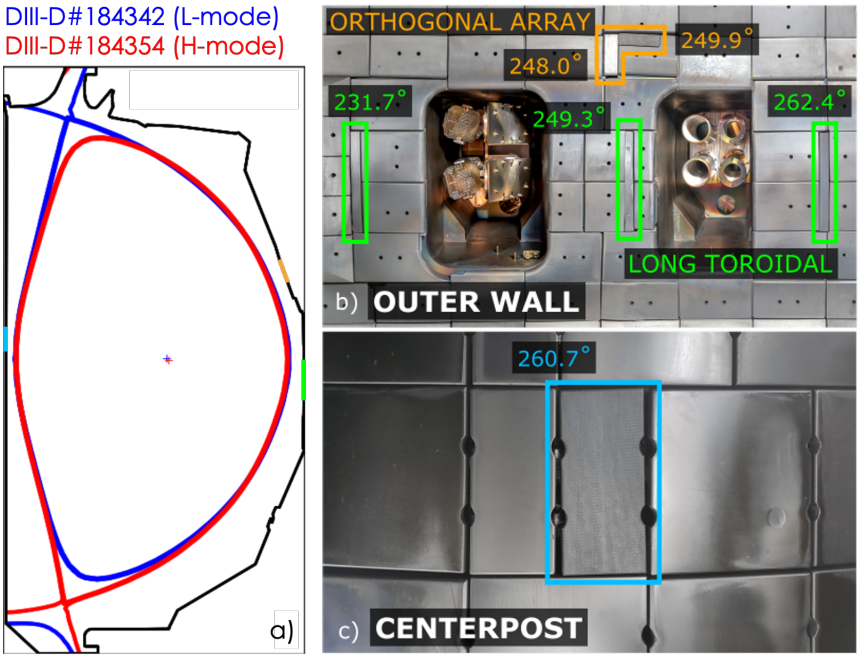

Figure 4.1: (a) Plasma shape for the L-mode (blue) and H-mode (red) plasmas with ICE loop locations roughly indicated by highlighted sections of the first wall armor. (b) All ICE loops on the LFS of the machine and (c) one of two HFS loops (second not pictured).

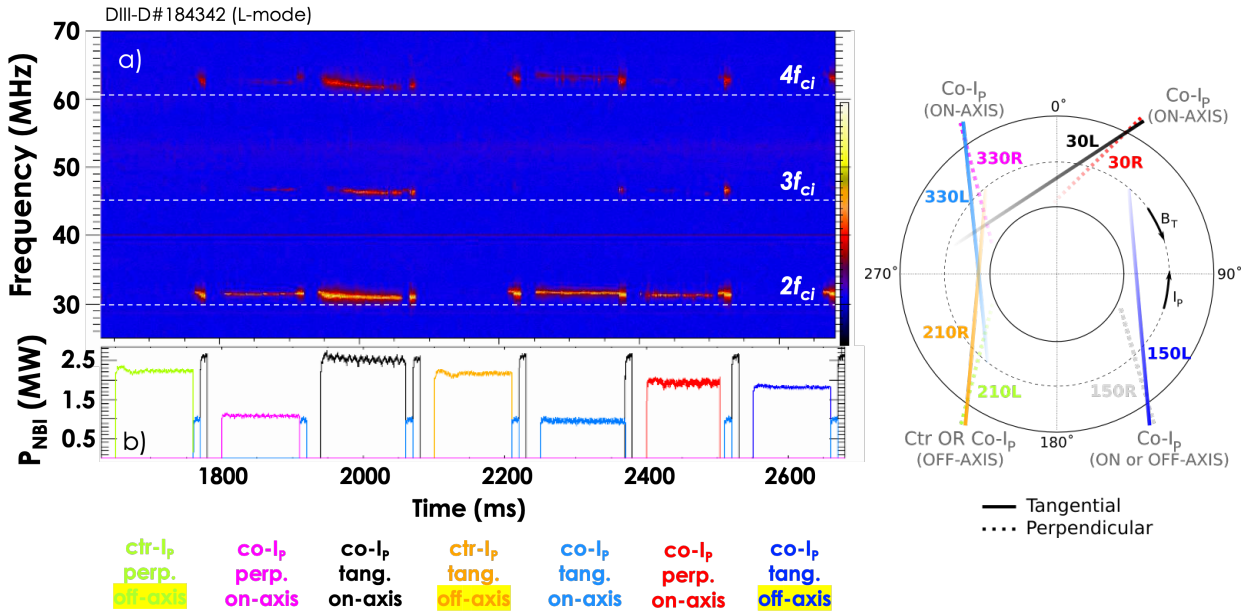

Figure 4.2: (Left) Second, third, and fourth harmonic ICE excited by different NBI geometries that were individually cycled in an L-mode shot on DIII-D. Colors here correspond to those in the figure depicting an aerial view of the DIII-D beams (right).

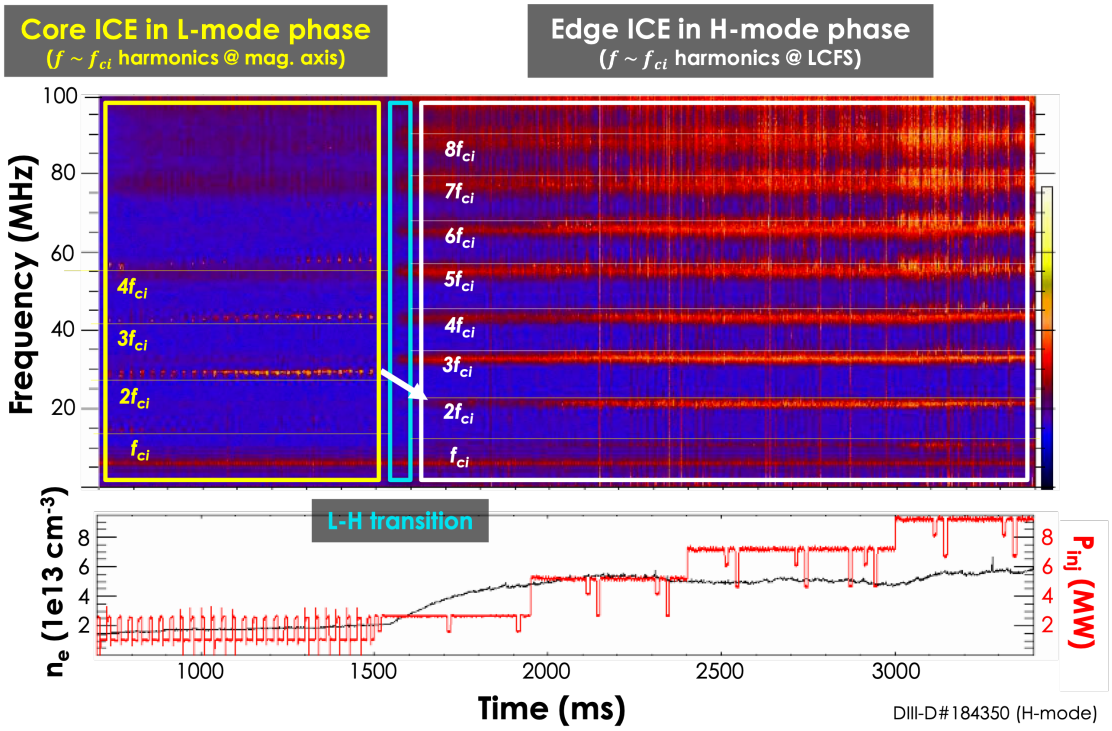

Figure 4.3: (a) An example of an H-mode shot exhibiting both core and edge-localized ICE, where horizontal lines have been overlaid to indicate f_{ci} evaluated at the magnetic axis in L-mode (yellow) and the LCFS in H-mode (white). The shot begins in L-mode (left), with the neutral beams exciting core ICE harmonics 1–4 f_{ci}. After the L-H transition, harmonics 1–9 f_{ci} are excited and localized near the plasma edge. Noise at roughly 5 MHz is observed throughout the discharge and is likely caused by the power supplies. (b) NBI power (MW) in red and electron density n_e (1e13 cm^{-3}) in black.

phase, indicating that the tearing mode did not induce appreciable fast ion losses.

The toroidal LFS loop used for autopower spectrum measurements presented in this work is located at $\phi = 248.0°$ (Fig. 4.1(a), orange) and the toroidal HFS loop at $\phi = 260.7°$ (Fig. 4.1(b)). These two loops are somewhat displaced (toroidally by $\sim 12.7°$, vertically by roughly 12.3 cm), and the effects of eddy currents are assumed to be negligible. The long LFS toroidal loops used to calculate toroidal mode numbers are at a lower vertical position near the midplane of the machine, and the possible loop pairs are separated toroidally by $\Delta\phi = 13.1$, 17.6, and 30.7°. As the digitizer employed by this diagnostic has a sampling rate of 200 MSamples/s, 100 MHz lowpass filters (Mini-Circuits BLP-100+) were used for both the small poloidal and toroidal loop channels in an attempt to suppress $f > 100$ MHz

aliased signals. These filters nominally have a DC–98 MHz passband and 3 dB f_{cutoff} of 108 MHz [118].

Though none of the loops are absolutely calibrated, the HFS and small LFS loops' signals are expected to be comparable, considering cable losses and loop area size (15 and 19 cm^2, respectively). Furthermore, all ICE channels are dispersionless in the frequency range considered here and have extremely similar frequency responses (including all components from the in-vessel loops to the cables in the annex as illustrated in [46]).

4.2 Core ICE dependence on on- vs. off-axis beams

Core ICE depends strongly on the NBI configuration, with high-powered on-axis beams typically driving the strongest ICE [165]. The effect of on- and off-axis beams was only considered here for core ICE as edge ICE does not exhibit such a clear dependence on beam geometry [165]. Both the near-tangential and near-perpendicular on-axis, co-I_P beams typically excite the first through the fourth ICE harmonics, and the second harmonic customarily has the highest amplitude. The co-I_P beams that were tilted off-axis in previous experiments did not drive ICE, and this was reproduced in the recent experiment. Table 4.1 summarizes the core ICE harmonics excited by the available beam geometries, including data from both this recent experiment and historical data [172]. In particular, the autopower spectrum from the small toroidal loop (Fig. 3.5(a)) was time-averaged over the course of 100 ms pulses from on-axis, co-I_P, near-tangential beams at 2.5 MW and 1.0 MW (81 keV and 55 keV, respectively) in Fig. 4.4(a). Despite these on-axis beams having different powers and voltages, they excited nearly the same spectrum of core ICE at 2–4f_{ci}. However, the off-axis, co-I_P, near-tangential beam at a moderate 1.7 MW (80 keV) did not excite any ICE (Fig. 4.4(b)).

The classical fast ion distribution was calculated for each beam using the TRANSP transport

a) **CO-I_p BEAMS**

	High power		Low power	
On-axis	Near-tangential 2nd – 4th	Near-perpendicular 2nd	Near-tangential 2nd & 4th	Near-perpendicular 2nd
Off-axis	Near-tangential none	Near-perpendicular none	N/A	N/A

b) **CTR-I_p BEAMS**

	High power		Low power	
On-axis	Near-tangential 1st – 7th	Near-perpendicular 1st & 2nd	N/A	N/A
Off-axis	Near-tangential none	Near-perpendicular none	N/A	N/A

Table 4.1: Table of core ICE harmonics excited by various neutral beam geometries available in both this experiment and historical ICE experiments, for both the (a) co-I_P and (b) ctr-I_P beams. The colors correspond to those used in Fig. 4.2 for the individual beam configurations. Note, harmonic amplitudes are not included in this table.

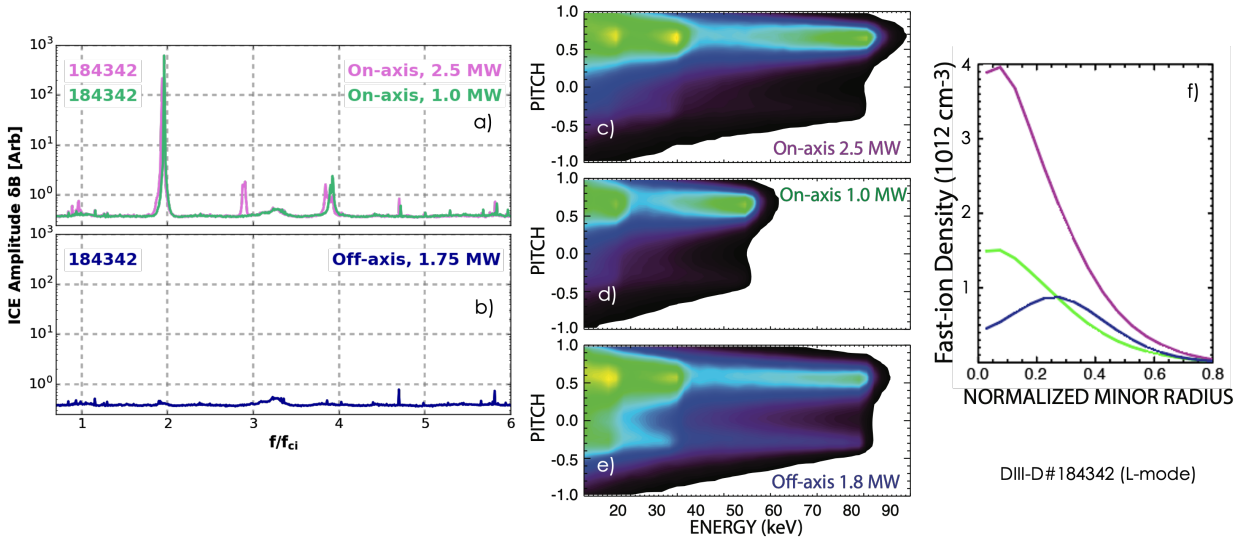

Figure 4.4: Time-averaged autopower spectrum over the course of a 100 ms pulse from co-I_P, co-tangential beams, which were (a) on-axis at 30° and 330° and (b) off-axis at 150°. f_{ci} is evaluated at the magnetic axis. The fast ion distribution velocity profile for each beam pulse is depicted in (c), (d), and (e), where the relative value of the color scale is 1.0, 0.60, and 0.24, respectively. The spatial profile, taken by summing the fast ion distributions in velocity space, is presented in (f).

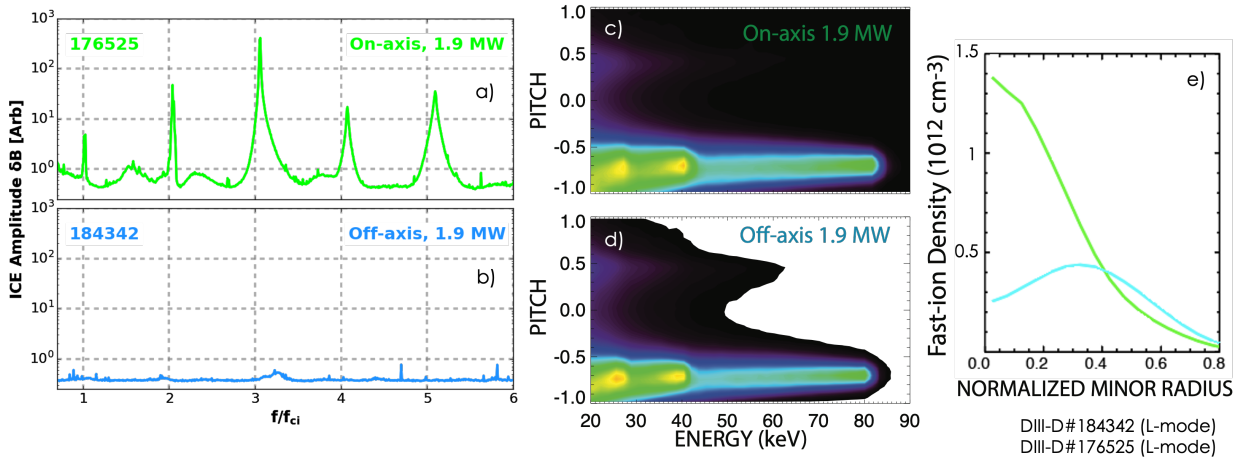

Figure 4.5: Time-averaged autopower spectrum over the course of a 100 ms pulse of the ctr-I_P, near-tangential beam at 210° when it was (a) on- and (b) off-axis in 2018 and 2021, respectively. Again, f_{ci} is evaluated at the magnetic axis. The velocity profile for each beam pulse is depicted in (c) and (d), where the relative value of the color scale maximum is 0.53 and 0.26, respectively. The spatial profile, taken by summing the fast ion distributions in velocity space, is presented in (e).

code [17], making use of the NUBEAM Monte Carlo module [128]. This same analysis process was used in [165], however those studies predate the ctr-I_P beams being tilted permanently off-axis. The distributions were first integrated over all Z and R over 165–190 cm in the core to ascertain the velocity space distributions depicted in Fig. 4.4(c-e). The differences in the distribution as averaged over all Z and over $|Z| < 15$ cm in the core were negligible. The velocity distributions for the high-power on-axis (Fig. 4.4(c)) and off-axis (Fig. 4.4(e)) were similar, though clearly they did not excite the same ICE spectra. The spatial profiles for each beam were also calculated by integrating over velocity space, and it was in these profiles that a notable difference between the on- and off-axis high-powered beams was present. While both the high- and low-powered on-axis beams had spatial profiles that were peaked in the core of the plasma, the off-axis beam spatial profile was peaked off-axis.

In comparison to the co-I_P beams, the on-axis, near-tangential, ctr-I_P beam historically has excited harmonics 1–7f_{ci} [165], with the third harmonic being dominant and all harmonics being broader in frequency than harmonics excited by the co-I_P beams (Fig. 4.5(a)). Simi-

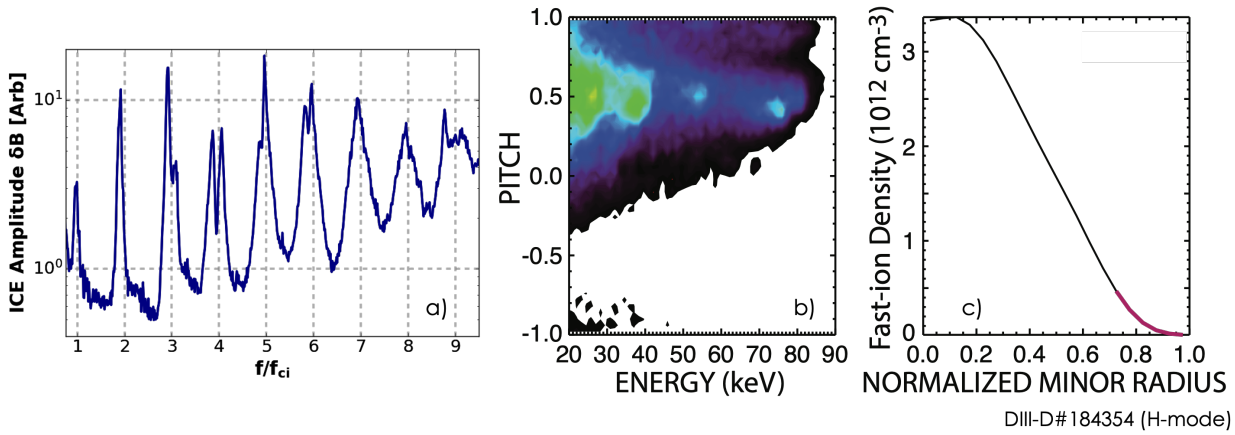

Figure 4.6: (a) Autopower spectrum from an H-mode plasma time-averaged over a period of constant injected beam power, during which ELMs are present. f_{ci} is evaluated at the LCFS. (b) The velocity profile and (c) spatial profiles, the latter with a red highlight depicting the $R > 219$ cm area of interest.

larly to the co-I_P beams, when the ctr-I_P beam was tilted off-axis (Fig. 4.5(b)) all ICE modes were completely suppressed. Again, the fast ion distributions for each beam were integrated over Z and R in the core to obtain the velocity space distribution, and over configuration space for the spatial profiles. The velocity distributions (Fig. 4.5(c) and (d)) were extremely similar for both the on- and off-axis, but the spatial profiles were reminiscent of those of the co-I_P beams. Evidently, change in the spatial profile was important in the disappearance of core ICE.

For comparison, an example of time-averaged edge ICE and the corresponding velocity (averaged over $R > 219$ cm to cover the edge of the plasma) and spatial profiles is shown in Fig. 4.6. Notably, in the area of interest (highlighted in dark red in Fig. 4.6(c)), the fast ion density was low ($\lesssim 0.5 \times 10^{12}$ cm^{-3}) and yet multiple edge ICE harmonics were present. It has been found previously that, contrary to core ICE, exciting edge ICE does not necessarily require many fast ions. There are multiple examples of edge ICE on other machines including JET [38], TFTR [24, 23], JT-60U [85], and KSTAR [29, 28] driven by extremely low concentrations of fusion products, which are of inherently higher energy than NBI ions. Furthermore, edge ICE may have a different underlying excitation mechanism.

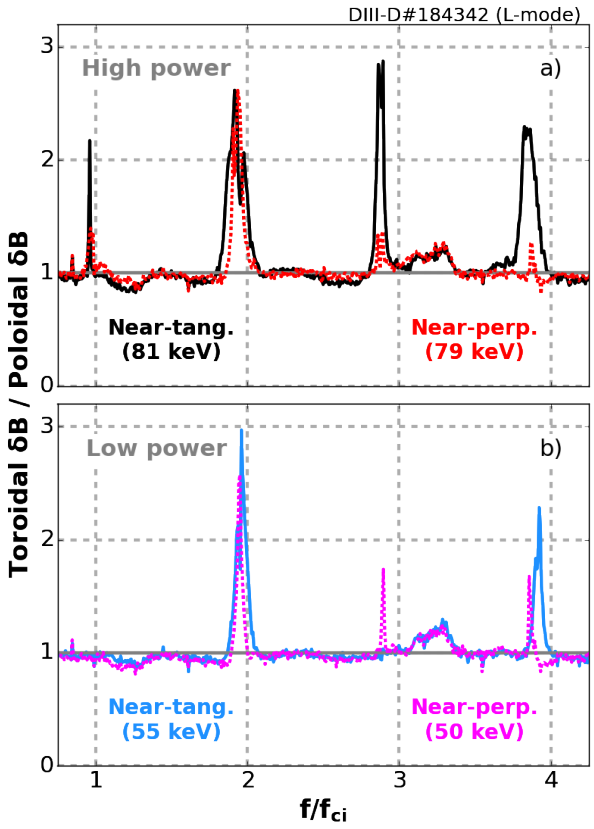

Figure 4.7: Polarization estimates ($^{\delta B_{tor}}/_{\delta B_{pol}}$) at the plasma edge as calculated for core ICE excited by on-axis, co-I_P neutral beams. (a) High-power near-tangential (solid black) and near-perpendicular (dashed red) beams. (b) Low power near-tangential (solid blue) and near-perpendicular (dashed magenta) beams. f_{ci} is evaluated at the magnetic axis.

4.3 Polarization at the plasma edge

The main aim of these experiments was to characterize the spatial structure of the modes. Mode polarization ($^{\delta B_{\parallel}}/_{\delta B_{\perp}}$) at the plasma edge can be approximated by comparing measurements from the toroidal and poloidal loop pair on the outer wall (Chapter 3.2.2, Fig. 3.5(a)). Both loops have nearly identical loop areas and similar cable losses such that they are comparable despite neither being absolutely calibrated, and each has an antialiasing filter. The ratio $^{\delta B_{tor}}/_{\delta B_{pol}} \sim {}^{\delta B_{\parallel}}/_{\delta B_{\perp}}$ is calculated by time-averaging the autopower from each loop over a select time window and then dividing the toroidal autopower by the poloidal autopower. A roughly compressional polarization at the plasma edge corresponds to $^{\delta B_{tor}}/_{\delta B_{pol}} > 1$, and

$\delta B_{tor}/\delta B_{pol} < 1$ suggests shear polarization. Note that these measurements are of polarization at the plasma edge; it is entirely possible—even likely in some cases—that the dominant polarization of the mode in the core of the plasma is different from the polarization at the edge.

Data from the orthogonal pair was time-averaged over the course of a variety of on-axis beam pulses that drove core ICE in the $B_T = 2.17$ T plasma. For all beams that drove ICE, a ratio of $\delta B_{tor}/\delta B_{pol} > 1$ was found near the coils for the first, second, third, and fourth harmonics (as depicted in Fig. 4.7), indicating compressional polarization at the plasma edge. However, there was some variation between beams. Core ICE excited by the high-power near-tangential beam (Fig. 4.7(a) in black) exhibited ratios $\delta B_{tor}/\delta B_{pol} > 2$ at the plasma edge for all harmonics. In contrast, the similarly high-powered near-perpendicular beam (Fig. 4.7(a) in red) had $\delta B_{tor}/\delta B_{pol} > 2$ only for the second harmonic and then $\delta B_{tor}/\delta B_{pol} \sim 1$ for all other harmonics. The low-powered beams (Fig. 4.7(b)) also exhibited $\delta B_{tor}/\delta B_{pol} > 2$ for the second harmonic, but somewhat lower ratios for the third and fourth harmonics. It should be noted that the autopower spectrum amplitude for harmonics other than the second were quite low for both the toroidal and poloidal loops, and it is likely that background noise was affecting edge polarization ratios calculated for non-dominant harmonics in Fig. 4.7.

Time-averaging over a window of constant beam power during an H-mode shot (Fig. 4.8(a)), the ratio at each edge ICE harmonic peak was found to be $\delta B_{tor}/\delta B_{pol} \gtrsim 2$ for harmonics $f = 1$–$7 f_{ci}$ (Fig. 4.8(b)). For harmonics $8 f_{ci}$ and above, the ratio was still $\delta B_{tor}/\delta B_{pol} \gtrsim 1.5$ but the peaks were less distinct. It is likely that, as edge ICE in H-mode plasmas was generally of high amplitude, the lowpass filters were not sufficient to suppress aliased signals and thus there was a combination of $f \lesssim 100$ MHz and $f \lesssim 100$ MHz peaks for $f/f_{ci} \gtrsim 8$. These findings indicate that edge ICE was compressionally polarized at the plasma edge. However, it should be noted that this edge polarization measurement may not be indicative of the dominant mode polarization, nor of the overall structure of the mode. For example,

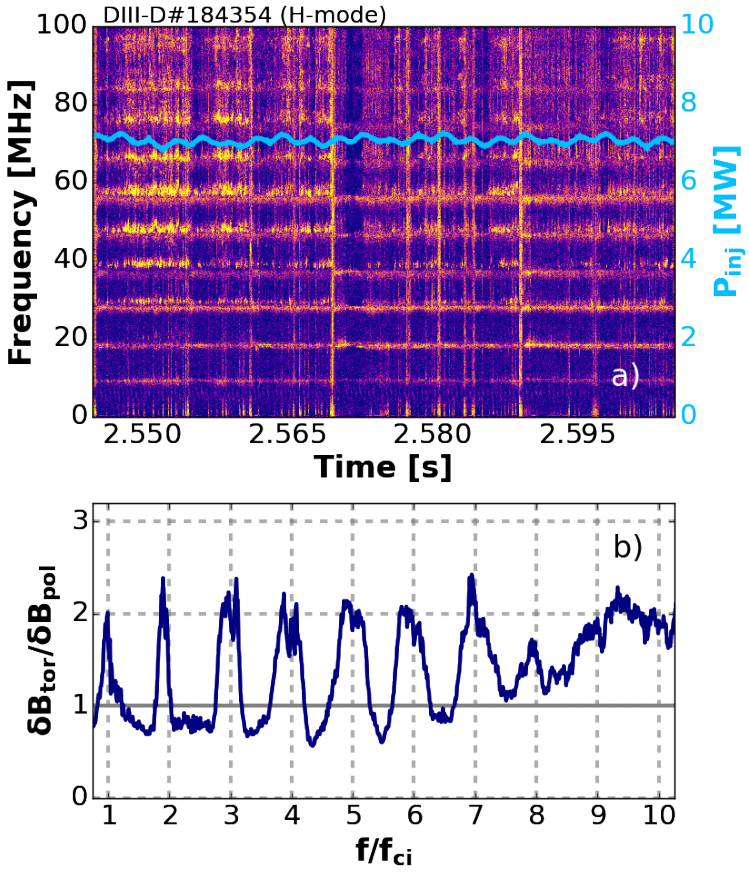

Figure 4.8: (a) Edge ICE excited in an H-mode plasma, where the injected beam power P_{inj} is overlaid in light blue. (b) Polarization $^{\delta B_{tor}}/_{\delta B_{pol}}$ at the plasma edge as calculated from the small toroidal and poloidal outer wall loops. In this case, f_{ci} is evaluated at the LCFS.

despite these compressional edge polarization measurements, the mode was not likely a CAE, as the high k wavenumber measured by the high-frequency Doppler backscattering (DBS) system suggests that the modes were likely driven by the MCI or an electrostatic wave [41]. Compressional polarization at the plasma edge has also been observed for ICE and chirping ICE (ch-ICE) on NSTX(-U) [60, 61]. However, the ratio of toroidal and poloidal amplitude measured on TFTR was highly variable, and no definitive conclusions could be drawn regarding mode polarization aside from the general observation that the toroidal and poloidal components were roughly the same [25].

Finally, sub-cyclotron modes were also studied in this experiment. An example of such a

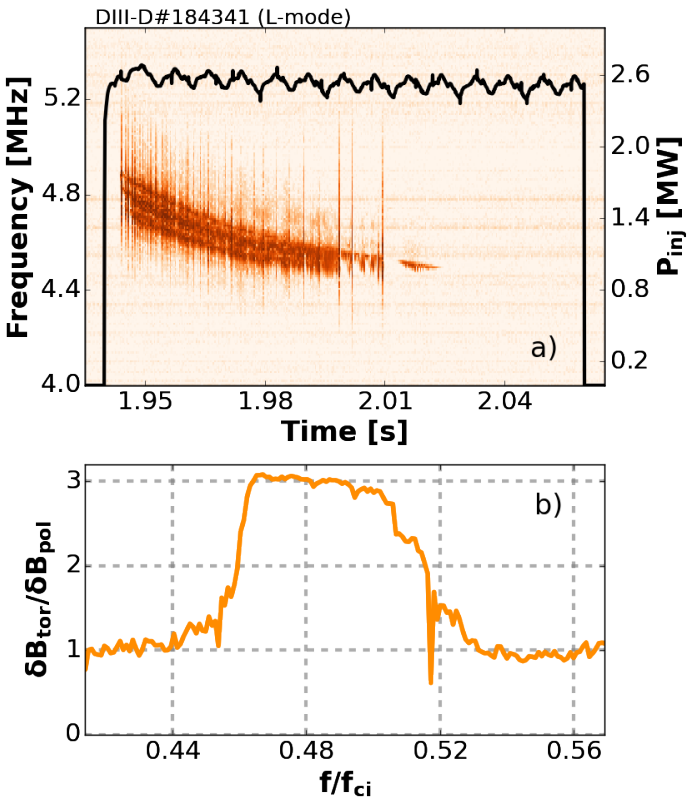

Figure 4.9: (a) Spectrogram calculated from small toroidal loop data, illustrating a sub-cyclotron mode at $\sim 0.5 f_{ci}$ excited by the 2.5 MW on-axis, near-tangential beam (overlaid in black). (b) Ratio of small toroidal and poloidal loop autopower. Here, f_{ci} is evaluated at the magnetic axis.

mode on DIII-D is depicted in Fig. 4.9(a), where the the high-power, co-I_P, near-tangential, on-axis beam excited sub-cyclotron modes at a lower magnetic field strength of $B_T = 1.25$ T. The mode was destabilized 4 ms after the beam turns on and was stabilized at around t = 2.02 s, roughly halfway through the beam pulse. While mode stability is not the focus of this work, we will note that stabilization of the mode while the beam remains on, particularly in the absence of a current ramp, conflicts with previous experiments on DIII-D [161]. This could indicate that a positive energy gradient, in addition to the usually larger contribution from fast ion anisotropy, was needed for the drive of this mode to overcome background damping in this particular shot. Here, multiple discrete, closely spaced, spectral lines were present that swept down in frequency over the time averaging window, so a wide peak was

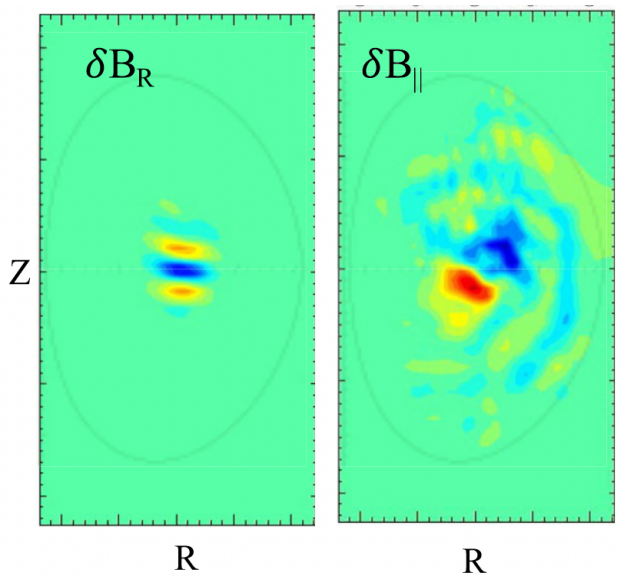

Figure 4.10: GAE parallel and perpendicular magnetic fluctuation amplitudes simulated for DIII-D relevant conditions using the 3D hybrid code HYM. Figure taken from [10].

observed in the averaged data (Fig. 4.9(b)). As with the previous core ICE example, the autopower from both the toroidal and poloidal loops was time-averaged over the duration of the beam pulse. As $^{\delta B_{tor}}/_{\delta B_{pol}} \sim 3$ (Fig. 4.9(b)), the mode was predominately compressional at the plasma edge.

Again, these edge polarization measurements, while valuable for constraining future modeling, do not necessarily reflect the dominant polarization of the modes, which may have larger amplitude closer to the core [39]. For instance, simulations of NSTX(-U) using the 3D hybrid code HYM [13, 12, 103], illustrated in Fig. 4.10, consistently find that both GAEs and CAEs have a large compressional fluctuation in the edge, despite having very different polarization in the core ($\delta B_\perp \gg \delta B_\parallel$ for GAEs vs $\delta B_\parallel \gg \delta B_\perp$ for CAEs) [13, 12, 103]. This finding, which is consistent with experimental measurements of GAEs and CAEs in NSTX [40, 58, 63], is attributable to strong coupling between the shear and compressional branches of the dispersion due to spatial gradients in the equilibrium profiles near the edge. Consequently, sub-cyclotron modes cannot be distinguished between shear and compressional modes on the basis of edge polarization measurements alone. Furthermore, it should

be noted that direct comparison to spherical tokamaks is difficult as the field at the outer wall shifts more in spherical tokamaks than in conventional tokamaks (relative to where the mode is excited) because the equilibrium field changes pitch more. More definitive identification can be achieved by appealing to the resonance condition, dispersion relation, and/or more sophisticated modeling, which concluded that sub-cyclotron modes in DIII-D were most likely GAEs [10, 161].

4.4 Toroidal mode numbers

Signals from the three long loops on the outer wall (Fig. 3.5(a) in Chapter 3.2.2) were used to estimate toroidal mode numbers for a few select cases of both sub-cyclotron modes and ICE. The long cables required to transfer signal from the machine hall to the annex introduce phase shifts that scale linearly with frequency and thus are appreciable for the frequency ranges of interest ($\gtrsim$ 10 MHz). These time delays (typically in the range $\tau \sim$ 200–300 ns) were measured [126] and were subtracted from the raw time series data such that all channels were on the same time base. The coherence and cross-power were calculated for each possible loop pairing, using both the time-averaging and frequency-smoothing techniques outlined in Chapters 3.3.1 and 3.3.2 [15, 16]. In this work, only points with a coherence higher than 80% were selected, and then for each point the toroidal mode number was determined by fitting the slope between the cross-phase and angular displacement for each probe pair and selecting the fit with the lowest $\chi^2_{reduced}$ value. This phase fitting method is outlined by Ferron, Strait, and Kim [57, 90]. Though the closest spacing between any of the loop pairs (13.1°) would normally translate to a nominally maximum resolvable toroidal mode number $|n| \sim 13$, the third loop pair can help resolve higher numbers that otherwise might be subject to spatial aliasing. Thus, even toroidal mode numbers $|n| > 13$ could be considered for each time and frequency, and generally the value of n with the lowest associated $\chi^2_{reduced}$ value

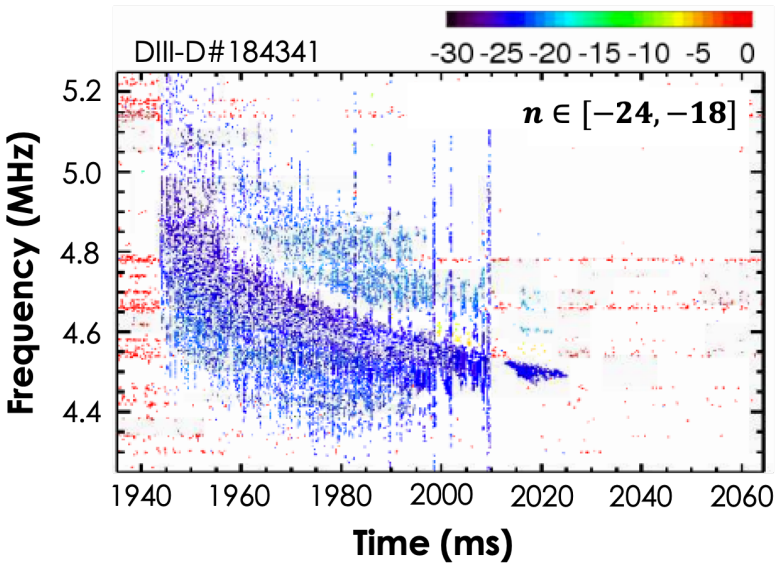

Figure 4.11: Toroidal mode numbers calculated for sub-cyclotron modes excited in a $B_T = 1.25$ T, L-mode plasma using the three long toroidal loops (Fig. 3.5(a)) and the frequency-smoothing technique. Here, $n \in [-20, -15]$, so the modes are counter-propagating with respect to the direction of I_P and beam injection.

was selected as the most probable. The effects of eddy currents are assumed to be negligible as the loops are of identical design, located at nominally the same poloidal position, and are surrounded by similar graphite first wall tiles. Finally, n is assumed to be well defined for a given eigenmode and thus can be measured at any radius, including at the wall.

Sub-cyclotron mode structure has been more widely explored in literature than ICE and served as a benchmark to ensure that our toroidal mode number calculation technique was sound. Considering the same case as depicted in Fig. 4.9(a) and assuming these are GAEs as per previous DIII-D studies in comparable conditions [10, 11, 12, 161], heuristic estimates were made for the expected toroidal mode numbers. As derived in Appendix B, the two-fluid dispersion relation for shear waves gives:

$$-\frac{R\omega_{cb}}{v_A}\frac{1}{\sqrt{1-{}^{\omega}/_{\omega_{ci}}}} < n < -\frac{R\omega_{cb}}{v_A}\frac{1}{\sqrt{1-{}^{\omega^2}/_{\omega_{ci}^2}}} \tag{1}$$

Note that the upper and lower bounds are not strict, but rather represent a spread due

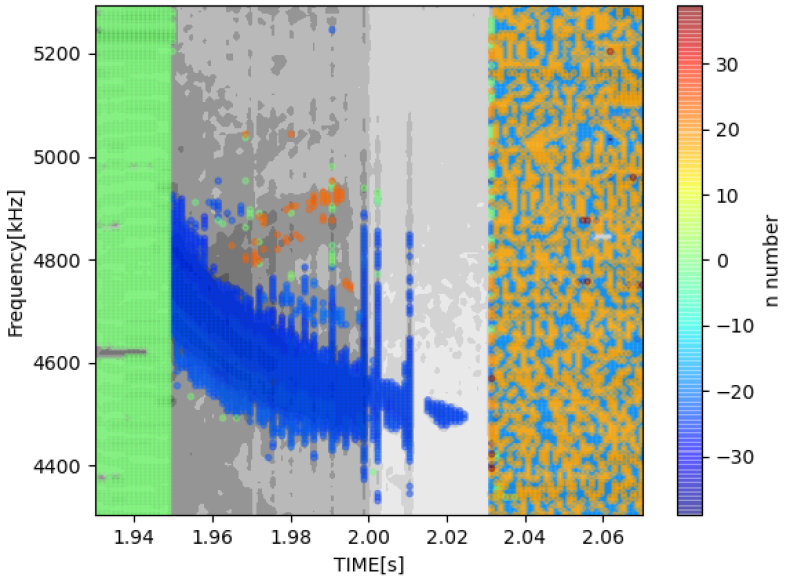

Figure 4.12: Toroidal mode numbers calculated for the same case as in Fig. 4.11, except with the time-averaged method.

to lack of knowledge of the direction of the wavevector ($k_\parallel/k_\perp$), which was not measured. Thus, for the observed mode frequencies of $\omega/\omega_{ci} \in [0.3, 0.52]$ with values of $R = 1.72$ m and $n_e \sim 2.2\times10^{13}$ cm^{-3} near the magnetic axis, we expected the range of toroidal mode numbers to be $n \in [-20, -13]$. Here, the negative sign indicates mode propagation counter to the plasma current and the direction of beam injection. These heuristic estimates assume that the modes are centered about the magnetic axis, though it should be noted that simulations of similar modes on DIII-D indicate that the modes may be extended both radially and poloidally [10, 11, 103]. The toroidal mode numbers as determined through cross-phase data calculated via frequency-averaging and time-smoothing are depicted in Figs. 4.11 and Fig. 4.12, respectively. The former method resulted in mode numbers in the range $n \in [-24, -18]$ and the latter gave $n \in [-25, -20]$, which both roughly agreed with heuristic estimates. These values also agreed with HYM simulation results for comparable DIII-D plasmas, where the $n = -23$ counter-propagating GAE was found to be most unstable [10].

Similar toroidal mode number bounds cannot be heuristically estimated for ICE, as elaborated in the appendix. However, as there was rough agreement between measured and

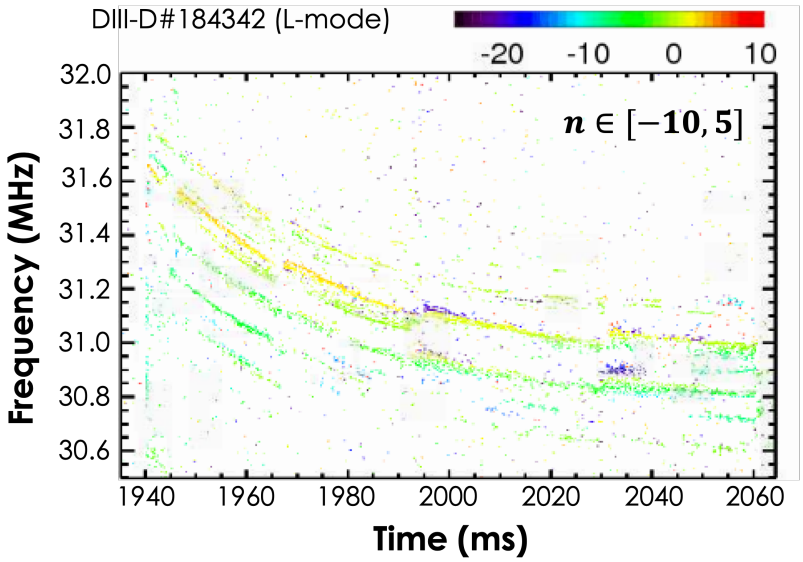

Figure 4.13: Toroidal mode numbers for the core ICE case in a $B_T = 2.17$ T, L-mode plasma, where a range of $n \in [-10, 5]$ indicates that there is a mix of co- and counter-propagating modes.

expected mode numbers in the sub-cyclotron case, it was reasonable to apply the same calculation technique to ICE cases. Considering the high-powered beam case from Fig. 3.9 at $B_T = 2.17$ T resulted in toroidal mode numbers $n \in [-10, 5]$, with $n \in [-3, 2]$ being the most persistent through the beam pulse (Fig. 4.13). Frequency bands depicted in Fig. 4.13 were spaced ~ 150 kHz apart. In this case, there was a mix of co- and counter-propagating modes with respect to I_P and NBI direction. Similar ranges of $n \sim [-10, 5]$ were observed for all three other on-axis, co-I_P beams. Though not directly comparable due to the different nature of ICE observed, toroidal mode number measurements made on other machines are in the same range as those made on DIII-D. Mode numbers calculated for ch-ICE on NSTX(-U) in the range $n \in [-4, -1]$ [60] are comparable to those observed for core ICE on DIII-D. Measurements of edge ICE (both beam- and fusion product-driven) on JT-60U and core ICE on AUG are also similar with $|n| \leq 3$ [85] and $n = 0$ [122], respectively.

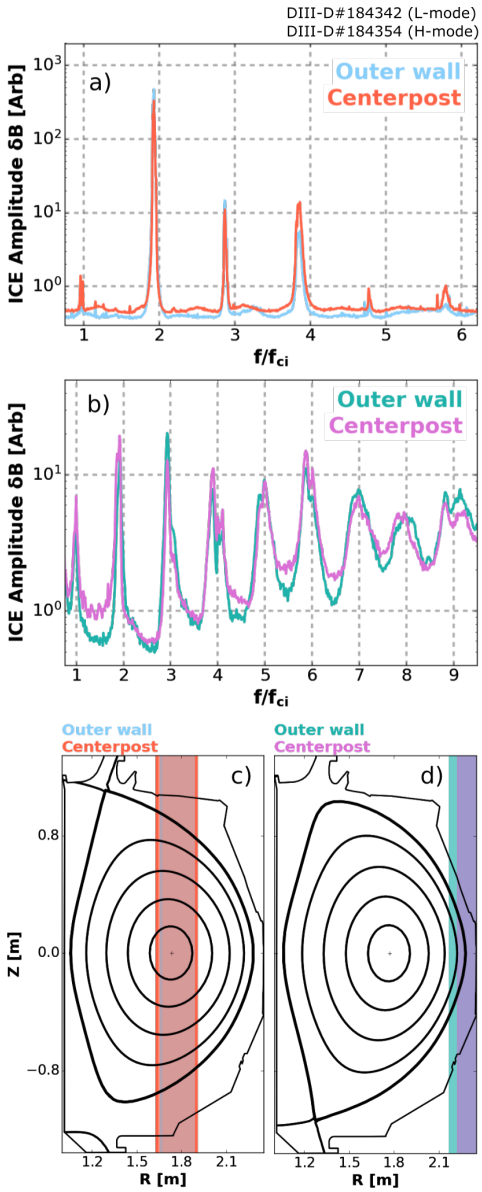

Figure 4.14: (a) Core ICE as measured by a toroidal loop on the centerpost (red) and the small toroidal loop on the outer wall (blue). Here, f_{ci} is evaluated at the magnetic axis. (b) Edge ICE as measured by the centerpost (orchid) and outer wall (teal) loops, with f_{ci} evaluated at the LCFS. (c) Equilibrium reconstruction with rough core ICE emission radii for outer wall and centerpost measurements. (d) Edge ICE equilibrium and emission radii.

4.5 Centerpost vs. outer wall measurements

The autopower as determined from toroidal loops located on the low and high field sides of the machine can be compared to determine whether the modes are poloidally extended or if they originate from a point close to a detecting loop. An example of core ICE as measured by a small toroidal loop on the outer wall (Chapter 3.2.2 Fig. 3.5(a)) and the centerpost (Fig. 3.5(b)) is shown in Fig. 4.14(a). The peaks detected by these outer wall and centerpost loops were nearly identical in frequency and comparable in amplitude, indicating that the modes were poloidally extended. Small temporal differences between inboard and outboard amplitude envelopes of $\sim$ 25 μs were sometimes observed, but these differences were not significant enough to suggest that the modes are constrained to small poloidal region. Using the dominant peak from the centerpost and outer wall loops in conjunction with equilibria generated using EFIT [98], the rough emission radius was found to be 1.77 m for both as illustrated in Fig. 4.14(c), where both the red and blue emission regions overlapped in the core. As in previous works, these radii were determined by finding the location where $f_{ci}(R)$ matched the frequency separation of peaks in the observed spectrum. As the total magnetic field strength is nearly independent from vertical position Z in DIII-D [165], the vertical emission location cannot be determined. The Doppler shift of the ICE peaks was assumed small enough to be neglected when determining these rough emission locations.

This same comparison waws made for edge ICE (Fig. 4.14(b)). Again, very similar modes were observed by both loops for all excited harmonics, suggesting that edge ICE was also poloidally extended. Moreover, recent measurements of edge ICE with the radially resolved high-frequency DBS system found an extended spatial structure over at least 1/6 of the minor radius [41]. Combined with the measurements presented here, it can be concluded that edge ICE has a broad global structure rather than a highly localized eigenfunction. The emission radius as determined from both centerpost and outer wall data occurred at roughly 2.4 m, as illustrated in Fig. 4.14(d) where the teal and purple emission regions for the outer wall

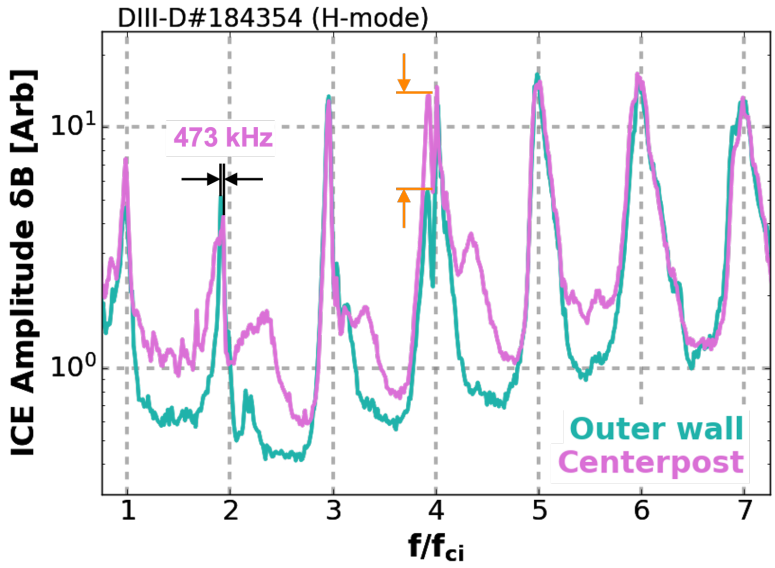

Figure 4.15: Autopower spectra of edge ICE as measured by the centerpost and outerwall loops, where small discrepancies in both frequency and amplitude were observed. For example, there is a difference of roughly 473 kHz between second harmonic peaks, and a significant amplitude difference observed for the fourth harmonics.

and centerpost loops overlapped near the LCFS. However, there were slight discrepancies in both frequency and amplitude (an example of which is depicted in Fig. 4.15), which may shed light on wave propagation through the evanescent layers on the LFS and HFS of the machine. These discrepancies were often on the order of hundreds of kilohertz and thus much larger than the difference expected by the bulk plasma rotation, whose frequency ranged from roughly 2 kHz in the L-mode plasmas to a maximum of $\sim$7 kHz in the core of the H-mode shots analyzed in this work. In the edge of these H-mode shots where ICE appears to be localized, the rotation frequency was $\lesssim 2$ kHz. Investigation of this phenomenon is explored in the next chapter, wherein the plasma shape was manipulated to alter the evanescent layer on the LFS.

ICE has been observed using physically displaced probes on TFTR, AUG, and TUMAN-3M. The former study found that the observed modes did not exhibit a dependence on probe location [23, 24, 25], indicating that the modes are poloidally extended and thus largely corroborating DIII-D findings. However, the small discrepancies in both frequency

and amplitude discussed above were not mentioned in TFTR studies and are discussed in the next chapter. In AUG, the same modes were observed using the LFS and HFS probes, though in the latter case the signal was lower in amplitude [123]. Furthermore, the overall unimportance of probe location seen in TFTR, AUG, and DIII-D studies contrasts with observations of ohmic ICE made on TUMAN-3M [4, 101]. In contrast, observed frequency peaks in TUMAN-3M were significantly different between the two detectors, corresponding to the differences in local magnetic field strength and thus indicating highly localized emission. Hence, beam-driven and ohmic ICE may have substantially different poloidal mode structures.

Chapter 5

ICE dependence on the evanescent layer and fast ion density

Discerning the extent to which ICE frequency, amplitude, and mode structure depend on shifts in the plasma location vs. characteristics of the fast ion population is necessary for ICE to serve as a measure of fast ion properties. Simultaneously, investigating how the size of the vacuum region between the plasma and the pickup loops affects the aforementioned ICE mode properties may inform evaluations of diagnostic sensitivity in future devices. Disentangling all of these effects may help to reconcile experimental observations with synthetic diagnostic measurements in future modeling efforts. This chapter aims to characterize at least some of these effects and motivate further investigations in both DIII-D and future devices.

The effects of both small plasma shifts on core ICE and larger variations in the plasma shape by scanning the distance between the LCFS and the outer wall are investigated in Chapters 5.1.1 and 5.1.2. In Chapter 5.2, the impact of a similar scan in LFS wall proximity on H-mode edge ICE was evaluated. Finally, comparisons of observed and predicted fine-scale ($\delta f < f_{ci}$) frequency splitting for both core and edge ICE are compared in Chapter 5.3.

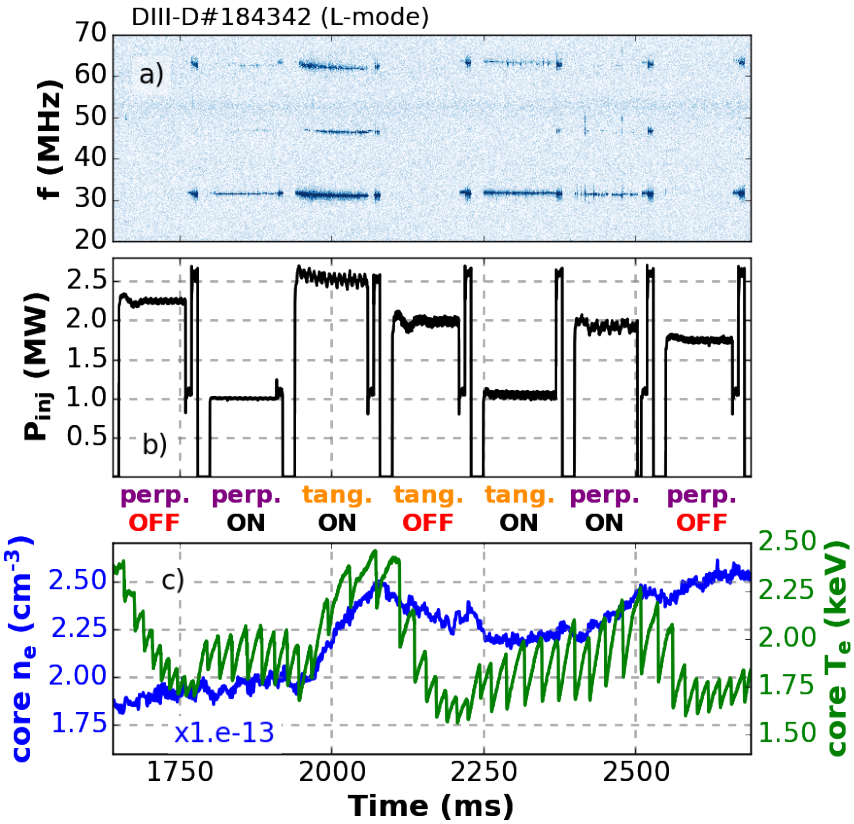

Figure 5.1: (a) Autopower spectrum determined from an outer wall toroidal ICE loop. (b) Injected beam power, as seven different neutral beam geometries were cycled (as described in detail in [45]) for 100–120 ms pulses. The text immediately beneath each pulse ('perp.', 'tang.', 'OFF', 'ON') indicates either nearly perpendicular or tangential injection with respect to the solenoid, and whether the beams are on- or off- axis with respect to the midplane of the machine. (c) Line-averaged core density (blue) as measured by the CO2 interferometer diagnostic [169] and core temperature (green), determined by electron cyclotron emission [5].

5.1 Core ICE in L-mode plasmas

5.1.1 Core ICE in main phase

As discussed in the previous chapter, the main phase of the 2.17 T LSN L-mode shot involved cycling up to seven different NBI geometries, as depicted in Fig. 5.1(a-b). This work largely focused on ICE excited by the 2.5 MW (81 keV) near-tangential, on-axis beam that was pulsed from 1940–2060 ms (Fig. 5.1(b)) as it consistently excited the most ICE harmonics. As illustrated in Fig. 5.1(a), modes appeared at $f/f_{ci} = 2$, 3, and 4, with the second harmonic

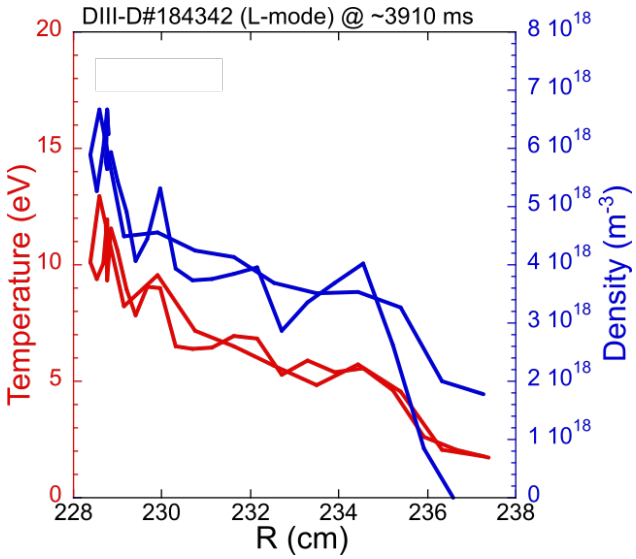

Figure 5.2: Temperature (red) and density (blue) profiles in the SOL as measured by the midplane reciprocating probe. The probe is extended from a $R \sim 237.5$ cm to ∼299.5 cm and then retracted again, and the duplicate lines for both temperature and density depict data collected on both lengths of the journey. During the time period over which the probe was plunged, the radial location of the LCFS at the midplane ranged from roughly 229–232 cm.

having the highest amplitude by a factor of roughly 10. However, these modes did not necessarily occur at a fixed frequency but instead downswept by up to ∼500 kHz throughout the course of a beam pulse (Fig. 5.3(a), (c)). In the case of the aforementioned 2.5 MW beam pulse, the core density and temperature both increased (Fig. 5.3(b)), as did the magnetic axis position and the proximity of the LCFS at the midplane to the outer wall (termed the "gapout" parameter in DIII-D). However, a frequency downshift was still present for ICE during a pulse from a beam with the same geometry but lower power (Fig. 5.3(c)) and the core density and temperature did not change appreciably (Fig. 5.3(d)).

As determined through equilibria constrained by the motional Stark effect (MSE) diagnostic [84], the gapout and magnetic axis shifted at least slightly with each beam pulse. These equilibria were averaged over 4 ms (at 4 ms intervals) on a 129×129 grid. The output magnetic field strengths $B(R)$ were then used for comparison against the highest peaks detected in the autopower measured by an ICE loop on the LFS, as shown in Fig. 5.4(a). The de-

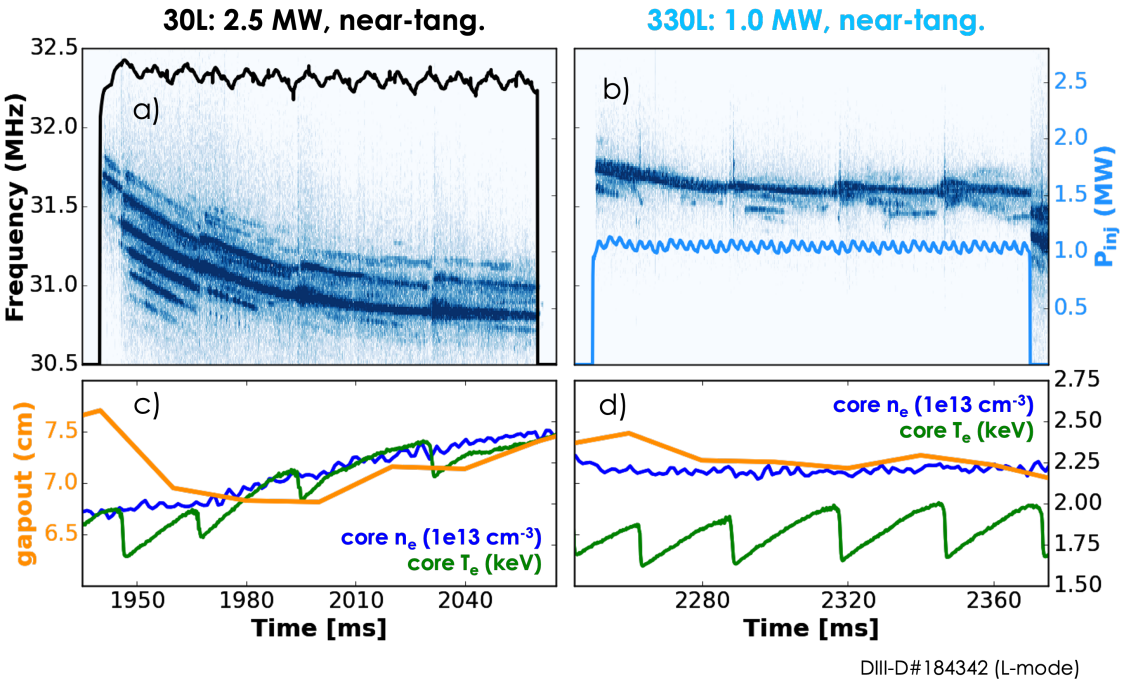

Figure 5.3: ICE autopower spectrum as determined from an HFS loop over the course of a pulse from an on-axis, near-tangential, co-I_P beam, operating at a) 2.5 MW (81 keV) and b) 1.0 MW (55 keV). (c) and (d) Corresponding gapout (orange), core density (blue), and core temperature (green).

tected peaks (centered about the aforementioned equilibria intervals) are shown in yellow, and then the nearest match to these peaks in the equilibria data ($f_{ci}(R) = {}^{q_e B(R)}/_{m_D}$) are represented by magenta dots. f_{ci} corresponding to the magnetic axis is depicted in red, and the LCFS (plus 9 MHz so that the trends are comparable on the same plot) is in lime. ICE frequency tracks best with the magnetic axis position, as the downsweeping over the duration of the beam pulse aligns well with the axis shifting outwards, as opposed to the LCFS peaks that appear somewhat stable throughout this pulse. This dependence on the magnetic axis position was replicated to a lesser extent during pulses from other beams, as the shifts in magnetic axis and gapout were modest or negligible. These beams were either near-perpendicular with respect to the centerpost and/or operating at a much lower power, imparting less pressure and thus likely introducing a lower Grad-Shafranov shift such that the movement of the magnetic axis was comparatively subtle. Similar observations of ICE shifting with the plasma have been made of ch-ICE on NSTX(-U) [60, 61] and core ICE on

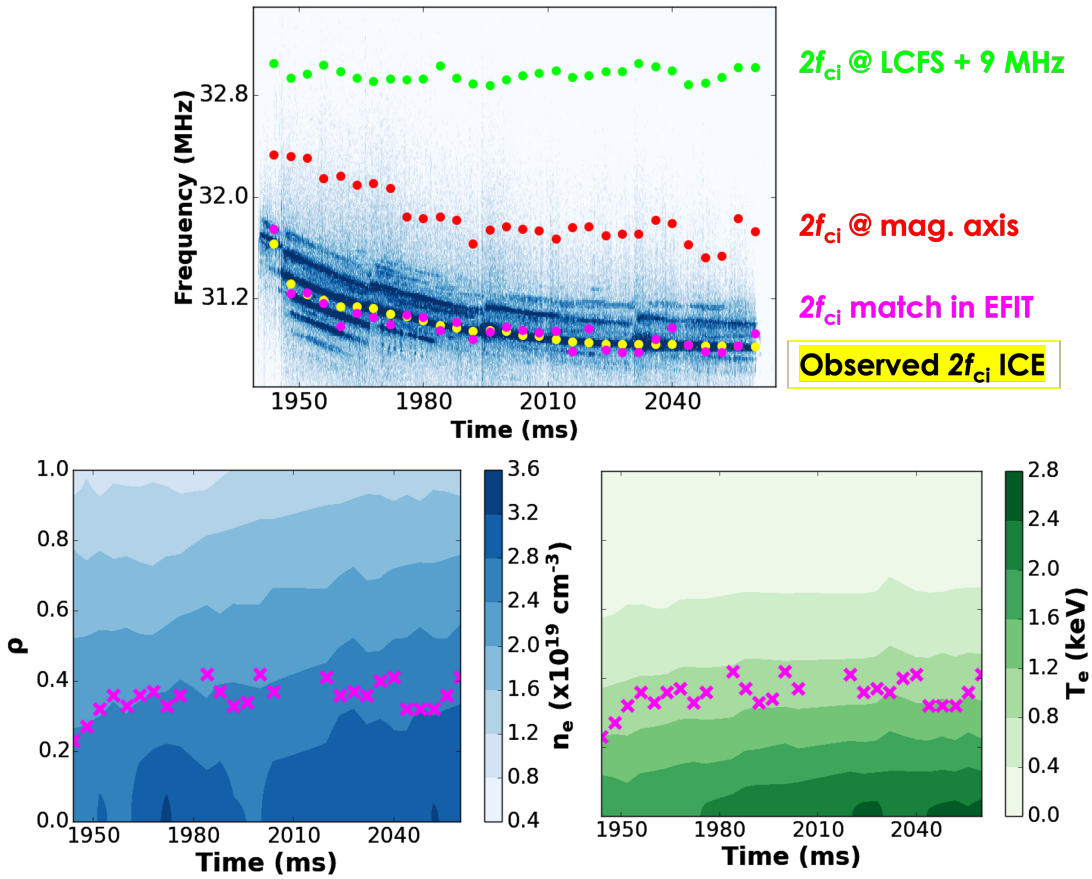

Figure 5.4: a) Maxima in the ICE autopower spectra are determined (yellow dots) and then the closest $2f_{ci}$ matches are found in the equilibria data (magneta). $2f_{ci}$ as calculated at the magnetic axis is pictured in red, and at the LCFS (plus 9 MHz so as to picture them on the same plot) in lime green. b) Density and c) temperature profiles with approximate ICE locations mapped to ρ overlaid in magenta crosses (same points as in magneta in (a)).

AUG [123]. As depicted in Fig. 5.4(b, c), the density and temperature profiles did not possess discernible features that track with the ICE localization. These findings agree with previous observations on DIII-D [165], as well as NSTX(-U) [61], LHD [142], and TUMAN-3M [4], that the observed ICE frequency did not follow changes in density.

Aside from the overall frequency downshifting over the duration of the beam pulse, fine splitting was also observed that was similar to previous studies on DIII-D [165]. In the cases presented in Fig. 5.3, bands spaced roughly 200 kHz apart appeared in the spectra within 10 ms of the beams turning on, with six present in the high-power beam case (Fig. 5.3(a)) and

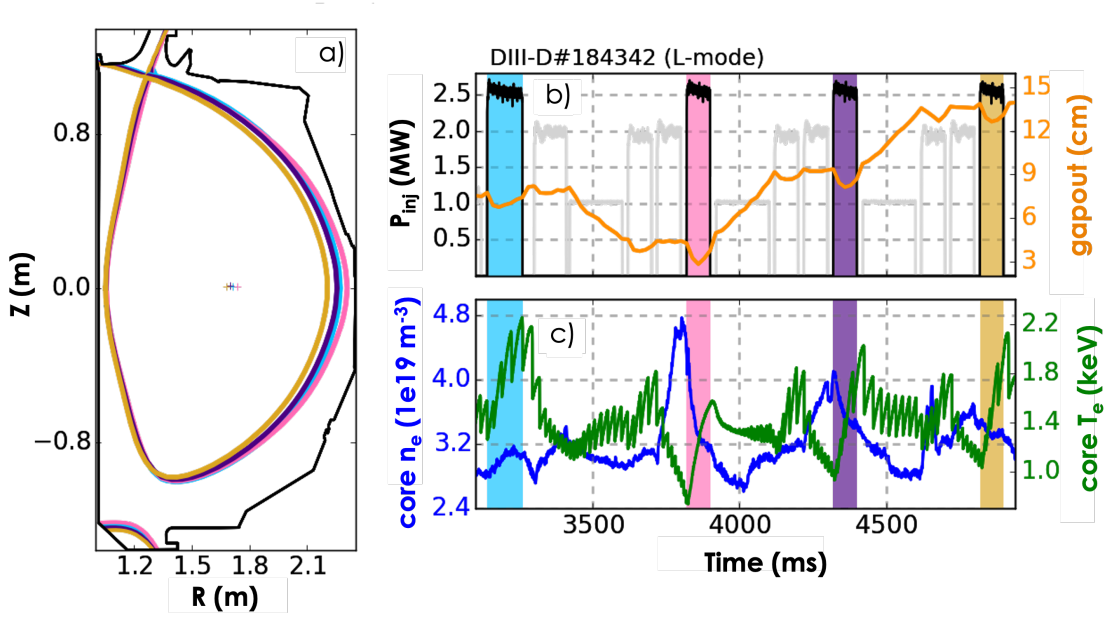

Figure 5.5: (a) Plasma equilibria at different gapout values. (b) Injected power from the 2.5 MW co-I_P neutral beam (black) and gapout parameter (orange) with gapout values of interest marked by colored rectangles.

considerably fewer visible for the low-power beam (Fig. 5.3(c)). In the former high-power case, the lower frequency bands disappeared quickly, with the lowest band stabilizing within roughly 15 ms of its initial excitation. In other pulses, fewer bands were excited and most either lingered or at least reappeared throughout the beam pulse (Fig. 5.3(c)). This fine structure behavior appeared in conjunction with brief periods where ICE was stabilized as sawteeth induced fast ion losses in the core [170], which have previously been observed in core ICE on DIII-D [165].

5.1.2 Scrapeoff region effect on core ICE

In addition to the plasma's slight movements due to beam injection, a dedicated shaping scan was conducted toward the end of the aforementioned $B_T = 2.17$ T L-mode shot to explore how the size of the evanescent layer affects ICE. Fig. 5.5 illustrates this end phase, where the gapout parameter was changed to alter the vacuum region near the outer wall (Fig. 5.5(a),

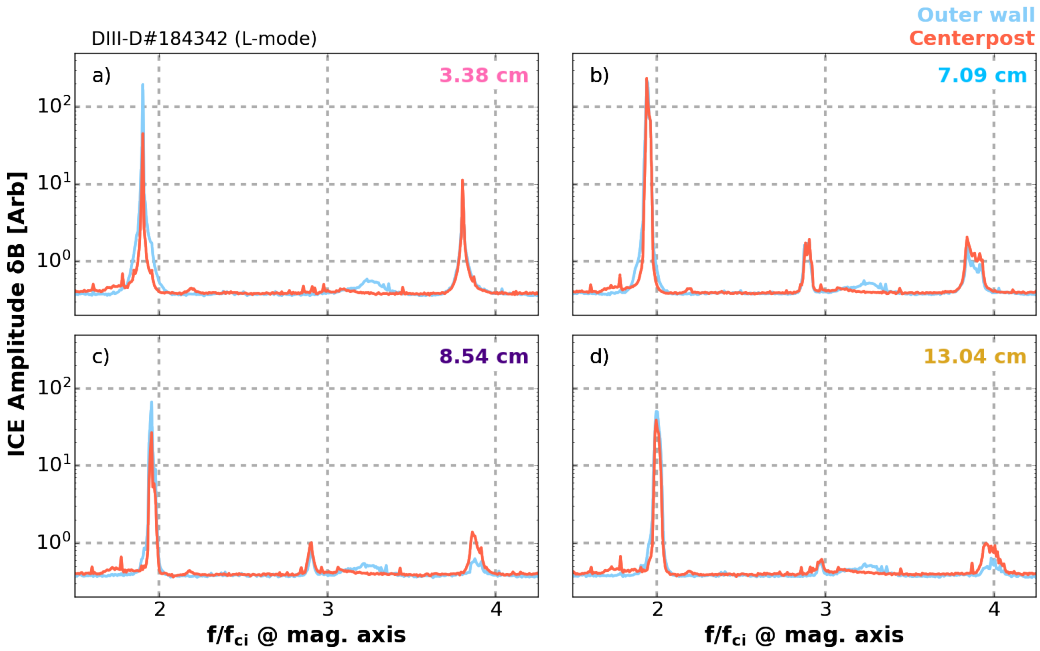

Figure 5.6: Centerpost (red) and outer wall loop (light blue) autopowers time-averaged over 2.5 MW, on-axis beam pulses at gapout values of (a) 3.38, (b) 7.09, (c) 8.54, and (d) 13.04 cm as denoted in Fig. 5.5. f_{ci} is the deuterium ion cyclotron frequency evaluated at the magnetic axis.

(b) in orange) while four different beams were pulsed in succession for roughly 110–170 ms (Fig. 5.5(b), black). The distance between the centerpost and the plasma was held constant; consequently, the magnetic axis position also shifted slightly (approximately half as much as gapout). Time windows during the same 2.5 MW on-axis beam considered in the previous section are highlighted by colored rectangles, and the corresponding equilibria are shown in Fig. 5.5(b). The core electron density and temperature are depicted in Fig. 5.6(c), where density ranged from 2.6–4.8 $\times$ 10^{13} cm^{-3} and temperature from roughly 0.7–2.2 keV.

Autopower spectra as measured by the LFS and HFS loops described in section 3 were compared as a means of investigating whether changes in the evanescent layer impact ICE wave propagation. The resultant harmonics' relative amplitudes were easiest to discern in the time-averaged spectrum data, as is illustrated in Fig. 5.6. In keeping with Chapter 5.1.1, the second harmonic remained dominant, though its emission radius seemed to shift closer to that of the magnetic axis as gapout increases. Before the gapout scan (Fig. 5.6(b)), the

amplitudes measured by both loops were quite similar—however, for subsequent pulses with different average gapout values (markedly, the smallest at 3.38 cm), the outer wall loop detected a stronger $\sim 2f_{ci}$ peak than the centerpost loop. Aside from the period before the scan, the second harmonic generally decreased as gapout was increased. The third harmonic was completely absent for the pulses that happened to have the most extreme average gapout values (Fig. 5.6(a) and (d)). Finally, the fourth harmonic at the lowest gapout value was equally strong in both inboard and outboard measurements (Fig. 5.6(a)). As gapout was increased, the $\sim 4f_{ci}$ peak diminished in amplitude, with the signal as measured by the outer wall loop deteriorating slightly more than its HFS counterpart as gapout increased. As discussed in section 3, the loops used to make these measurements are of different size and thus may have had different sensitivities to the modes—however, if this were the case, one would have expected all peaks to behave similarly, contrary to what is depicted in Fig. 5.6. As both loops observed the harmonics, these modes were likely poloidally extended, as was found previously for core ICE on DIII-D [45].

These peaks exhibited fine-scale frequency splitting, as was particularly evident for the second harmonic (illustrated in Fig. 5.7 during the same time windows highlighted in Fig. 5.5). As in the time-averaged data , the outer wall loop generally observed slightly stronger modes, evinced in the fine structure as additional bands with higher magnitudes (Fig. 5.7(a-d) vs. (e-h)). The ICE with the highest overall amplitude was in the period just before the gapout scan started, at roughly 3140–3260 ms with an average gapout value of roughly 7 cm (Fig. 5.7(b) and (f)). The second harmonic in this case (Fig. 5.7(b)) exhibited a set of multiple strong spectral lines spaced roughly 150–200 kHz apart that persisted through the beam pulse. For later pulses with higher gapout values, a main line accompanied by a similar set of seemingly weaker spectral lines (again, roughly 150–200 kHz apart) were excited (Fig. 5.7(c) and (d)). For all three of these cases, the modes briefly diminished or disappeared entirely as sawteeth expelled fast ions from the core, returning soon after when the driving fast ion population was replenished. However, for the pulse that occurred during the period with the smallest

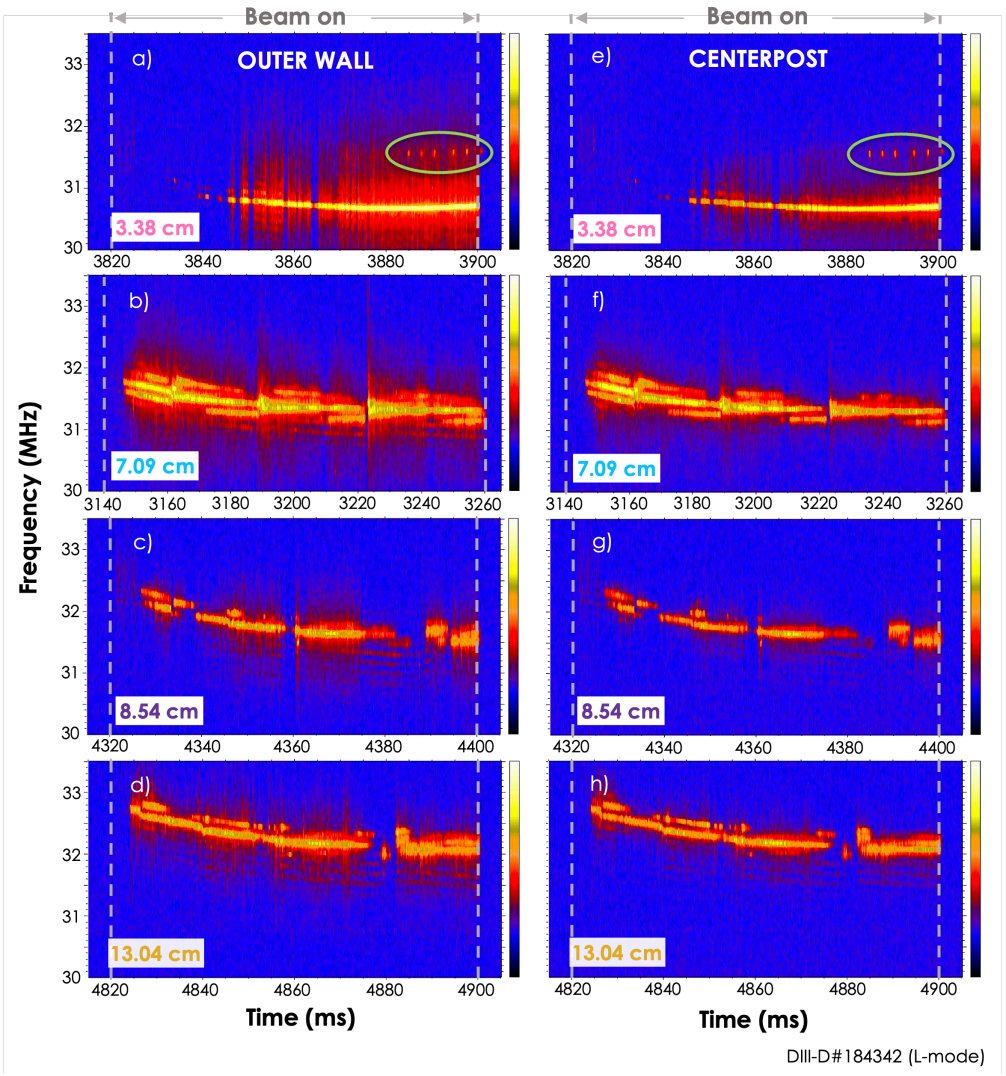

Figure 5.7: Autopower spectra of ICE driven by the 2.5 MW, on-axis, near-tangential beam (all on the same colorscale). Signal from the outer wall probe at gapout values of (a) 3.38 cm, (b) 8.09 cm, (c) 8.34 cm, and (d) 13.04 cm is on the left, and corresponding centerpost signal in (e-h) on the right. The green ovals in (a-e) highlight chirping modes of interest.

gapout value (Fig. 5.7(a)), the delay between beam turn on and mode destabilization was $\gtrsim 3$ times that observed for the other gapout cases. When the mode did eventually appear, it manifested as a solid spectral line. This mode was continuously destabilized over the duration of the beam pulse, as this time period was devoid of sawteeth. Toward the end of this beam pulse, six small blips appeared nearly 900 kHz above the main mode (circled in green in Fig. 5.7(a)).

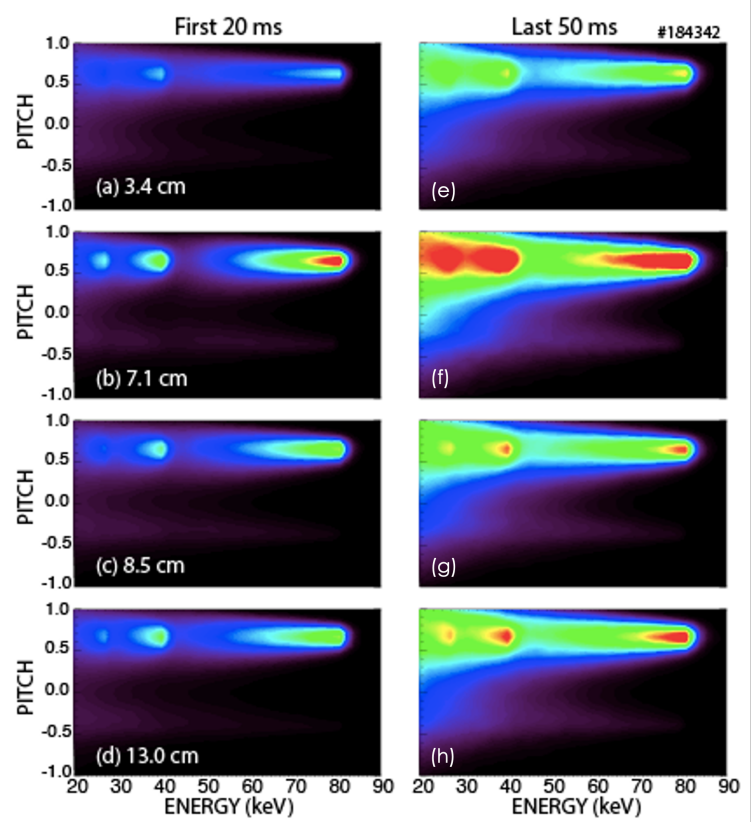

Figure 5.8: The fast ion distribution velocity profile for the beginning 20 ms (a-d) and end 50 ms (e-h) of each beam pulse in Fig. 5.5(c). Here, all distributions are on the same color scale, normalized by the overall maximum beam ion density that is achieved over the pulse from 3820–3900 ms ((b) and (f)). The slowing down times calculated by TRANSP during the last 50 ms of each pulse were (e) 35, (f) 56, (g) 39, and (h) 47 ms.

Previous studies in DIII-D [165, 45] have observed a general dependence of ICE harmonic amplitudes on injected fast ion distribution via various NBI geometries, with [165] observing different fine-scale splitting. For the core ICE cases presented above, the NUBEAM Monte Carlo module [128] within the TRANSP transport code [17] was used to calculate the fast ion distributions at the beginning and end of each beam pulse. The velocity profiles for each beam pulse were averaged over $R \in [165, 195]$ cm and over $|Z| < 15$ cm during the initial 20 ms of the beam pulse (Fig. 5.8(a-d)) and for the end 50 ms (Fig. 5.8(e-h)), with all figures normalized to appear on the same color scale. Though all distributions are peaked at a pitch of $v_\parallel/v \sim 0.7$ with full, half, and third energies of roughly 81, 40.5, and 27 keV, there were significant differences in the fast ion density. The ICE case featuring the most fine-scale

frequency splitting (Fig. 5.7(b)) occurred in conjunction the velocity profile with the largest fast ion density, as depicted by Fig. 5.8(f). In comparison, the number of spectral lines seemed to decrease with the fast ion density until, finally, the case of ICE with the fewest spectral lines (Fig. 5.7(a)) corresponded to the lowest fast ion density of all. Unsurprisingly, the cases with the longest delay between beam turn-on and mode destabilization (Fig. 5.7(a) and (c)) corresponded to the lowest fast ion densities during the first 20 ms. The spatial profiles of the fast ion distributions computed for each beam pulse examined here, generated by summing the fast ion distributions in velocity space, were very similar and as such were less likely to be driving changes in the ICE spectra than the velocity profiles. This core ICE dependence on fast ion density is reminiscent of past observations from the JFT-2M linear device, where core ICE excitation mandated a beam-to-bulk plasma density ratio of $n_b/n_e > 0.1\%$ [177]. (Note, this ratio is unusually high, as ICE is excited in many machines with very small fast ion fractions.)

Varying the bulk plasma density and temperature can effect significant changes in fast ion density, despite unchanging beam energy and geometry (Fig. 5.5(c)). Said fast ion density is roughly proportional to the product of the beam power and slowing down time [80, 156], the latter of which increases with low core n_e and high T_e. In the highest fast ion density case here, the line-integrated core n_e was relatively low in the context of this particular L-mode plasma at $\sim 3.0 \times 10^{19}$ m^{-3}, and core T_e was high at roughly 4 keV (both averaged over the course of the beam pulse) (Fig. 5.5(c)). In comparison, over the course of the beam pulse with the lowest fast ion density, the core n_e decreased from roughly 4.2 to $\sim 3.2 \times 10^{19}$ m^{-3} and the core T_e nearly doubled from roughly 0.8 to 1.6 keV. In the case with the most ICE fine splitting, the slowing down time was 56 ms, whereas the ICE at one main spectral line corresponded to the shortest slowing down time of 35 ms. Possible explanations and comparisons to predictions to frequency splitting are explored further in Chapter 6.2.

Finally, the three long toroidal loops on the outer wall (Fig. 4.1(b) in green) were used to

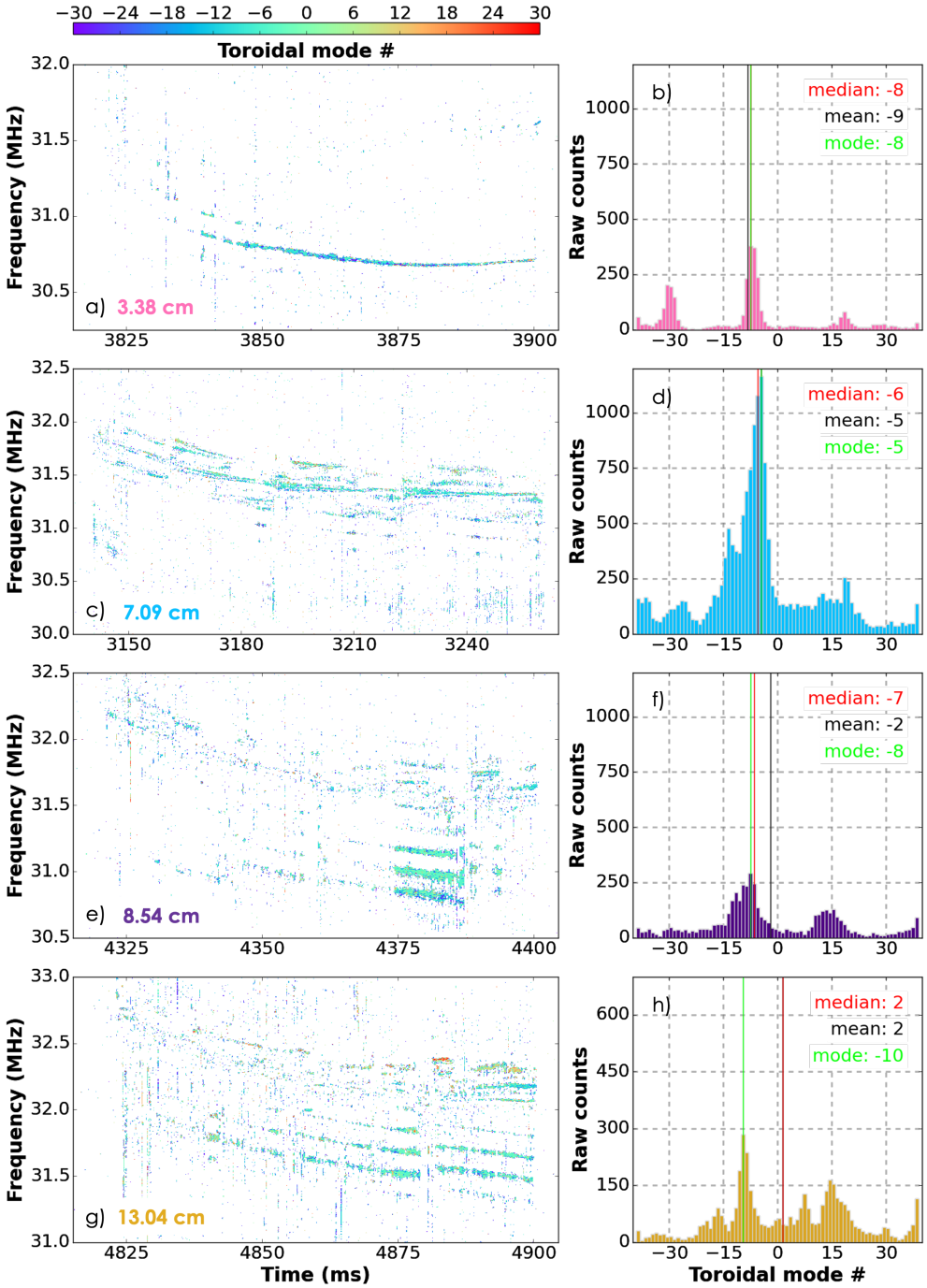

Figure 5.9: The toroidal mode numbers for each frequency and time point during the same beam pulses as discussed in Fig. 5.7 are depicted in (a), (c), (e), and (g). The toroidal mode numbers are then counted and binned, as shown in (b), (d), (f), and (h). The median, mean, and mode values (red, black, and blue) are both delineated over the histograms and printed in the top right corner of each subfigure.

calculate toroidal mode numbers (n) corresponding to the modes shown in Fig. 5.7 [45]. In addition to the autopower spectra typically calculated using signal from each of these loops, the crosspower spectra, including coherence and crossphase, were calculated for each possible loop pairing. The toroidal mode numbers in the time/frequency range of interest were determined using the same technique outlined in Chapter 4.4; for each point that had an acceptably high coherence ($\gtrsim 0.80$), the slope between the crossphase and the physical toroidal displacement between the loop pairs was fit, and the one with the lowest χ^2_{reduced} when compared to theoretical traces of slope $n \in [-39, 39]$ was chosen as the most likely value (Fig. 5.9(e)). In an attempt to mitigate the effects of coherent noise, the toroidal mode numbers considered here were also cross-referenced against autopower values from one of the loops and only those points corresponding to an autopower amplitude greater than 1% of the maximum in the region of interest were kept. The remaining toroidal mode number values were then binned and counted, and the final results are presented in Fig. 5.9(a-d). (Peaks outside of this range that appeared in the histograms are discussed further in Chapter 6.2.) The mode numbers were largely concentrated in the range of roughly $n \in [-20, 20]$, as illustrated by the light blue-teal lines that echo the frequency splitting previously seen in the autopower spectra (Fig. 5.7). The median and mean toroidal mode numbers both slightly increased with gapout, but this trend could not be extricated from the effects of coherent noise, as the overall number of counts that satisfy the above coherence and autopower criteria was relatively low for all cases aside from the ICE case in Fig. 5.9(b). There was no discernible trend in mode number when compared with fast ion density or gapout.

5.2 Edge ICE in H-mode plasmas

The second phase of the experiment explored edge ICE in USN H-mode plasmas whose basic parameters were described in Chapter 3. A gapout scan similar to that in the L-mode

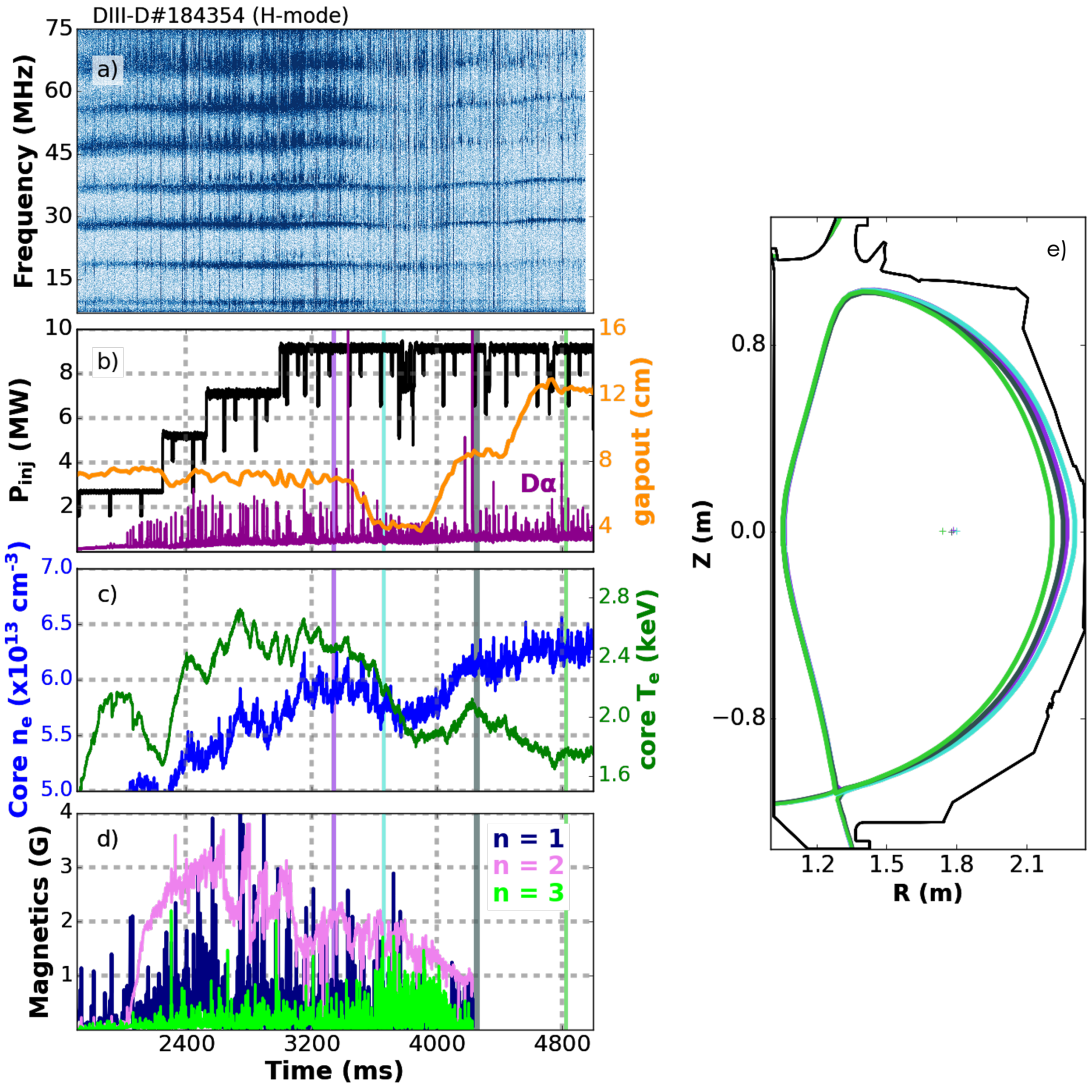

Figure 5.10: (a) ICE autopower spectrum as measured by a toroidal outer wall loop. (b) P_{inj} (black) via neutral beams and gapout (orange), as well as D-α signal in purple to illustrate ELM activity. (c) Core density (blue) and temperature (green) time evoluton. d) Magnetics signals illustrating the n = 1, 2, and 3 signals. (Note, a higher sampling rate was requested, reducing the data acquisition duration such that it did not extend completely through the shot.) (e) Plasma equilibria corresponding to various gapout values highlighted by rectangles in subfigures (b-c).

plasma was conducted in the end phase of three of these shots, one of which is shown in Fig. 5.10 (DIII-D#184354, with $B_T = 1.96$ T and $I_P = 0.95$ MA). Previous assessments [45] determined that these modes were compressionally polarized at the plasma edge and that they were poloidally extended, as the same harmonic peaks were detected by loops on the

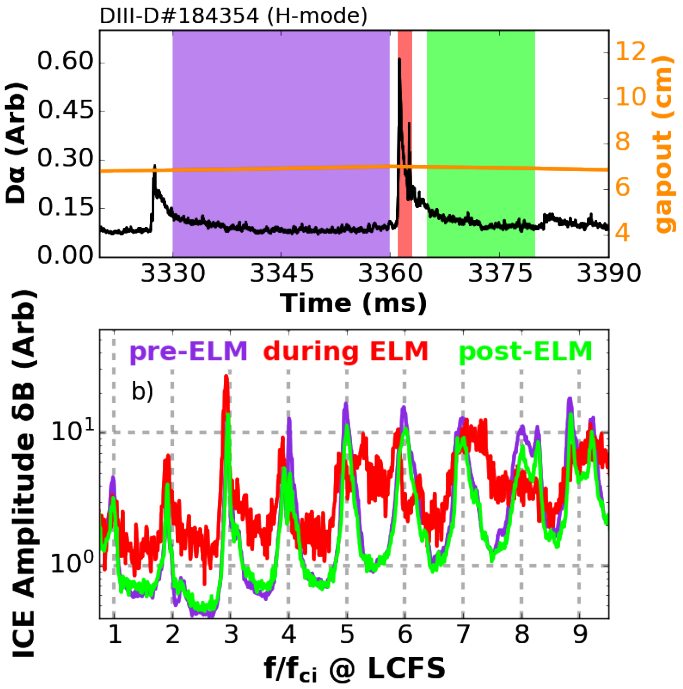

Figure 5.11: (a) ELM during H-mode flattop and (b) time-averages of ICE signal before (violet), during (red), and immediately after (green) an ELM. Here, the violet denotes an example of the time windows used for analysis in this paper.

HFS and LFS sides of the machine. These findings were corroborated by the high-frequency DBS system, which observed density fluctuations corresponding to harmonics of f_{ci} at the LCFS over $\gtrsim 1/6$ of the minor radius [41].

The frequency of the peaks generally changed as gapout varies (Fig. 5.10(b), in orange), similar to core ICE behavior in L-mode (Fig. 5.6). The gapout scan started at roughly 3500 ms, where the average gapout value was decreased significantly from its original value of ∼6 cm to 4 cm, and then back up to roughly 8 and then 12 cm. The line-averaged core density was kept fairly constant throughout at ∼5.75–6.25 $\times 10^{13}$ cm^{-3}; however, the core temperature decreased throughout the scan from $T_e \sim 2.5$ to 1.8 keV (Fig. 5.10(c) in green and blue, respectively).

As these were standard H-mode plasmas, ELMs were present (Fig.5.10(b) in purple). Here, ELMs did not suppress edge ICE as has been observed in some cases [29, 37, 41], but instead

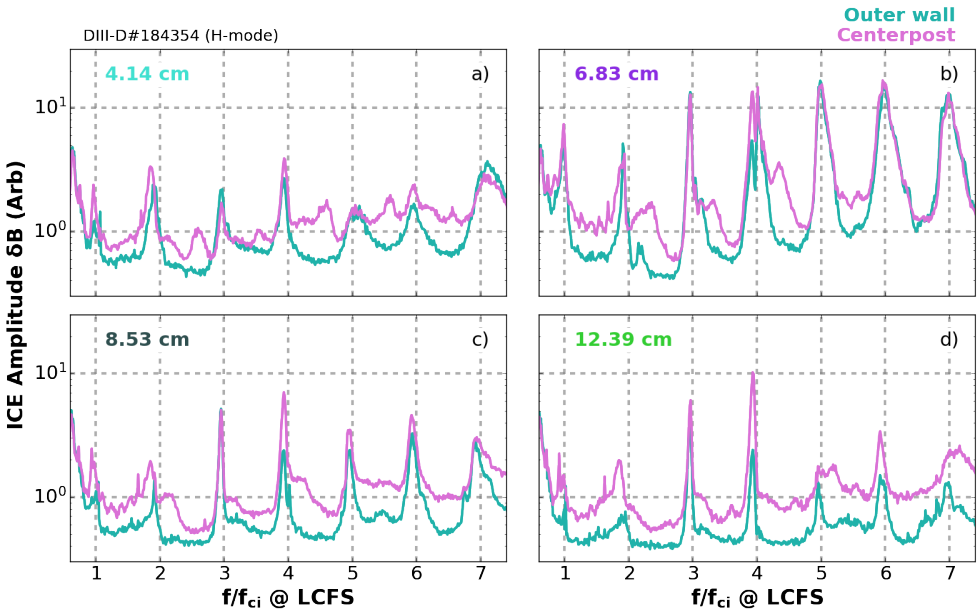

Figure 5.12: Autopower spectra from centerpost and outer wall loops time-averaged during periods with average gapout values of (a) 5.75, (b) 6.83, (c) 8.53, and (d) 12.39 cm. The purple rectangle highlights the time period before the gapout scan was conducted, corresponding to Fig. 5.10.

introduced a broadband RF signal in addition to the base edge ICE peaks, as seen previously in KSTAR [162]) and illustrated here in Fig. 5.11. To avoid this feature, all analysis for this work was undertaken in periods between ELMs, which here constituted time intervals of roughly 10–30 ms (purple and green in Fig. 5.11(a)). As higher harmonics may be obfuscated by aliased harmonics ($f > 100$ MHz), only harmonics 1–7f_{ci} were considered.

The effects of altering gapout on ICE amplitude were, again, most visible in the time-averaged data (Fig. 5.12). Beginning with the response of the lower harmonics ($f/f_{ci} < 5$), the second harmonic generally featured the largest difference between the inboard and outboard loops; this difference increased with gapout, from roughly 470 kHz to nearly 900 kHz at the largest average gapout value of 12.39 cm. Note, differences in frequency for the same harmonic peak were observed here for edge ICE but were not seen for any gapout value in the core ICE studies. The gapout scan appeared to disturb ICE such that different features were observed throughout the gapout scan from those in the "original" plasma. Once

the plasma was perturbed from this initial state (Fig. 5.12(b)), signal from the centerpost was no longer upshifted, but instead the outer wall loop routinely saw the second harmonic peak at slightly higher frequencies. This was illustrated in Fig. 5.13(a), where this trend was observed in two other H-mode shots with gapout scans. Both of these shots were well-matched in bulk plasma density and temperature, despite one of the shots having a higher magnetic field strength of $B_T = 1.96$ T. The fourth harmonic did not exhibit a large frequency difference between inboard and outboard peaks; however, there was an amplitude difference that increased with gapout. Again, this was replicated in two other H-mode shots (Fig. 5.13(b)), where the log of the ratio of the fourth harmonic peak amplitudes as measured by the LFS and HFS loops generally increased with gapout, aside from points before the gapout scan (marked by orange oval). Finally, the third harmonic appeared very similar in amplitude and frequency in the inboard and outboard data for most gapout values, save for the time window with the lowest average gapout value, where the peak measured by the outer wall loop had a slightly higher amplitude.

In stark contrast, the higher harmonics did not seem to follow any sort of uniform change with gapout. Again, ICE was seemingly disturbed by the gapout scan such that the spectrum behaved differently in time periods beyond that depicted in Fig. 5.12(b). Peaks at $f \simeq 5$, 6, and $7f_{ci}$ that were observed at nearly equal, relatively high amplitudes by both the inboard and outboard loops before the gapout scan were of much lower amplitudes in subsequent time windows, regardless of whether the average gapout value was larger (Fig. 5.12(c) and (d)) or smaller (Fig. 5.12(a)) than the initial average value of 6.83 cm. Furthermore, where there was generally little difference in amplitude between the two loops initially, the centerpost loop was more sensitive to these harmonics in these later times. These higher harmonic trends held for the other two shots with gapout scans.

The velocity distribution of the fast ion function for each time of interest in DIII-D#184354 is illustrated in Fig. 5.14, where all averages were taken during 23 ms intervals centered in

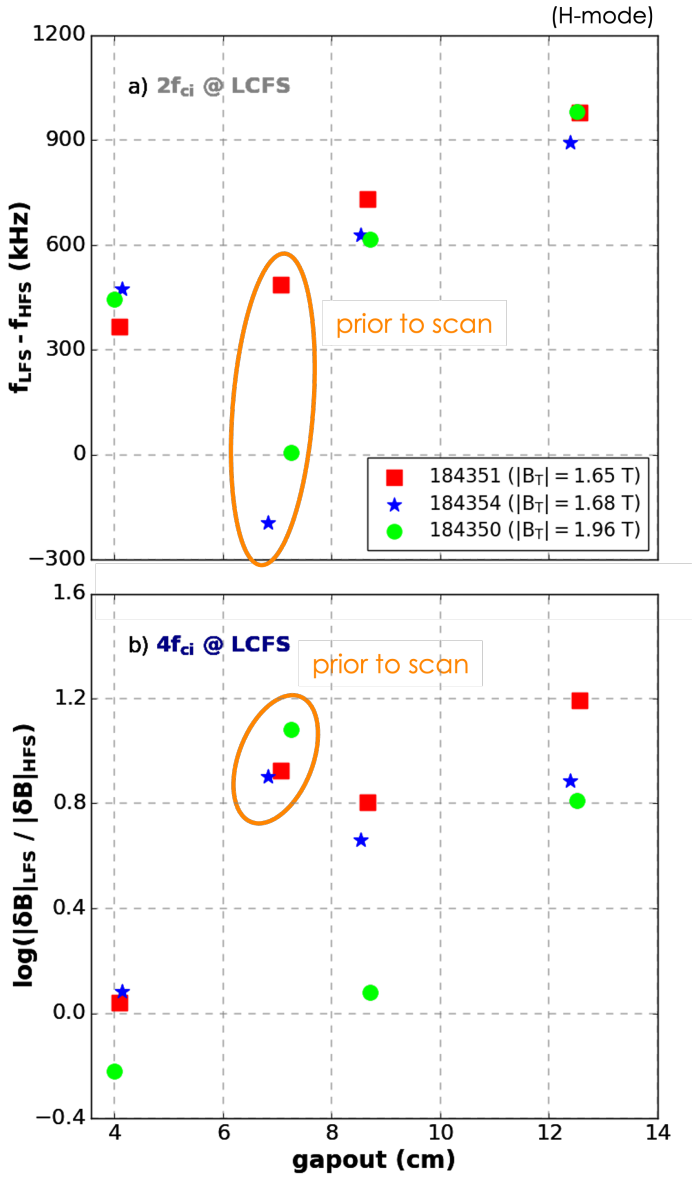

Figure 5.13: (a) Difference between LFS frequency (f_{LFS}) and centerpost frequency (f_{HFS}) for the second harmonic vs. gapout for three H-mode shots. (b) Difference in the log of LFS and HFS amplitude for the fourth harmonic.

the middle of the ELM-free time periods denoted in Fig. 5.10(b-c). In all cases, the spatial average was over the two $[R, z]$ points that are closest to the LCFS at the outer midplane. The velocity profiles here were peaked at a pitch of $v_\parallel/v = 0.5$, with presumably some of the higher-pitch particles ionizing in the edge. Contrary to the velocity profiles presented in section 5.1.2, all edge ICE velocity profiles were exceedingly similar, indicating perhaps that the aforementioned frequency shifts are predominantly due to some other effect. Fig. 5.14(e-

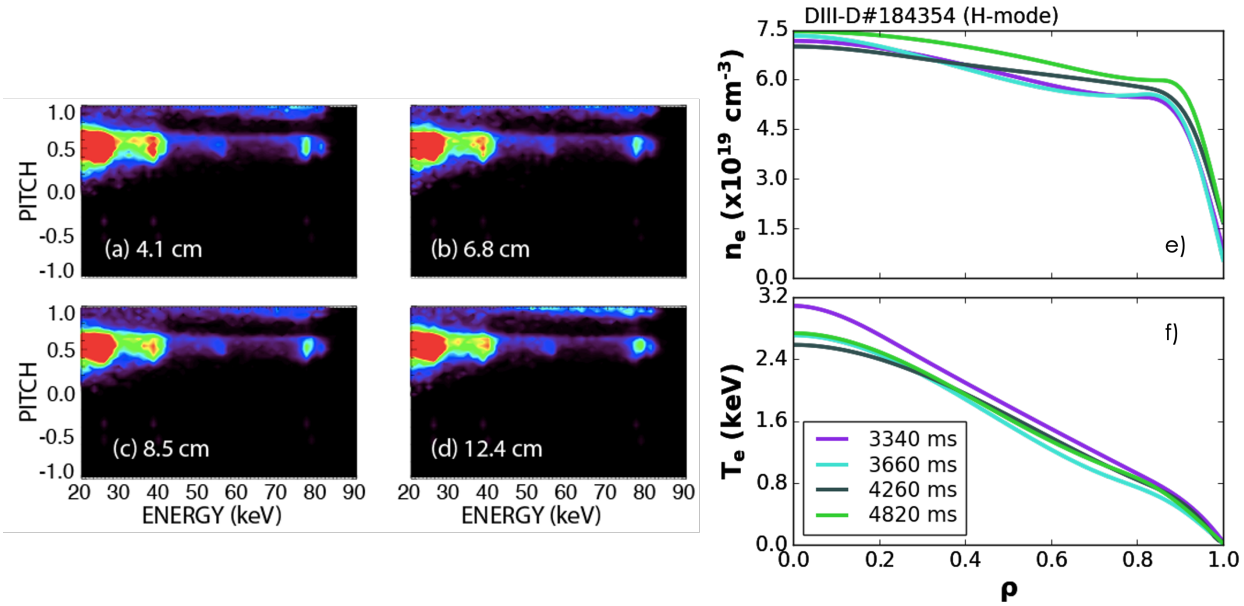

Figure 5.14: The velocity profile of the fast ion distribution for each highlighted time period depicted in Fig. 5.10(b and c). Bulk plasma density (e) and temperature profiles (f) mapped to the normalized flux surface ρ.

f) depicted bulk plasma profiles of n_e and T_e, where the former was determined using CO2 interferometer [169], Thomson scattering [22], and reflectometer [181] data; and the latter from Thomson scattering and electron cyclotron emission [5] diagnostics. Time-averaging windows of 20 ms were selected, centered roughly in the ELM-free time windows highlighted in Fig. 5.10(b-d). Again, the equilibria used to determine ρ were constrained by the MSE diagnostic [84], though in this case the temporal resolution was not quite as fine as in Chapter 5.1.1, instead having been averaged over time intervals of 20 ms. There appeared to be slight changes in the density (Fig. 5.14(e)) at the edge of the plasma ($\rho \gtrsim 0.95$) between the different time periods, but no trends that corresponded to the drastic changes in ICE signal from before (purple line) to after the gapout scan was initiated. T_e at the edge was extremely similar for all time periods.

5.3 Observed vs. predicted frequency splitting

Multiple mechanisms have been put forth to predict ICE fine splitting, both in the local MCI and global eigenmode approaches. One such prediction in the former category, devised by Fülöp et al. [64, 65], stems from the addition of toroidal effects to the local resonance condition and predicts the following doublet splitting:

$$\delta\omega/\omega \approx (\rho_L/R)(v_{\text{beam}}/v_{\text{Alfvén}})(1+p_r^2) \tag{5.1}$$

where ρ_L is the fast ion Larmor radius, R the major radius of the machine, v_{beam} the beam ion velocity, $v_{\text{Alfvén}}$ the Alfvén velocity, and p_r the pitch of the resonant fast ions. For the core ICE cases presented here, $\rho_L/R \sim 0.07$, $v_{\text{beam}}/v_{\text{Alfvén}} \sim 0.5$, and $p_r \sim 0.7$, giving rise to an estimated splitting of $\delta\omega/\omega \sim 5\%$. This is much larger than the $\delta\omega/\omega = 0.9\%$ observed for the spectral lines in most pulses, but aligns closely with the spacing of 900 MHz ($\delta\omega/\omega = 5\%$) between the chirping modes and the main spectral line in Fig. 5.7(a, e). This model similarly overestimated $\delta f/f$ for NSTX(-U), where splitting of $\delta\omega/\omega$ ∼15–17% was predicted, roughly six times the observed 2.7% [61].

This description is further challenged by comparisons of this second harmonic core ICE in a $B_T = 2.17$ T with both fourth harmonic ICE from the same beam pulse, and to a pulse from the same beam into a similar plasma with $B_T = 1.25$ T. In the case of the fourth harmonic, this expression would predict δf to follow with frequency—i.e., that δf should increase by a factor of two for $4f_{ci}$. However, as depicted in Fig. 5.15, very similar splitting on the order of 150 kHz was observed for the fourth harmonic, nearly identical to that observed for the second harmonic. In Eq. 5.1, this splitting would also be expected to increase with beam velocity and decrease proportionally to $1/B^2$, but this was not observed in comparing $2f_{ci}$ in plasmas with different magnetic field strengths. The same on-axis, near-tangential, co-I_P, 2.5 MW beam was injected into similar plasmas with $B_T = 2.17$ and 1.25 T, as seen in

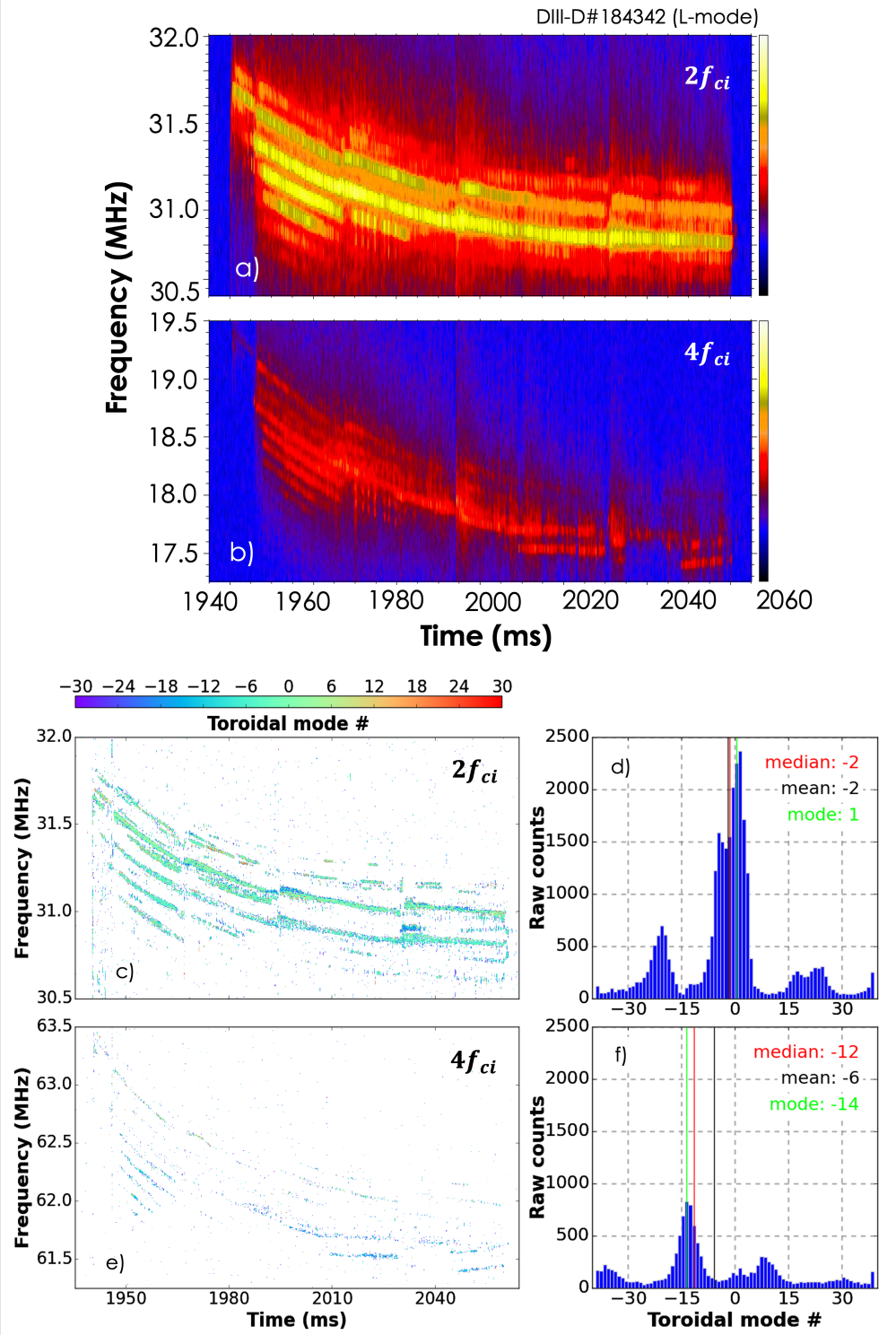

Figure 5.15: Toroidal mode numbers are calculated for the second harmonic ICE (a) during a pulse before the gapout scan, as depicted in Fig. 5.3. The toroidal mode numbers are counted in (b). The same processes are applied to the fourth harmonic (b) and (d). The median, mean, and mode values (red, black, and blue) for the counts are both delineated over the histograms and printed in the top right corner of (b) and (d).

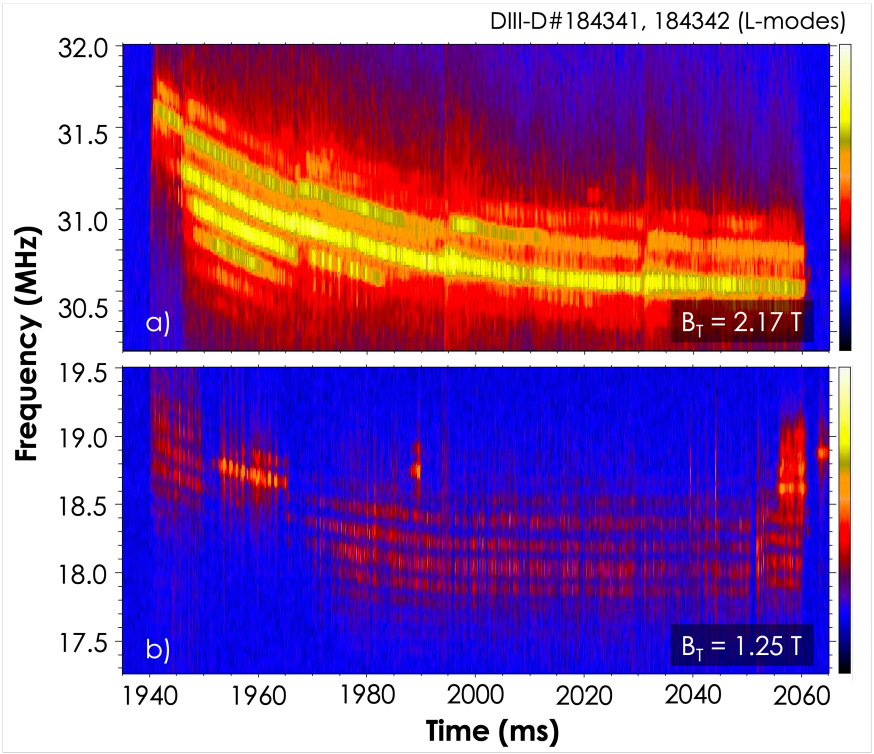

Figure 5.16: Second harmonic core ICE excited by the same on-axis, near-tangential, co-I_P 2.5 MW beam in a) $B_T = 2.17$ T and b) 1.25 T L-mode plasmas.

Fig. 5.16. The same splitting of ~ 150 kHz was observed for both $f/f_{ci} = 2$ modes, where the δf in the case of the $B_T = 1.25$ T should have been roughly three times that observed at 2.17 T, judging by the ratio of $(1/1.25^2)/(1/2.17^2)$. Over the duration of these beam pulses, the average densities were slightly different ($n_e \sim 2.17$ and 1.82×10^{13} cm^{-3}) and the average core T_e for both was roughly 2.11 keV.

For edge ICE, experimental values were roughly $\rho_L = 0.20$ m, $R = 1.79$ m, $v_{\text{beam}} = 2.79 \times 10^6$ m/s, $v_{\text{Alfvén}} = 3.27 \times 10^6$ m/s, and $p_r = 0.5$, resulting in an estimated splitting of $\delta\omega/\omega \sim 11\%$ (roughly 1.3 MHz for $f_{ci} = 12.3$ MHz). Splitting of this magnitude was found in some instances of edge ICE on DIII-D, e.g., for the fourth harmonic in Fig. 5.12(b) where two peaks were present and separated by roughly 2 MHz. This doublet peak was also observed in the time-averaged data before the gapout scan was initiated in the other two H-mode shots. However, this was not ubiquitously observed, as was evident through the lack of

doublet splitting in the other time-averaged spectra for the same plasma (Fig. 5.12(a, c, d)). Multiple peaks were observed for harmonics $f/f_{ci} > 7$ but their spacing often exceeded 3 MHz, ~ 2.5 times larger than anticipated. Recent work [32] has revisited splitting via MCI, particularly in the event that there are large $v_\parallel$ (assuming a uniform plasma), leading to a resonant Doppler shift comparable to the cyclotron frequency. This in turn can result in large splitting (i.e., large fractions of f_{ci}) and make determining the ICE emission radius difficult.

In the global eigenmode picture, an energy shift between co- and counter-propagating modes is expected due to the toroidal current and associated poloidal magnetic field present in a tokamak [37, 2]. Here, a homogeneous cylindrical case is assumed, and the predicted splitting in terms of the parallel index of refraction ($N_\parallel = {}^{k_\parallel c}/_{\omega}$) is given by:

$$\Delta N_\parallel \sim (c/\omega r)(B_\theta/B) \tag{5.2}$$

where r is the radial location of the mode (note, this derivation assumed a circular cross-section and r here is the distance from the core of the plasma to the mode), B_θ is the poloidal magnetic field, and B the total magnetic field. In the case of core ICE, this expression becomes impractical as $r \to 0$ in the denominator. However, for $4f_{ci}$ edge ICE, $r \sim 0.52$ m, $\omega/2\pi = 38.09$ MHz, $B_\theta \sim 0.17$ T, and $B \sim 1.50$ T gives rise to $\Delta N_\parallel \sim 10.79$, or $\Delta k_\parallel \sim 0.11$. In principle, one could use measurements of n to get estimates of $k_\parallel$, which can roughly be approximated at the edge by scaling $k_\phi = {}^{n}/_{R}$ by R. However, toroidal mode numbers have not yet been determined for edge ICE, as these modes tend to be much less coherent than their core counterparts. Future work may address this issue.

Moreover, some of the peaks in the spectrum appeared and vanished at different times during a beam pulse, as seen in Fig. 5.7. Generally, if the different peaks in the fine splitting corresponded to distinct modes (for instance, slightly different frequencies if they had slightly

different $k_\parallel$ or $k_\perp$), then they might have had different growth rates. Assuming that the amplitude of each mode depends on the growth rate, the more unstable modes were the ones with larger measured amplitudes. Some of the drive came from the bump on tail in the fast ion distribution that goes away on the slowing down timescale. It could be that this extra bit of drive was needed to make the "less unstable" modes have positive growth rates overall, such that when this was gone, the remaining drive was not large enough to overcome the damping. But for the more unstable modes, like the ones that persisted for the entire duration of the beam pulse, they might have had large enough growth rates from other gradients in the fast ion distribution to keep them net unstable the entire time. This is supported by recent AUG [109] observations, where the ICE destabilization was very sensitive to the slowing down and pitch angle diffusion of the fast ion distribution.

Sub-cyclotron modes in DIII-D also showed frequency splitting, though typically much finer than presented for ICE here (δf $\sim$20 kHz as reported in [79], which were subsequently determined to be GAEs [161] vs. $\delta f \geq 100$ kHz for ICE). In [10], it was argued that this fine splitting could not be explained by incremental changes in mode numbers in the ideal MHD shear Alfvén wave dispersion. Instead, these small frequency differences could be generated by non-ideal corrections to the shear Alfvén wave dispersion (namely, coupling to compressional waves and finite ω/ω_{ci} corrections from the Hall term), which could lead to the correct order of magnitude frequency difference for different radial mode numbers. This points to the possibility that the observed ICE frequency splitting could also be attributable to non-ideal corrections to the dispersion relation, which is left as a possibility to explore in future work. In general, understanding the observed frequency splitting is desirable since it provides additional experimental features for verification of future ICE simulations in toroidal geometry.

Chapter 6

Summary and discussion

6.1 Summary

The ion cyclotron emission diagnostic on the DIII-D tokamak has been upgraded to comprise seven single-turn magnetic pickup loops that (nominally) measure magnetic field fluctuations at frequencies in the ion cyclotron range (1–100 MHz). A new horizontal loop was installed on the LFS of the machine, and it can be used in conjunction with its neighboring small toroidal loop to estimate mode polarization at the plasma edge through the ratio of toroidal to poloidal fluctuation amplitude $\delta B_{tor}/\delta B_{pol}$. Two existing long toroidal loops on the LFS were joined by a third, enabling measurements of toroidal mode number n. Finally, two new HFS loops were installed and their signals can be compared to those of their LFS counterparts to investigate, among other things, whether observed modes are poloidally extended. A new high-frequency configuration enabling measurements of frequencies into the lower hybrid range ($\sim$ 500 MHz) has also been tested and used for initial helicon conditioning experiments.

A dedicated 2021 experiment in DIII-D made use of these diagnostic upgrades, characterizing mode structure and exploring mode phenomenology for both ICE and sub-cyclotron modes

in L- and H-mode plasmas. Core ICE in L-mode plasmas was found to have a ratio of $\delta B_{tor}/\delta B_{pol} > 2$ for harmonics of appreciable amplitude, indicating compressional polarization at the edge. Sub-cyclotron modes in L-mode plasmas and edge ICE in H-mode plasmas were similarly compressionally polarized, with ratios of $\delta B_{tor}/\delta B_{pol} \gtrsim 2$ and ~ 3, respectively. Further, the sub-cyclotron measurements presented here are in agreement with simulations made for comparable plasmas on DIII-D [10, 11, 161]. Toroidal mode number estimates were made for sub-cyclotron modes and core ICE, with the former serving as a benchmark for the calculation method. In this suspected GAE case, the mode numbers remained in the range $n \in [-25, -20]$, close to heuristic estimates of $n \in [-20, -13]$ and results of roughly $n = -23$ from DIII-D-relevant simulation work [10, 11, 161]. Toroidal mode numbers in the range $n \in [-10, 5]$ were calculated for core ICE, with both positive and negative n indicating a mix of co- and counter-propagating modes. These measurements were similar to observations made on NSTX(-U) [60] and JT-60U [85]. Comparing signals from the centerpost and outer wall loops indicated that ICE is poloidally extended.

Core ICE was found to be highly dependent on plasma shape. Second harmonic ICE was observed to track movements in the magnetic axis very closely, as even small shifts due to single beam injection appear in the ICE spectra as downshifts of up to roughly 500 kHz. The distance between the LCFS and the outer wall was altered, and ICE harmonic amplitudes generally appeared to diminish with increasing gapout. The second harmonic exhibited the largest difference in amplitudes measured by the LFS and HFS loops, with the stronger modes observed by the outer wall loop at smaller gapout values. Fine-scale frequency splitting on the order of ~ 150 kHz was seen particularly for second harmonic core ICE, with more spectral bands corresponding to higher fast ion densities. There was no observable splitting dependence on gapout. Toroidal mode numbers calculated for these harmonics fell largely within the range of $n \in [-20, 20]$ and there was no direct dependence on either fast ion density or gapout.

Similar scans of gapout were conducted during the end phase of H-mode plasmas to assess edge ICE dependence on the vacuum region. In these cases, differences in both frequency and amplitude were observed in the time-averaged spectra as measured by the LFS and HFS loops for specific harmonics. Contrary to core ICE, there is little difference in the fast ion distribution for the various time windows of interest in the edge region, and the difference in the second harmonic peaks measured by the LFS and HFS loops linearly increases with gapout. A similar, roughly exponential dependence on gapout is observed for the ratio between LFS and HFS-measured fourth harmonic amplitude. Though it seems more likely that changes in gapout may be contributing to these spectral variations, it is noted that the absence of a general decrease in higher harmonics complicates this picture. There is minimal doublet splitting in these edge ICE cases, but when observed it roughly agrees with predicted values stemming from drift effects.

The detailed mode structure measurements presented here, coupled with fast ion distribution information, can be used to test and validate theoretical models en route to developing a more complete physical understanding of ICE so that it can be leveraged as a passive fast ion diagnostic in future burning plasmas.

Further investigation of mode fine splitting and toroidal mode number dependence on evanescent layer and fast ion distribution (in conjunction with measurements from the high-frequency DBS system where possible) may help bridge the gap between theory and experiment.

6.2 Discussion

In calculating toroidal mode numbers, modes of lower autopower amplitudes tend to be somewhat bimodal in terms of n counts, as seen in figure 5.9. These unexpected peaks

are likely due coherent noise and/or wrongful selection of the toroidal mode number based on χ^2_{reduced} values. In the case of the former, despite a filter based on autopower spectra, there can still be points in the toroidal mode number spectra that do not align with the spectral bands (as depicted in figure 5.7), especially for modes of low amplitude. Increasing the autopower spectra threshold to suppress too many of these points, however, leads to depleted resolution in the area of interest. The other contributor to unexpected peaks in n counts may be points whose lowest χ^2_{reduced} value corresponds to an aliased value of n. The nominal resolvable range of mode numbers as determined by the closest in-vessel pair is $|n| < 13$ [45] (Chapter 4.4), and while the third loop enables better resolution outside of this range, it cannot entirely remove all aliased points. This latter issue may be improved through installing additional toroidal in-vessel loops to increase the number of pairs in the toroidal mode number calculation.

It is also worth noting that the mode numbers presented in figure 5.9 are generally lower than those calculated for a beam pulse earlier in the same shot (described in depth in [45] and reproduced for discussion in Chapter 5.3), which fell largely in the range $n \in [-10, 5]$. Understanding the nature of this change is largely left for future work, but it should be noted that the average plasma density was somewhat lower (2.17×10^{13} cm^{-3}) later compared to a pulse with the same gapout at 3135 ms ($n_e \sim 2.98 \times 10^{13}$ cm^{-3}). The average core temperature slightly decreased, from roughly 2.11 to 1.75 keV.

6.3 Outlook and future work

ICE measurements on reactor-relevant devices may come from multiple diagnostics, including RF probes akin to the magnetic pick up loops detailed in this work. Alternative methods that make use of systems already planned for installation on ITER include microwave reflectometry [116, 171] and ICRH antenna arc detection systems [54, 88, 115]. While possibly

ill-suited to reactor conditions due to optical components, DBS may be used in present devices to augment δB measurements and help to expand the ICE physics basis ahead of ICE diagnostic implementation on a reactor.

Possible developments to the diagnostic system on DIII-D are detailed in Chapter 6.3.1, and potential lines of inquiry are proposed in Chapter 6.3.2.

6.3.1 Expansion of the DIII-D ICE diagnostic

Some diagnostic improvements can be made without purchasing additional components. The system should be calibrated; while the diagnostic currently is sufficient for relative determinations and proof-of-concept explorations, measurements of mode amplitude will be helpful for constraining simulations in the future. Another investigation may be comparison of toroidal mode numbers as calculated by the retired ICRF straps against those determined via the ICE diagnostic.

Supplementary loops would greatly aid in resolving existing measurements and expanding diagnostic capabilities. Additional long toroidal loops on the LFS would mean more pairs and thus additional data points to better resolve toroidal mode number calculations—particularly for higher harmonic core ICE or edge ICE, where currently toroidal mode calculations are difficult as the signal can be of relatively low amplitude and/or somewhat lost in coherent background noise. Horizontal loops on the LFS could aid in poloidal resolution, though determination of poloidal mode number is less meaningful for DIII-D cases than it may have been for devices with a circular cross-section (e.g., TFTR), as poloidal symmetry is not conserved. Finally, either vertical or horizontal loops on the HFS would be welcome. The former would enable toroidal mode number measurements, which could be compared to those determined on the LFS, addressing whether toroidal mode number is indeed conserved. The latter may be useful for comparisons against edge polarization measurements and estimations

of k via high-frequency DBS.

Another idea may be to try increasing the distance between the diagnostic probes and the plasma. Removing the loops from highly-radiated regions would extend diagnostic life, and it was shown in Chapter 5 that ICE signal—in the case of edge ICE—is not prohibitively sensitive to the vacuum region width. One could imagine placing probes far back in ports (more likely of a variety akin to those used in [142, 162], as opposed to the current ICE loops that involve tile faces) and comparing signal to that of the existing tile loops. A more unconventional test or possibly outside the machine. It is possible that the conducting vessel shields signal at these frequencies, but it is worth testing nonetheless.

It must also be noted that the utility of the ICE diagnostic extends past ICE and sub-cyclotron studies. The work to expand the diagnostic to higher frequency ranges (Chapter 3.4 and Appendix C) could be improved through acquiring additional broadband capacitive DC blocks, which could ultimately replace the limited ferrite-core isolation transformers currently in use. Additional function generator(s) would also be necessary to mix down signal, or a higher frequency digitizer would be required[1]. While it is possible that lower-loss cables could be implemented and the in-vessel loops slightly altered (e.g., the length of exposed inner conductor between the loop front and mounting bracket changed), cable skin depth and/or the in-vessel loop reactance may impose an unavoidable upper frequency limit (at least $\lesssim$ 1 GHz) on this system.

6.3.2 Lines of inquiry

Possible lines of inquiry for future core ICE investigations include more dedicatedly probing fast ion density and determining whether there is a threshold for destabilizing ICE. Con-

[1]Note, implementing a higher-frequency digitizer like those used on LHD [141] and KSTAR [162] would likely limit the data acquisition window to be quite a bit shorter than the duration of the plasma. While far from prohibitive, this would require careful consideration of a trigger system.

comitantly, these investigations would provide additional fine-scale spectral splitting data. Although initiated in this work, further shaping and localization studies would be useful and will benefit from collaboration with the high-frequency DBS diagnostic. The L-mode studies presented in Chapter 5 rely on a single shot and thus are insufficient to extrapolate general trends—even adding additional shots and/or beam pulses of the same ilk to this dataset may help to elucidate ICE dependence on shaping and frequency splitting.

The pure deuterium studies presented here could be extended into mixed species plasmas, beginning with an existing mixed-species dataset comprising $\gtrsim 200$ shots with cycled beams that were part of 2018 and 2021 Frontier Science experiments. These studies may be particularly useful in determining the impact of beam ions vs. fusion products.

Edge ICE studies are in need of dire attention, particularly in calculating mode numbers. Potential phenomenological studies could be undertaken as well, which may begin with characterizing edge ICE in various scenarios. This naturally would call into question how ICE depends on pedestal characteristics (e.g., height, width, and/or dependence on density and temperature gradients), as well as how ICE is impacted by ELMs, or even serve as a precursor as in the case of EAST and KSTAR. As with core ICE, edge ICE should be studied in mixed species plasmas, particularly the emission region, as ICE was seen to change localization slightly when excited by beam ions vs. fusion products in D-T plasmas [25].

Another simple study would be to use the HICE configuration to explore higher-frequency ranges; it is unclear exactly how many edge ICE harmonics are excited, as the default ICE system with the standard low-pass filters and Ikezi-era DC blocks can only resolve aliased signals up to roughly 120 MHz. It is also possible that other modes in the lower hybrid range are either excited by current fast ion populations (beam ions, fusion products) and/or will be by those introduced by up-and-coming RF heating systems like helicon and LHCD.

Bibliography

[1] H. Abu-Shawareb. Lawson criterion for ignition exceeded in an inertial fusion experiment. *Physical Review Letters*, 129(7):075001, Aug. 2022.

[2] J. Adam and J. Jacquinot. Eigenmode field structure of the fast magnetosonic wave in a tokamak and loading impedance of coupling structures. Technical Report EUR-CEA-FC–886, Association Euratom-CEA, Centre d'Etudes Nucláires de Fontenay-aux-Roses, Apr. 1977.

[3] T. D. Arber, K. Bennett, C. S. Brady, A. Lawrence-Douglas, M. G. Ramsay, N. J. Sircombe, P. Gillies, R. G. Evans, H. Schmitz, A. R. Bell, and C. P. Ridgers. Contemporary particle-in-cell approach to laser-plasma modelling. *Plasma Phys. Control. Fusion*, 57(11):113001, Sept. 2015.

[4] L. Askinazi, A. Belokurov, D. Gin, V. Kornev, S. Lebedev, A. Shevelev, A. Tukachinsky, and N. Zhubr. Ion cyclotron emission in NBI-heated plasmas in the TUMAN-3M tokamak. *Nucl. Fusion*, 58(8):082003, Aug. 2018.

[5] M. E. Austin and J. Lohr. Electron cyclotron emission radiometer upgrade on the DIII-D tokamak. *Review of Scientific Instruments*, 74(3):1457–1459, Mar. 2003.

[6] A. Axley and R. I. Pinsker. Investigation of ion cyclotron emissions on DIII-D during neutral beam injection and fast wave heating. 2009. BAPS.2009.DPP.JP8.73.

[7] M. A. Balihkin, Y. Y. Shprits, S. N. Walker, L. Chen, N. Cornilleau-Wehrlin, I. Dandouras, O. Santolik, C. Carr, K. H. Yearby, and B. Weiss. Observations of discrete harmonics emerging from equatorial noise. *Nature Communications*, 6(1):7703, Nov. 2015.

[8] V. S. Belikov and Y. I. Kolesnichenko. Magnetoacoustic cyclotron instability in a thermonuclear plasma. *Soviet Physics - Technical Physics*, 20:9.

[9] V. S. Belikov, Y. I. Kolesnichenko, and R. B. White. Destabilization of fast magnetoacoustic waves by circulating energetic ions in toroidal plasmas. *Physics of Plasmas*, 10(12):4771–4775, Dec. 2003.

[10] E. V. Belova, N. A. Crocker, J. B. Lestz, and E. D. Fredrickson. Application of simulations and theory of sub-cyclotron frequency modes to DIII-D. *Nuclear Fusion*, 62(10):106016, Sept. 2022.

[11] E. V. Belova, N. A. Crocker, S. X. Tang, J. B. Lestz, and E. D. Fredrickson. Global Alfvén eigenmode (GAE) simulations for NSTX(-U) and DIII-D. 2020. BAPS.2020.DPP.PP12.00025.

[12] E. V. Belova, E. D. Fredrickson, J. B. Lestz, N. A. Crocker, and NSTX-U Team. Numerical simulations of global Alfvén eigenmodes excitation and stabilization in NSTX-U. *Physics of Plasmas*, 26(9):092507, Sept. 2019.

[13] E. V. Belova, N. N. Gorelenkov, N. A. Crocker, J. B. Lestz, E. D. Fredrickson, S. Tang, and K. Tritz. Nonlinear simulations of beam-driven compressional Alfvén eigenmodes in NSTX. *Physics of Plasmas*, 24(4):042505, Apr. 2017.

[14] E. V. Belova, N. N. Gorelenkov, E. D. Fredrickson, K. Tritz, and N. A. Crocker. Coupling of neutral-beam-driven compressional Alfvén eigenmodes to kinetic Alfvén waves in NSTX tokamak and energy channeling. *Physical Review Letters*, 115(1):015001, June 2015.

[15] J. S. Bendat and A. G. Piersol. *Engineering Applications of Correlation and Spectral Analysis*. John Wiley and Sons, Inc, New York, NY, second edition, 1993.

[16] J. S. Bendat and A. G. Piersol. *Random Data - Bendat - 2010 - Wiley Series in Probability and Statistics - Wiley Online Library*. John Wiley and Sons, Inc, Hoboken, New Jersey, 4 edition, 2010.

[17] J. Breslau, M. Gorelenkova, F. Poli, J. Sachdev, A. Pankin, G. Perumpilly, X. Yuan, and L. Glant. Transp. [Computer Software] `https://doi.org/10.11578/dc.20180627.4`, jun 2018. TRANSP is a 1.5D equilibrium and transport solver for interpretation and prediction of tokamak discharges.

[18] D. A. J. Buchenauer. *Fast Ion Effects on Magnetic Instabilities in the PDX Tokamak*. PhD thesis, Princeton University, 1985.

[19] L. Carbajal and F. A. Calderón. On the 2d dynamics of the magnetoacoustic cyclotron instability driven by fusion-born ions. *Physics of Plasmas*, 28(1):014505, Jan. 2021.

[20] L. Carbajal, R. O. Dendy, S. C. Chapman, and J. W. S. Cook. Linear and nonlinear physics of the magnetoacoustic cyclotron instability of fusion-born ions in relation to ion cyclotron emission. *Physics of Plasmas*, 21(1):012106, Jan. 2014.

[21] L. Carbajal, R. O. Dendy, S. C. Chapman, and J. W. S. Cook. Quantifying fusion born ion populations in magnetically confined plasmas using ion cyclotron emission. *Physical Review Letters*, 118(10):105001, Mar. 2017.

[22] T. N. Carlstrom, G. L. Campbell, J. C. DeBoo, R. Evanko, J. Evans, C. M. Greenfield, J. Haskovec, C. L. Hsieh, E. McKee, R. T. Snider, R. Stockdale, P. K. Trost, and M. P. Thomas. Design and operation of the multipulse Thomson scattering diagnostic on DIII-D (invited). *Review of Scientific Instruments*, 63(10):4901–4906, Oct. 1992.

[23] S. Cauffman and R. Majeski. Ion cyclotron emission on the Tokamak Fusion Test Reactor. *Review of Scientific Instruments*, 66(1):817–819, Jan. 1995.

[24] S. Cauffman, R. Majeski, K. G. McClements, and R. O. Dendy. Alfvénic behaviour of alpha particle driven ion cyclotron emission in TFTR. *Nucl. Fusion*, 35(12):1597–1602, Dec. 1995.

[25] S. R. Cauffman. *Ion cyclotron emission from fusion plasmas*. PhD thesis, Princeton University, 1997.

[26] B. Chapman, R. O. Dendy, S. C. Chapman, L. A. Holland, S. W. A. Irvine, and B. C. G. Reman. Comparing theory and simulation of ion cyclotron emission from energetic ion populations with spherical shell and ring-beam distributions in velocity-space. *Plasma Physics and Controlled Fusion*, 62(5):055003, Mar. 2020.

[27] B. Chapman, R. O. Dendy, S. C. Chapman, K. G. McClements, G. S. Yun, S. G. Thatipamula, and M. H. Kim. Interpretation of suprathermal emission at deuteron cyclotron harmonics from deuterium plasmas heated by neutral beam injection in the KSTAR tokamak. *Nucl. Fusion*, 59(10):106021, Oct. 2019.

[28] B. Chapman, R. O. Dendy, S. C. Chapman, S. G. McClements, S. G. Thatipamula, and M. H. Kim. Nonlinear wave interactions generate high-harmonic cyclotron emission from fusion-born protons during a KSTAR ELM crash. *Nuclear Fusion*, 58:096027, July 2018.

[29] B. Chapman, R. O. Dendy, K. G. McClements, S. C. Chapman, G. S. Yun, S. G. Thatipamula, and M. H. Kim. Sub-microsecond temporal evolution of edge density during edge localized modes in KSTAR tokamak plasmas inferred from ion cyclotron emission. *Nuclear Fusion*, 57(12):124004, Dec. 2017.

[30] L. Chen, J. Vaclavik, and G. W. Hammett. Ion radial transport induced by ICRF waves in tokamaks. *Nuclear Fusion*, 28(3):389, Mar. 1988.

[31] S. Chowdury, N. A. Crocker, W. A. Peebles, T. L. Rhodes, B. G. Van Compernolle, M. W. Brookman, R. I. Pinsker, C. H. Lau, L. Bradly, and R. Lantsov. Local helicon wave measurements in DIII-D via Doppler backscattering. 2021. BAPS.2021.DPP.CP11.00085.

[32] J. W. S. Cook. Doublet splitting of fusion alpha-particle drive ion cyclotron emission. 2022.

[33] J. W. S. Cook, R. O. Dendy, and S. C. Chapman. Particle-in-cell simulations of the magnetoacoustic cyclotron instability of fusion-born alpha-particles in tokamak plasmas. *Plasma Phys. Control. Fusion*, 55(6):065003, Apr. 2013.

[34] J. W. S. Cook, R. O. Dendy, and S. C. Chapman. Stimulated emission of fast Alfvén waves within magnetically confined fusion plasmas. *Physical Review Letters*, 118(18):185001, May 2017.

[35] B. Coppi, S. Cowley, R. Kulsrud, P. Detragiache, and F. Pegoraro. High-energy components and collective modes in thermonuclear plasmas. *The Physics of Fluids*, 29(12):4060–4072, Dec. 1986.

[36] B. Coppi, G. Penn, and C. Riconda. Exictation of contained modes by high energy nuclei and correlated cyclotron emission. *Annals of Physics*, 261(2):117–162, Dec. 1997.

[37] G. A. Cottrell, V. P. Bhatnagar, O. Da Costa, R. O. Dendy, J. Jacquinot, K. G. McClements, D. C. McCune, M. F. F. Nave, P. Smeulders, and D. F. H. Start. Ion cyclotron emission measurements during JET deuterium-tritium experiments. *Nucl. Fusion*, 33(9):1365–1387, Sept. 1993.

[38] G. A. Cottrell and R. O. Dendy. Superthermal radiation from fusion products JET. *Phys. Rev. Lett.*, 60(1):33–36, Jan. 1988.

[39] N. A. Crocker, S. Kubota, W. A. Peebles, T. L. Rhodes, E. D. Fredrickson, E. Belova, A. Diallo, B. P. LeBlanc, and S. A. Sabbag. Density perturbation mode structure of high frequency compressional and global Alfvén eigenmodes in the National Spherical Torus Experiment using a novel reflectometer analysis technique. *Nuclear Fusion*, 58:016051, Dec. 2017.

[40] N. A. Crocker, W. A. Peebles, S. Kubota, J. Zhang, R. E. Bell, E. D. Fredrickson, N. N. Gorelenkov, B. P. LeBlanc, J. E. Mendard, M. Podestá, S. A. Sabbagh, K. Tritz, and H. Yuh. High spatial sampling global mode structure measurements via multichannel reflectometry in NSTX. *Plasma Physics and Controlled Fusion*, 53:105001, Aug. 2011.

[41] N. A. Crocker, S. X. Tang, K. E. Thome, J. B. Lestz, E. V. Belova, A. Zalzali, R. O. Dendy, W. A. Peebles, K. Barada, R. Hong, T. L. Rhodes, G. Wang, L. Zeng, T. A. Carter, G. H. DeGrandchamp, W. W. Heidbrink, and R. I. Pinsker. Novel internal measurements of ion cyclotron frequency range fast-ion driven modes. *Nuclear Fusion*, 62(2):026023, Jan. 2022.

[42] Culham Center for Fusion Energy. Fusion energy record demonstrates powerplant future.

[43] G. H. DeGrandchamp, W. W. Heidbrink, X. D. Du, K. E. Thome, L. Bardoczi, M. A. Van Zeeland, C. S. Collins, S. T. Vincena, S. X. Tang, N. A. Crocker, S. Sharapov, M. E. Koepke, S. H. Nogami, and S. Tripathi. Ion species mix, magnetic field, and distribution function dependence of instabilities in the ion cyclotron range of frequencies. In *16th IAEA Technical Meeting on Energetic Particles*, Sept. 2019.

[44] G. H. DeGrandchamp, W. W. Heidbrink, J. B. Lestz, M. A. Van Zeeland, X. D. Du, K. E. Thome, J. A. Boedo, N. A. Crocker, and R. I. Pinsker. Ion cyclotron emission dependence on the evanescent layer and fast ion density on the DIII-D tokamak. *In preparation.*

[45] G. H. DeGrandchamp, J. B. Lestz, M. A. Van Zeeland, X. D. Du, K. E. Thome, N. A. Crocker, W. W. Heidbrink, and R. I. Pinsker. Mode structure measurements of ion

cyclotron emission and sub-cyclotron modes on DIII-D. *Nuclear Fusion*, 62(10):106033, 2022.

[46] G. H. DeGrandchamp, K. E. Thome, W. W. Heidbrink, I. Holmes, and R. I. Pinsker. Upgrades to the ion cyclotron emission diagnostic on the DIII-D tokamak. *Review of Scientific Instruments*, 92(3):033543, Mar. 2021. Publisher: American Institute of Physics.

[47] R. Dendy, K. McClements, C. Lashmore-Davies, R. Majeski, and S. Cauffman. A mechanism for beam-driven excitation of ion cyclotron harmonic waves in the Tokamak Fusion Test Reactor. *Physics of Plasmas*, 1(10):3407–3413, Oct. 1994.

[48] R. O. Dendy. Interpretation of ion cyclotron emission from fusion and space plasmas. *Plasma Physics and Controlled Fusion*, 36(12B):B163–B172, Dec. 1994.

[49] R. O. Dendy, C. N. Lashmore-Davies, and K. F. Kam. A possible excitation mechanism for observed superthermal ion cyclotron emission from tokamak plasmas. *Physics of Fluids B: Plasma Physics*, 4(12):086032, Dec. 1992.

[50] R. O. Dendy, C. N. Lashmore-Davies, and K. F. Kam. The magnetoacoustic cyclotron instability of an extended shell distribution of energetic ions. *Physics of Fluids B: Plasma Physics*, 5(7):1937–1994, July 1993.

[51] R. O. Dendy, C. N. Lashmore-Davies, K. G. McClements, and G. A. Cottrell. The excitation of obliquely propagating fast Alfvén waves at fusion ion cyclotron harmonics. *Physics of Plasmas*, 1(6):1918–1928, June 1994.

[52] Department of Energy. DOE Explains...nuclear fusion reactions.

[53] Department of Energy. DOE Explains...tokamaks.

[54] R. D'Inca. *Ion cyclotron emission on ASDEX upgrade*. PhD thesis, Ludwig-Maximilians-Universität, Munich, Germany, 2014.

[55] H. H. Duong, W. W. Heidbrink, E. J. Strait, T. W. Petrie, R. Lee, R. A. Moyer, and J. G. Watkins. Loss of energetic beam ions during TAE instabilities. *Nucl. Fusion*, 33(5):749–765, May 1993.

[56] Équipe TFR. High-power neutral injection and ion power balance in TFR. *Nucl. Fusion*, 18(9):1271–1303, Sept. 1978.

[57] J. R. Ferron and E. J. Strait. Real time analysis of tokamak discharge parameters. *Review of Scientific Instruments*, 63(10):4799–4802, Oct. 1992.

[58] E. D. Fredrickson, R. E. Bell, D. S. Darrow, G. Y. Fu, N. N. Gorelenkov, B. P. LeBlanc, S. S. Medley, J. E. Menard, H. Park, A. L. Roquemore, W. W. Heidbrink, S. A. Sabbagh, D. Stutman, K. Tritz, N. A. Crocker, S. Kubota, W. Peebles, K. C. Lee, and F. M. Levinton. Collective fast ion instability-induced losses in National Spherical Tokamak Experiment. *Physics of Plasmas*, 13(5):056109, May 2006.

[59] E. D. Fredrickson, N. Gorelenkov, C. Z. Cheng, R. Bell, D. Darrow, D. Johnson, S. Kaye, B. LeBlanc, J. Menard, S. Kubota, and W. Peebles. Observation of compressional Alfvén modes during neutral-beam heating on the National Spherical Torus Experiment. *Phys. Rev. Lett.*, 87(14):145001, Sept. 2001.

[60] E. D. Fredrickson, N. N. Gorelenkov, R. E. Bell, A. Diallo, B. P. LeBlanc, J. B. Lestz, M. Podestá, and the NSTX team. Chirping ion cyclotron emission (ICE) on NSTX-U. *Nuclear Fusion*, 61(8):086007, July 2021.

[61] E. D. Fredrickson, N. N. Gorelenkov, R. E. Bell, A. Diallo, B. P. LeBlanc, and M. Podestá. Emission in the ion cyclotron range of frequencies (ICE) on NSTX and NSTX-U. *Physics of Plasmas*, 26(3):032111, Mar. 2019.

[62] E. D. Fredrickson, N. N. Gorelenkov, and J. Menard. Phenomenology of compressional Alfvén eigenmodes. *Physics of Plasmas*, 11(7):3653–3659, July 2004.

[63] E. D. Fredrickson, N. N. Gorelenkov, M. Podestá, N. A. Crocker, S. P. Gerhardt, R. E. Bell, A. Diallo, B. LeBlanc, F. M. Levinton, and H. Yuh. Non-linear modulation of short wavelength compressional Alfvén eigenmodes. *Physics of Plasmas*, 20:042122, Apr. 2013.

[64] T. Fülöp, Y. I. Kolesnichenko, M. Lisak, and D. Anderson. Origin of superthermal ion cyclotron emission in tokamaks. *Nuclear Fusion*, 37(9):1281–1293, Sept. 1997.

[65] T. Fülöp and M. Lisak. Ion cyclotron emission from fusion products and beam ions in the Tokamak Fusion Test Reactor. *Nuclear Fusion*, 38(5):761–773, May 1998.

[66] J. Galdon-Quiroga, M. Garcìa-Munoz, L. Sanchis-Sanchez, M. Mantsinen, S. Fietz, V. Igochine, M. Maraschek, M. Rodriguez-Ramos, B. Sieglin, A. Snicker, G. Tardini, D. Vezinet, M. Weiland, L. G. Eriksson, T. A. U. Team, and T. E. M. Team. Velocity space resolved absolute measurement of fast ion losses induced by a tearing mode in the ASDEX Upgrade tokamak. *Nucl. Fusion*, 58(3):036005, Jan. 2018.

[67] E. Gibney. Nuclear-fusion reactor smashes energy record. *Nature*, 602(7897):371, Feb. 2022.

[68] N. N. Gorelenkov. Energetic particle-driven compressional Alfvén eigenmodes and prospects for ion cyclotron emission studies in fusion plasmas. *New J. Phys.*, 18(10):105010, Oct. 2016.

[69] N. N. Gorelenkov. Ion cyclotron emission studies: Retrospects and prospects. *Plasma Phys. Rep.*, 42(5):430–439, May 2016.

[70] N. N. Gorelenkov and C. Z. Cheng. Alfvén cyclotron instability and ion cyclotron emission. *Nucl. Fusion*, 35(12):1743–1752, Dec. 1995.

[71] N. N. Gorelenkov and C. Z. Cheng. Excitation of Alfvén cyclotron instability by charged fusion products in tokamaks. *Physics of Plasmas*, 2(6):1961–1971, June 1995.

[72] N. N. Gorelenkov, E. D. Fredrickson, W. W. Heidbrink, N. A. Crocker, S. Kubota, and W. A. Peebles. Discrete compressional Alfvén eigenmode spectrum in tokamaks. *Nuclear Fusion*, 46(10):S933–S941, Sept. 2006.

[73] M. V. Gorelenkova and N. N. Gorelenkov. Magnetosonic eigenmodes near the magnetic field well in a spherical torus. *Physics of Plasmas*, 5(11):4104–4106, Nov. 1998.

[74] G. J. Greene. Measurements of ion cyclotron emission and ICRF-driven waves in TFTR. *Europhysics Conference Abstracts*, 14B(IV):1540–1543, 1990.

[75] B. A. Grierson, M. A. Van Zeeland, J. T. Scoville, B. Crowley, I. Bykov, J. M. Park, W. W. Heidbrink, A. Nagy, S. R. Haskey, and D. Liu. Testing the DIII-D co/counter off-axis neutral beam injected power and ability to balance injected torque. *Nuclear Fusion*, 61(11):116049, Oct. 2021.

[76] E. G. Harris. Unstable plasma oscillations in a magnetic field. *Phys. Rev. Lett.*, 2(2):34–36, Jan. 1959.

[77] W. W. Heidbrink. Alpha particle physics in a tokamak burning plasma environment. *Physics of Plasmas*, 9(5):2113–2119, Apr. 2002.

[78] W. W. Heidbrink, M. E. Austin, R. K. Fisher, M. García-Muñoz, G. Matsunaga, G. R. McKee, R. A. Moyer, C. M. Muscatello, M. Okabayashi, D. C. Pace, K. Shinohara, W. M. Solomon, E. J. Strait, M. A. V. Zeeland, and Y. B. Zhu. Characterization of off-axis fishbones. *Plasma Phys. Control. Fusion*, 53(8):085028, July 2011.

[79] W. W. Heidbrink, E. D. Fredrickson, N. N. Gorelenkov, T. L. Rhodes, and M. A. V. Zeeland. Observation of compressional Alfvén eigenmodes (CAE) in a conventional tokamak. *Nucl. Fusion*, 46(2):324–334, Jan. 2006.

[80] W. W. Heidbrink, K. Jinchoon, and R. J. Groebner. Comparison of experimental and theoretical fast ion slowing-down times in DIII-D. *Nuclear Fusion*, 28(10):1897–1901, Sept. 1988.

[81] W. W. Heidbrink, C. Paz-Soldan, D. A. Spong, X. D. Du, K. E. Thome, M. E. Austin, A. Lvovskiy, R. A. Moyer, R. I. Pinsker, and M. A. Van Zeeland. Low-frequency whistler waves in quiescent runaway electron plasmas. *Plasma Physics and Controlled Fusion*, 61(1):014007, Nov. 2018.

[82] W. W. Heidbrink and G. J. Sadler. The behaviour of fast ions in tokamak experiments. *Nuclear Fusion*, 34(4):535–615.

[83] W. W. Heidbrink and R. B. White. Mechanisms of energetic-particle transport in magnetically confined plasmas. *Physics of Plasmas*, 27(3):030901, Mar. 2020.

[84] C. T. Holcomb, M. A. Makowski, R. J. Jayakumar, S. A. Allen, R. M. Ellis, R. Geer, D. Behne, K. L. Morris, L. G. Seppala, and J. M. Moller. Motional stark effect diagnostic expansion on DIII-D for enhanced current and E_r profile measurements. *Review of Scientific Instruments*, 77(10):10E506, Oct. 2006.

[85] M. Ichimura, H. Higaki, S. Kakimoto, Y. Yamaguchi, K. Nemoto, M. Katano, M. Ishikawa, S. Moriyama, and T. Suzuki. Observation of spontaneously excited waves in the ion cyclotron frequency range on JT-60U. *Nucl. Fusion*, 48(3):035012, Feb. 2008.

[86] H. Ikezi, R. I. Pinsker, S. C. Chiu, and J. S. DeGrassie. Fast wave propagation studies in the DIII-D tokamak. *Physics of Plasmas*, 3(6):2306–2315, June 1996.

[87] ITER. JET makes history, again.

[88] P. Jacquet, G. Berger-By, V. Bobkov, T. Blackman, I. E. Day, F. Durodié, M. Graham, T. Hellsten, M. Laxåback, M.-L. Mayoral, I. Monakhov, M. Nightingale, S. E. Sharapov, M. Vrancken, and JET-EFDA contributors. Parasitic signals in the receiving band of the sub-harmonic arc detection system on JET ICRF antennas. *AIP Conference Proceedings*, 1406:17–90, Dec. 2011.

[89] M. Keilhacker, A. Gibson, C. Gormenzano, P. J. Lomas, P. R. Thomas, M. L. Watkins, P. Andrew, B. Balet, D. Borba, C. D. Challis, I. Coffey, G. A. Cottrell, H. P. L. De Esch, N. Deliyanakis, A. Fasoli, C. W. Gowers, H. Y. Guo, G. T. A. Huysmans, T. T. C. Jones, W. Kerner, R. W. T. König, M. J. Loughlin, A. Maas, F. B. Marcus, M. F. F. Nave, F. G. Rimini, G. J. Sadler, S. E. Sharapov, G. Sips, P. Smeulders, F. X. Söldner, A. Taroni, B. J. D. Tubbing, v. M. G., D. J. Ward, and the JET team. High fusion performance from deuterium-tritium plasmas in JET. *Nuclear Fusion*, 39(2):209, Feb. 1999.

[90] J. S. Kim, D. H. Edgell, J. M. Greene, E. J. Strait, and M. S. Chance. MHD mode identification of tokamak plasmas from Mirnov signals. *Plasma Physics and Controlled Fusion*, 41(11):1399–1420, Nov. 1999.

[91] M. H. Kim, S. G. Thatipamula, J. E. Lee, M. J. Choi, H. K. Park, T. Akiyama, and G. S. Yun. Distinct stages of radio frequency emission at the onset of pedestal collapse in KSTAR H-mode plasmas. *Nuclear Fusion*, 58(9):096034, July 2018.

[92] H. Kimura, Y. Kusama, M. Saigusa, G. J. Kramer, K. Tobita, M. Nemoto, T. Kondoh, T. Nishitani, O. Da Costa, and T. Ozeki. Alfvén eigenmode and energetic particle research at JT-60U. *Nuclear Fusion*, 38(9):1303–1314, Sept. 1998.

[93] Y. I. Kolesnichenko, T. Fülöp, M. Lisak, and D. Anderson. Localized fast magnetoacoustic eigenmodes in tokamak plasmas. *Nuclear Fusion*, 38(12):1871–1879, Dec. 1998.

[94] Y. I. Kolesnichenko, A. V. Tykhyy, and R. B. White. Spatial channeling in toroidal plasmas: overview and new results. *Nuclear Fusion*, 60(11):112006, Aug. 2020.

[95] Y. I. Kolesnichenko, V. V. Yakovenko, Yu. V. Lutsenko, R. B. White, and A. Weller. Effects of energetic-ion-driven instabilities on plasma heating, transport and rotation in toroidal systems. *Nuclear Fusion*, 50(8):084011, July 2010.

[96] Y. I. Kolesnichenko, Y. V. Yakovenko, and V. V. Lutsenko. Channeling of the energy and momentum during energetic-ion-driven instabilities in fusion plasmas. *Physical Review Letters*, 104(7):075001, Feb. 2010.

[97] A. Kuley, Z. Lin, J. Bao, X. S. Wei, Y. Xiao, W. Zhang, G. Y. Sun, and N. J. Fisch. Verification of nonlinear particle simulation of radio frequency waves in tokamak. *Physics of Plasmas*, 22(10):102515, Oct. 2015.

[98] L. L. Lao, H. St. John, R. D. Stambaugh, A. G. Kellman, and W. Pfeiffer. Reconstruction of current profile parameters and plasma shapes in tokamaks. *Nuclear Fusion*, 25(11):1611–1622, Nov. 1985.

[99] Lawrence Livermore National Laboratory. Pursuing fusion ignition.

[100] J. D. Lawson. Some criteria for a power producing thermonuclear reactor. *Proceedings of the Physical Society. Section B*, 70(1):6, Jan. 1957.

[101] S. V. Lebedev, L. G. Askinazi, A. A. Belokurov, D. B. Gin, V. A. Kornev, A. A. Shabelsky, A. E. Shevelev, A. S. Tukachinsky, N. A. Zhubr, and A. G. Litvak. Observation of ion cyclotron emission from ohmically and NBI heated plasmas in TUMAN-3M tokamak. *EPJ Web of Conferences*, 149:03010, 2017.

[102] J. B. Lestz. *Theory and Simulations of Compressional and Global Alfvén Eigenmode Stability in Spherical Tokamaks*. PhD thesis, Princeton University, Princeton, NJ, 2020.

[103] J. B. Lestz, E. V. Belova, and N. N. Gorelenkov. Hybrid simulations of sub-cyclotron compressional and global Alfvén eigenmode stability in spherical tokamaks. *Physics of Plasmas*, 61(8):086016, July 2021.

[104] J. B. Lestz, N. N. Gorelenkov, E. V. Belova, S. X. Tang, and N. A. Crocker. Analytic stability boundaries for compressional and global Alfvén eigenmodes driven by fast ions. I. Interaction via ordinary and anomalous cyclotron resonances. *Physics of Plasmas*, 27(2):022513, Feb. 2020.

[105] J. B. Lestz, K. Saito, S. Kamio, H. Igami, K. Ogawa, M. Osakabe, W. W. Heidbrink, G. H. DeGrandchamp, and S. Vincena. Experimental comparison of ion cyclotron emission in the LHD stellarator and DIII-D tokamak. 2022. BAPS.2022.DPP.BP11.00032.

[106] S. J. Levinson, J. M. Powers, and R. D. Bengston. Space/time statistics of the turbulence in a tokamak edge plasma. *Nuclear Fusion*, 24(5):527–539, May 1984.

[107] Z. Lin, T. S. Hahm, W. W. Lee, W. M. Tang, and R. B. White. Turbulent Transport Reduction by Zonal Flows: Massively Parallel Simulations. 281:3, 1998.

[108] J. D. Lindl, S. W. Haan, O. L. Landen, A. R. Christopherson, and R. Betti. Progress toward a self-consistent set of 1d ignition capsule metrics in ICF. *Physics of Plasmas*, 25(12):122704, Dec. 2018.

[109] L. Liu, R. Ochoukov, K. G. McClements, R. O. Dency, V. V. Bobkov, M. Weiland, R. Bilato, R. Faugel, D. Moseev, M. Salewski, W. Zhang, X. Zhang, Y. Zhu, B. Chapman, and A. Zalzali. Explanation of core ion cyclotron emission from beam-ion heated plasams in asdex upgrade by the magnetoacoustic cyclotron instability. *Nuclear Fusion*, 61(8):026004, Nov. 2021.

[110] L. Liu, X. Zhang, Y. Zhu, C. Qin, S. Yuan, Y. Mao, M. Li, K. Zhang, J. Cheng, L. Ai, and Y. Cheng. Ion cyclotron emission driven by deuterium neutral beam injection and core fusion reaction ions in EAST. *Nuclear Fusion*, 60(4):044002, Apr. 2020.

[111] L. N. Liu, X. J. Zhang, Y. B. Zhu, C. M. Zin, Y. P. Zhao, S. Yuan, Y. Z. Mao, M. H. Li, Y. Chen, J. Cheng, L. L. Ping, H. Li, and L. Ai. Ion cyclotron emission diagnostic system on the experimental advanced superconducting tokamak and first detection of energetic-particle-driven radiation. *Review of Scientific Instruments*, 90(6):063504.

[112] J. L. Luxon. A design retrospective of the DIII-D tokamak. *Nuclear Fusion*, 42(5):614–633, May 2002.

[113] J. L. Luxon. A brief introduction to the DIII-D tokamak. *Fusion Science and Technology*, 48(2):828–833, Oct. 2005.

[114] G. F. Matthews, B. Bazylev, A. Baron-Wiechec, J. Coenen, K. Heinola, V. Kiptily, H. Maier, C. Reux, V. Riccardo, F. Rimini, G. Sergienko, V. Thompson, A. Widdowson, and J.E.T. Contributors. Melt damage to the JET ITER-like wall and divertor. *Physica Scripta*, 2016(T167):014070, Jan. 2016.

[115] K. G. McClements, A. Brisset, B. Chapman, S. C. Chapman, R. O. Dendy, P. Jacquet, V. G. Kiptily, M. Mantsinen, and B. C. G. R. and. Observations and modelling of ion cyclotron emission observed in JET plasmas using a sub-harmonic arc detection system during ion cyclotron resonance heating. *Nucl. Fusion*, 58(9):096020, July 2018.

[116] K. G. McClements, R. D'Inca, R. O. Dendy, L. Carbajal, S. C. Chapman, J. W. S. Cook, R. W. Harvey, W. W. Heidbrink, and S. D. Pinches. Fast particle-driven ion cyclotron emission (ICE) in tokamak plasmas and the case for an ICE diagnostic in ITER. *Nucl. Fusion*, 55(4):043013, Apr. 2015.

[117] O. Meneghini, S. P. Smith, L. L. Lao, O. Izacard, Q. Ren, J. M. Park, J. Candy, Z. Wang, C. J. Luna, V. A. Izzo, B. A. Grierson, P. B. Snyder, C. Holland, J. Penna, G. Lu, P. Raum, A. McCubbin, D. M. Orlov, E. A. Belli, N. M. Ferraro, R. Prater, T. H. Osborne, A. D. Turnbull, and G. M. Staebler. Integrated modeling applications for tokamak experiments with OMFIT. *Nucl. Fusion*, 55(8):083008, July 2015.

[118] Mini-Circuits. *Coaxial Lowpass Filter BLP-100+*, May 2020.

[119] D. Moseev and M. Salewski. Bi-Maxwellian, slowing-down, and ring velocity distributions of fast ions in magnetized plasmas. *Physics of Plasmas*, 26(2):020901.

[120] C. J. Murphy, M. Abrahim, P. M. Anderson, H. K. Chiu, H. J. Grunloh, M. J. Hansink, K. L. Holtrop, R.-M. Hong, A. G. Kellman, D. H. Kellman, P. S. Mauzey, S. Noraky, C. J. Pawley, J. Rauch, J. T. Scoville, M. A. Van Zeeland, H. H. Yip, M. Murakami, J. M. Park, and W. W. Heidbrink. Overview of DIII-D off-axis neutral beam project. In *2011 IEEE/NPSS 24th Symposium on Fusion Engineering*, pages 1–6, June 2011.

[121] R. Ochoukov, R. Bilato, V. Bobkov, S. C. Chapman, R. Dendy, M. Dreval, H. Faugel, A. Kappatou, Y. O. Kazakov, M. Mantsinen, K. G. McClements, D. Moseev, S. K. Nielsen, J. M. Noterdaeme, M. Salewski, P. Schneider, and M. Weiland. High frequency Alfvén eigenmodes detected with ion-cyclotron-emission diagnostics during NBI and ICRF heated plasmas on the ASDEX Upgrade tokamak. *Nucl. Fusion*, 60(12):126043, Nov. 2020.

[122] R. Ochoukov, R. Bilato, V. Bobkov, R. Dendy, M. Dreval, H. Faugel, M. Garcia-Muoz, A. Kappatou, M. Mantsinen, K. G. McClements, D. Moseev, M. Salewski, M. Schneider, and M. Weiland. Wavenumber measurements of ICE with low field side B-dot probes on AUG. In *27th Meeting of ITPA Topical Group on Energetic Particle Physics*, May 2022.

[123] R. Ochoukov, V. Bobkov, B. Chapman, R. Dendy, M. Dunne, H. Faugel, M. García-Muñoz, B. Geiger, P. Hennequin, K. G. McClements, D. Moseev, S. Nielsen, J. Rasmussen, P. Schneider, M. Weiland, J.-M. Noterdaeme, ASDEX Upgrade Team, and EUROfusion MST1 Team. Observations of core ion cyclotron emission on ASDEX Upgrade tokamak. *Review of Scientific Instruments*, 89(10):10J101, Oct. 2018.

[124] H. Ohtsuka, S. Yamamoto, M. Maeno, T. Matsuda, Y. Miura, N. Suzuki, M. Mori, and S. Teruaki. Observation of ICRF waves during neutral beam injection in tokamaks. *JAERI-M*, 84(150), Sept. 1984.

[125] H. J. C. Oliver, S. E. Sharapov, R. Akers, I. Klimek, and M. Cecconello. Compressional Alfvén and ion–ion hybrid waves in tokamak plasmas with two ion species. *Plasma Physics and Controlled Fusion*, 56(12):125017, Dec. 2014.

[126] O. Ostwald. *Group and Phase Delay Measurements with Vector Network Analyzer ZVR*. Rhode and Schwartz, 1997.

[127] D. C. Pace, W. W. Heidbrink, M. A. Van Zeeland, and Y. Zhu. In *43rd EPS Conference on Plasma Physics*, July 2016. 02.101.

[128] A. Pankin, D. McCune, A. Robert, G. Bateman, and A. Kritz. The tokamak Monte Carlo fast ion module NUBEAM in the National Transport Code Collaboration library. *Computer Physics Communications*, 159(3):157–184, June 2004.

[129] R. I. Pinsker. Whistlers, helicons, and lower hybrid waves: The physics of radio frequency wave propagation and absorption for current drive via Landau damping. *Physics of Plasmas*, 22(9):090901, Sept. 2015.

[130] R. I. Pinsker. *Personal communication*, Nov. 2020.

[131] R. I. Pinsker, X. Chen, C. C. Petty, B. G. Van Compernolle, C. P. Moeller, M. Porkolab, S. J. Wukitch, and A. Seltzman. DIII-D experimental program on the physics and technology of efficient RF off-axis current drive. 2022. BAPS.2021.DPP.UO03.00008.

[132] M. Porkolab, R. I. Pinsker, G. H. DeGrandchamp, S. G. Baek, M. W. Brookman, B. Van Compernolle, S. Denk, A. M. Garofalo, C. C. Petty, and K. E. Thome. Initial assessment of parametric decay instabilities during high power helicon wave. 2021. BAPS.2021.DPP.UO07.00007.

[133] M. Porkolab, R. I. Pinsker, G. H. DeGrandchamp, S. G. Baek, B. Van Compernolle, S. Denk, C. C. Petty, S. X. Tang, and K. E. Thome. Parametric decay instabilities driven by high-power helicon waves in DIII-D. In *24th Topical Conference on Radio-frequency Power in Plasmas*, Sept. 2022.

[134] B. C. G. Reman. *Interpreting Observations of Ion Cyclotron Emission from Energetic Ion Populations in Large Helical Device plasmas*. PhD thesis, University of Warwick, 2018.

[135] B. C. G. Reman, R. O. Dendy, T. Akiyama, S. C. Chapman, J. W. S. Cook, H. Igami, S. Inagaki, K. Saito, R. Seki, M. H. Kim, S. G. Thatipamula, and G. S. Yun. Density dependence of ion cyclotron emission from deuterium plasmas in the large helical device. *Nuclear Fusion*, 61(6):066023, May 2021.

[136] B. C. G. Reman, R. O. Dendy, T. Akiyama, S. C. Chapman, J. W. S. Cook, H. Igami, S. Inagaki, K. Saito, and G. S. Yun. Interpreting observations of ion cyclotron emission from large helical device plasmas with beam-injected ion populations. *Nucl. Fusion*, 59(9):096013, Sept. 2019.

[137] B. C. G. Reman, R. O. Dendy, H. Igami, T. Akiyama, M. Salewski, S. C. Chapman, J. W. S. Cook, S. Inagaki, K. Saito, R. Seki, M. Toida, M. H. Kim, S. G. Thatipamula, and G. S. Yun. First observation and interpretation of spontaneous collective radiation from fusion-born ions in a stellarator plasma. *Plasma Physics and Controlled Fusion*, 64(8):085008, June 2022.

[138] A. S. Richardson. *NRL Plasma Formulary*. Naval Research Laboratory, 2019.

[139] A. Saikin, J. Zhang, R. Allen, C. Smith, L. Kistler, H. Spence, R. Torbert, C. Kletzing, and V. Jordanova. The occurrence and wave properties of H^+-, He^+-, and O^+-band EMIC waves observed by the Van Allen probes. *Journal of Geophysical Research: Space Physics*, 120(9):7477–7492, Sept. 2015.

[140] K. Saito, H. Igami, M. Toida, T. Akiyama, S. Kamio, R. Seki, and the LHD experiment group. RF wave detection with high-frequency magnetic probes in LHD. *Plasma and Fusion Research*, 13(0):3402043–3402043, Apr. 2018.

[141] K. Saito, H. Kasahara, T. Seki, R. Kumazawa, T. Mutoh, T. Watanabe, F. Shimpo, G. Nomura, M. Osakabe, M. Ichimura, H. Higaki, and A. Komori. Measurement of ion cyclotron emissions by use of ICRF heating antennas in LHD. *Fusion Engineering and Design*, 84(7):1676–1679, Jan. 2019.

[142] K. Saito, R. Kumazawa, T. Seki, H. Kasahara, G. Nomura, F. Shimpo, H. Igami, M. Isobe, K. Ogawa, K. Toi, M. Osakabe, M. Nishiura, T. Watanabe, S. Yamamoto, M. Ichimura, and T. Mutoh. Measurement of ion cyclotron emissions by using high-frequency magnetic probes in the LHD. *Plasma Sci. Technol.*, 15(3):209–212, Mar. 2013.

[143] S. Sato, M. Ichimura, Y. Yamaguchi, M. Katano, Y. Imai, T. Murakami, Y. Miyake, T. Yokoyama, S. Moriyama, T. Kobayashi, A. Kojima, K. Shinohara, Y. Sakamoto, T. Watanabe, H. Hojo, and T. Imai. Observation of ion cyclotron emission owing to DD fusion product H ions in JT-60U. *Plasma and Fusion Research*, 5:S2067–S2067, 2010.

[144] P. Schild, G. A. Cottrell, and R. O. Dendy. Sawtooth oscillations in ion cyclotron emission from JET. *Nucl. Fusion*, 29(5):834–839, May 1989.

[145] J. T. Scoville, M. D. Boyer, B. J. Crowley, N. W. Eidietis, C. J. Pawley, and J. M. Rauch. New capabilities and upgrade path for the DIII-D neutral beam heating system. *Fusion Engineering and Design*, 146:6–9, Sept. 2019.

[146] M. Seki, M. Saigusa, M. Nemoto, K. Kusama, T. Tobita, M. Kuriyama, and K. Uehara. Observation of ion-cyclotron-wave instability caused by perpendicular neutral beam injection in the JT-60 tokamak. *Phys. Rev. Lett.*, 62(17):1989–1992, Apr. 1989.

[147] A. G. Shalashov, E. V. Suvorov, L. V. Lubyako, H. Massberg, and the W7-AS Team. NBI-drive ion cyclotron instabilities at the W7-AS stellarator. *Plasma Physics and Controlled Fusion*, 45(4):395–412, Mar. 2003.

[148] S. E. Sharapov, M. K. Lilley, R. Akers, N. B. Ayed, M. Cecconello, J. W. S. Cook, G. Cunningham, and E. Verwichte. Bi-directional Alfvén cyclotron instabilities in the mega-amp spherical tokamak. *Physics of Plasmas*, 21(11):082501, Aug. 2014.

[149] S. E. Sharapov, H. J. C. Oliver, N. B. Ayed, M. Cecconello, G. Cunningham, J. R. Harrison, I. Klimek, and R. Akers. Alfvén cyclotron instabilities in D and H-D plasmas on MAST. In *41st EPS Conference on Plasma Physics*, June 2014. P5.032.

[150] H. Smith, T. Fülöp, M. Lisak, and D. Anderson. Localization of compressional Alfvén eigenmodes in spherical tori. *Physics of Plasmas*, 10(5):1437–1442, May 2003.

[151] H. M. Smith and E. D. Fredrickson. Compressional Alfvén eigenmodes in rotating spherical tokamak plasmas. *Plasma Physics and Controlled Fusion*, 59(3):035007, Feb. 2017.

[152] H. M. Smith and E. Verwichte. Compressional Alfvén eigenmode structure in spherical tokamaks. *Plasma Physics and Controlled Fusion*, 51(7):075001, May 2009.

[153] T. H. Stix. *Waves in Plasmas*. American Institute of Physics, 1992.

[154] J. D. Strachan. Studies of global energy confinement in TFTR supershots. *Nuclear Fusion*, 34(7):1017, July 1994.

[155] J. D. Strachan, M. G. Bell, M. Bitter, R. V. Budny, R. J. Hawryluk, K. W. Hill, K. W. Hill, H. Hsuan, D. L. Jassby, L. C. Johnson, B. LeBlanc, D. K. Mansfield, E. S. Marmar, D. M. Meade, D. R. Mikkelsen, D. Mueller, H. K. Park, A. T. Ramsey, S. D. Scott, J. A. Snipes, E. J. Synakowski, G. Taylor, and J. L. Terry. Neutron emission from TFTR supershots. *Nuclear Fusion*, 33(7):991, July 1993.

[156] J. D. Strachan, P. L. Colestock, S. L. Davis, D. Eames, P. Efthimion, H. P. Eubank, R. J. Goldston, L. R. Grisham, R. J. Hawryluk, J. C. Hosea, J. Hovey, D. L. Jassby, D. W. Johnson, A. A. Mirin, G. Schilling, R. Stooksberry, L. D. Stewart, and H. H. Towner. Fusion neutron production during deuterium neutral-beam injection into the PLT tokamak. *Nuclear Fusion*, 53(7):074019.

[157] D. Stutman, L. Delgado-Aparicio, N. Gorelenkov, M. Finkenthal, E. Fredrickson, S. Kaye, E. Mazzucato, and K. Tritz. Correlation between electron transport and shear Alfvén activity in the National Spherical Torus Experiment. *Phys. Rev. Lett.*, 102(11):115002, Mar. 2009.

[158] S. Sumida, K. Shinohara, M. Ichimura, T. Bando, A. Bierwage, and S. Ide. Identification of slow-wave ion cyclotron emission on JT-60U. *Nuclear Fusion*, 61(11):116036, Oct. 2021.

[159] S. Sumida, K. Shinohara, R. Ikezoe, M. Ichimura, M. Sakamoto, M. Hirata, and S. Ide. Characteristics of fast 3He ion velocity distribution exciting ion cyclotron emission on JT-60U. *Plasma Physics and Controlled Fusion*, 61(2):025014, Jan. 2019.

[160] S. Tang, G. DeGrandchamp, R. Pinsker, K. Thome, B. Van Compernolle, and M. Porkolab. Magnetic fluctuation measurements from first high-power helicon experiments on DIII-D. In *24th Topical Conference on Radio-frequency Power in Plasmas*, Sept. 2022.

[161] S. X. Tang, T. A. Carter, N. A. Crocker, W. W. Heidbrink, J. B. Lestz, R. I. Pinsker, K. E. Thome, M. A. Van Zeeland, and E. V. Belova. Stabilization of Alfvén eigenmodes in DIII-D via controlled energetic ion density ramp and validation of theory and simulations. *Phys. Rev. Lett.*, 126(15):155001, Apr. 2021.

[162] S. G. Thatipamula, G. S. Yun, J. Leem, H. K. Park, K. W. Kim, T. Akiyama, and S. G. Lee. Dynamic spectra of radio frequency bursts associated with edge-localized modes. *Plasma Phys. Control. Fusion*, 58(6):065003, June 2016.

[163] K. E. Thome. Initial results of the ion cyclotron emission diagnostic. page 35, 2017.

[164] K. E. Thome, D. C. Pace, R. I. Pinsker, O. Meneghini, C. A. del Castillo, and Y. Zhu. Radio frequency measurements of energetic-particle-driven emission using the ion cyclotron emission diagnostic on the DIII-D tokamak. *Review of Scientific Instruments*, 89(10):10I102, July 2018.

[165] K. E. Thome, D. C. Pace, R. I. Pinsker, M. A. Van Zeeland, W. W. Heidbrink, and M. E. Austin. Central ion cyclotron emission in the DIII-D tokamak. *Nucl. Fusion*, 59(8):086011, Aug. 2019.

[166] J. Tollefson and E. Gibney. Nuclear-fusion lab achieves 'ignition': what does it mean? *Nature*, 612(7941):597–598, Dec. 2022.

[167] B. Van Compernolle, M. W. Brookman, C. P. Moeller, R. I. Pinsker, A. M. Garofalo, R. O'Neill, D. Geng, A. Nagy, J. P. Squire, K. Schultz, C. Pawley, D. Ponce, A. C. Torrezan, J. Lohr, B. Coriton, E. Hinson, R. Kalling, A. Marinoni, E. H. Martin, R. Nguyen, C. C. Petty, M. Porkolab, T. Raines, J. Ren, C. Rost, O. Schmitz, H. Torreblanca, H. Q. Wang, J. Watkins, and K. Zeller. The high-power helicon program at DIII-D: gearing up for first experiments. *Nuclear Fusion*, 61(11):116034, Sept. 2021.

[168] B. G. Van Compernolle, M. W. Brookman, R. I. Pinsker, C. Moeller, J. P. Squire, A. M. Garofalo, A. Nagy, A. Torrezan, D. Ponce, C. J. Pawley, S. Chowdury, N. A. Crocker, G. H. DeGrandchamp, E. T. Hinson, J. Lohr, A. Marinoni, E. H. Martin, C. C. Petty, M. Porkolab, C. C. Rost, O. Schmitz, K. E. Thome, H. Wang, J. G. Watkins, and K. Zeller. Commissioning and first results of the DIII-D helicon system. 2021. BAPS.2021.DPP.UO07.00006.

[169] M. A. Van Zeeland, R. L. Boivin, T. N. Carlstrom, T. Deterly, and D. K. Finkenthal. Fiber optic two-color vibration compensated interferometer for plasma density measurements. *Review of Scientific Instruments*, 77(10):10F325, Oct. 2006.

[170] M. A. Van Zeeland, J. H. Yu, W. W. Heidbrink, N. H. Brooks, K. H. Burrell, M. S. Chu, A. W. Hyatt, C. Muscatello, R. Nazikian, N. A. Pablant, D. C. Pace, W. M. Solomon, and M. R. Wade. Imaging key aspects of fast ion physics in the DIII-D tokamak. *Nuclear Fusion*, 50(8):084002, July 2010.

[171] G. Vayakis, C. I. Walker, F. Clairot, R. Sabot, V. Tribaldos, T. Estrada, E. Blanco, J. Sánchez, G. G. Denisov, V. I. Belousov, V. P. Silva, F. Da, M. E. Manso, L. Cupido, J. Dias, N. Valverde, V. A. Vershdov, D. A. Shelukhin, S. V. Soldatov, A. O. Urazbaev, and H. S. Frolov, E. Yu. Status and prospects for mm-wave reflectometry in ITER. *Nuclear Fusion*, 46(9):S836, Aug. 2006.

[172] S. T. Vincena, W. W. Heidbrink, N. A. Crocker, G. H. DeGrandchamp, X. D. Du, M. Koepke, S. Nogami, S. Sharapov, S. X. Tang, K. E. Thome, S. Tripathi, and M. A. Van Zeeland. The effect of species mix and fast-ion distribution on emission of fast magnetosonic waves near the ion cyclotron frequency. 2019. BAPS.2019.DPP.TO8.6.

[173] G. Watson and W. W. Heidbrink. Density interferometer using the fast Alfvén wave. *Review of Scientific Instruments*, 74(3):1605–1608, Mar. 2003.

[174] G. W. Watson. *Ion Species Mix and Ion Density Measurements Using Radio Frequency Waves*. PhD thesis, 2003.

[175] G. W. Watson, W. W. Heidbrink, K. H. Burrell, and G. J. Kramer. Plasma species mix diagnostic using ion–ion hybrid layer reflectometry. *Plasma Phys. Control. Fusion*, 46(3):471–487, Mar. 2004.

[176] J. A. Wesson. *Tokamaks*. Oxford University Press, fourth edition, 2011.

[177] S. Yamamoto, K. Itoh, A. Fukuyama, and S.-I. Itoh. Plasma heating by multiple-short-pulse neutral beams. In *Plasma Physics and Controlled Nuclear Fusion Research*, page 665, Sept. 1984.

[178] Y. Yu, X. Wei, P. Liu, and Z. Lin. Verification of a fully kinetic ion model for electromagnetic simulations of high-frequency waves in toroidal geometry. *Physics of Plasmas*, 29(7):073902, July 2022.

[179] A. Zalzali. *Simulations of ion cyclotron emission from energetic ions in DIII-D tokamak plasmas*. PhD thesis, University of Warwick, submitted.

[180] A. I. Zalzali, K. E. Thome, R. O. Dendy, S. C. Chapman, B. Chapman, and J. W. S. Cook. In *47th EPS Conference on Plasma Physics*, June 2021. P4.1002.

[181] L. Zeng, G. Wang, E. J. Doyle, T. L. Rhodes, W. A. Peebles, and Q. Peng. Fast automated analysis of high-resolution reflectometer density profiles on DIII-D. *Nuclear Fusion*, 46(9):S677–S684, Aug. 2006.

[182] C. D. Zhou and R. Betti. A measurable Lawson criterion and hydro-equivalent curves for inertial confinement fusion. *Physics of Plasmas*, 15(10):102707, Oct. 2008.

Appendix A

Acronyms

1D3V One spatial dimension, three velocity dimensions

ACI Alfvén cyclotron instability

AUG Asdex Upgrade tokamak (Garching, Germany)

CAE Compressional Alfvén eigenmode

ch-ICE Chirping ICE

DIII-D Doublet-IIII D tokamak (San Diego, CA USA)

DBS Dopper backscattering

EAST Experimental Advanced Superconducting Tokamak (Hefei, China)

ECCD Electron cyclotron current drive

ECE Electron cyclotron emission

ECRH Electron cyclotron resonance heating

ELM Edge localized mode

EMIC Electromagnetic ion cyclotron

EP Energetic particle

FFT Fast Fourier transform

FMW Fast magnetoacoustic wave

GAE Global Alfvén eigenmode

GTC Gyrokinetic toroidal code

HFS High-field side (of a tokamak)

IBW Ion Bernstein wave

ICE Ion cyclotron emission

ICRF Ion cyclotron range of frequencies

ICRH Ion cyclotron resonant heating

IDL Interactive Data Language code

IF Intermediate frequency

ITER ITER reactor, formerly stood for International Thermonuclear Experimental Reactor (Cadarache, France)

JET Joint European Torus (Culham, Oxfordshire, UK)

JFT-2M JAERI (Japan Atomic Energy Research Institute) Fusion Torus 2 Modified (Tokai, Japan)

JT-60(U) Japan Torus 60 (or Japan Torus 60 Upgrade) (Naka, Japan)

KAW Kinetic Alfvén wave

KSTAR Korea Superconducting Tokamak Advanced Research (Daejeon, South Korea)

LCFS Last closed flux surface

LFS Low-field side (of a tokamak)

LHCD Lower hybrid current drive

LHD Large Helical Device (Toki, Japan)

LHRF Lower hybrid range of frequencies

LO Local oscillator

LSN Lower single null

MAST Mega Ampere Spherical Tokamak (Culham, Oxfordshire UK)

MCI Magnetoacoustic cyclotron instability

MCF Magnetic confinement fusion

MSE Motional Stark effect

NBI Neutral beam injection

NIF National Ignition Facility

NSTX(-U) National Spherical Torus eXperiment (Princeton, NJ USA)

NUBEAM Computational model for neutral beam injection in tokamaks

PDI Parametric decay instability

PDX Poloidal Divertor Experiment

PIC Particle-in-cell

PLT Princeton Large Torus (Princeton, NJ USA)

RF Radiofrequency

TAE Toroidal Alfvén eigenmode

TFR Tokamak de Fontenay-aux-Roses (Fontenay-aux-Roses, France)

TFTR Tokamak Fusion Test Reactor (Princeton, NJ USA)

TRANSP 1.5D equilibrium and transport solver for tokamaks

TUMAN-3M tokamak (St. Petersburg, Russia)

USN Upper single null

VNA Vector network analyzer

WS-7A Wendelstein 7-A stellarator (Greifswald, Germany)

Appendix B

GAE heuristic toroidal mode number

Given the observed mode frequencies, we can estimate the expected range of toroidal mode numbers for GAEs from the two-fluid dispersion relation for shear waves, which can be written as [104, 153]:

$$N^2 = \frac{AG}{2F^2}\left[1 + \sqrt{1 - \frac{4F^2}{AG^2}}\right] \tag{A1}$$

where $A = 1/(1 - {}^{\omega^2}/_{\omega_{ci}^2})$, $F^2 = {}^{k_\parallel^2}/_{k^2}$, and $G = 1 + F^2$. Assuming that $k_\parallel \approx k_\varphi = {}^{n}/_{R}$, justified by simulations that have consistently found $|n| \gg {}^{|m|}/_{q}$ for sub-cyclotron modes [11, 10], and defining the parallel Alfvén index of refraction as $N_\parallel = {}^{|k_\parallel| v_A}/_{\omega}$, the toroidal mode number for counter-propagating waves is given by:

$$n \approx -\frac{R\omega}{v_A} N_\parallel \left(\omega/\omega_{ci}, |k_\parallel|/k_\perp\right). \tag{A2}$$

The dependence on the wave vector direction can be accounted for by taking the $|k_\parallel|/k_\perp \to 0$ and $|k_\parallel|/k_\perp \to \infty$ limits of Eq. A1 (since $N_\parallel$ is an increasing function of this parameter), yielding lower and upper bound estimates for n that include the effects of finite ${}^{\omega}/_{\omega_{ci}}$ for

counter-propagating GAEs:

$$-\frac{R\omega}{v_A}\frac{1}{\sqrt{1-{}^{\omega}/_{\omega_{ci}}}} < n < -\frac{R\omega}{v_A}\frac{1}{\sqrt{1-{}^{\omega^2}/_{\omega_{ci}^2}}} \tag{A3}$$

In the single fluid limit, finite frequency corrections would be neglected and Eq. A3 would simplify to $n \approx -{}^{R\omega}/_{v_A}$. However, these corrections can be relevant due to the large observed frequencies for GAEs in DIII-D (${}^{f}/_{f_{ci}} \sim 0.5$); hence, it is preferred that the range provided by Eq. A3 be calculated instead. For estimated ranges discussed in Sec. 4.4, we assume that R, v_A, and ω_{ci} are taken to be at the magnetic axis (for these plasmas, $R = 1.72$ m).

However, making similar heuristic estimates for ICE is more challenging. If ICE can be modeled as a CAE, then the two-fluid dispersion relation implies ${}^{\omega}/_{v_A} \geq k \geq |k_\varphi| = {}^{|n|}/_{R}$, such that $|n| < {}^{\ell\omega_{cb}R}/_{v_A}$, where it is assumed that the ICE frequency occurs at integer multiples ℓ of the beam ion cyclotron frequency, ω_{cb}. In practice though, this expression gives a very loose bound that is not useful in constraining the experimental analysis (evaluated here using $R = 1.73$ m and $n_e \sim 2.6 \times 10^{-19}$ m^{-3} near the magnetic axis for the case depicted in Fig. 4.13, it gives $|n| \lesssim 27\ell$). Conversely, no lower bound can be placed on $|n|$ since $N_\parallel$ can be made arbitrarily small in the limit of $|k_\parallel| \ll k_\perp$ for CAEs.

Although not needed for this analysis, it is worth noting that toroidal mode numbers for GAEs can also be estimated *a priori*, even before measurements of the mode frequency have been made, by invoking the resonance condition and linear stability considerations. The Doppler-shifted cyclotron resonance condition, neglecting the drift term (e.g., assuming $|k_\perp v_{\text{drift}}| \ll |k_\parallel v_\parallel|$), can be written as:

$$\omega - k_\parallel v_\parallel = \ell\omega_{cb}. \tag{A4}$$

Here, ω_{cb} is the beam ion cyclotron frequency and we have adopted the convention that

$\omega > 0$ and $v_\parallel > 0$, with the sign of $k_\parallel$ being defined relative to the direction of beam injection. Combining Eq. A2 and Eq. A4 yields:

$$n \approx \frac{\ell R \omega_{cb}}{v_A} \frac{1}{\sigma/N_\parallel - v_\parallel/v_A} \tag{A5}$$

where $\sigma = \text{sign}(k_\parallel)$. For counter-propagating modes, such as those previously seen on DIII-D [161], $\sigma = -1$ and thus, to satisfy the resonance condition, $\ell = 1$. Eq. A5 then becomes:

$$n \approx -\frac{R \omega_{cb}}{v_A} \frac{1}{1/N_\parallel + v_\parallel/v_A} \tag{A6}$$

Thus, knowledge of the mode frequency (needed to evaluate Eq. A2) has been replaced by an assumption on the value of $v_\parallel$ for the resonant fast ions. Linear stability theory dictates that typically the largest fast ion drive occurs for counter-propagating modes when $v_\parallel \approx v_b(v_\parallel/v)$, where v_b is the beam injection velocity and $v_\parallel/v$ is the pitch that the distribution is centered around (determined by a code such as NUBEAM, or estimated from the beam tangency radius). This condition gives the resonant contour that includes the most particles while guaranteeing that they all contribute drive, not damping, due to the sign of $\partial f_b/\partial(v_\parallel/v)$ [104, 12]. The same upper and lower bounds of $N_\parallel$ as before can be taken to arrive at the following estimate for the "most unstable" value of n, which is entirely equivalent to Eq. A3 combined with Eq. A4:

$$-\frac{R \omega_{cb}}{v_A} \frac{1}{\sqrt{1 - \omega/\omega_{ci}} + v_\parallel/v_A} < n < -\frac{R \omega_{cb}}{v_A} \frac{1}{\sqrt{1 - \omega^2/\omega_{ci}^2} + v_\parallel/v_A} \tag{A7}$$

Unlike for sub-cyclotron modes, the resonance condition is not helpful as a further constraint for ICE for two reasons. First, though the majority of ICE measurements have been made with magnetic pickup loops at the wall, ICE is assumed to occur very close to the harmonics of ω_{cb} at some location in the plasma, neglecting Doppler shifts. As such, the size of $k_\parallel$ implied by Eq. A4 is very sensitive to the value of ω_{cb} assumed for resonant particles on the

right-hand side, which depends on their orbits. For instance, if ω_{cb} were assumed to precisely match that of the emission location, Eq. A4 would imply $k_{\|} = {}^{(n-m/q)}/_{R} = 0$, which would require an assumption on the size of m in order to predict n (for GAEs, it was assumed that $|m| \ll |n|$). Second, theoretical literature on ICE posits that $|k_{\|}| \ll k_{\perp}$ is strongly preferred by the instability [51]. In that case, the drift term ($k_{\perp} v_{drift}$) previously neglected in Eq. A4 could be comparable to the parallel resonant Doppler shift ($k_{\|} v_{\|}$), and then the implied value of n would also depend on the unknown ratio of ${}^{k_{\|}}/_{k_{\perp}}$. Consequently, there are currently no simple and reliable heuristic estimates of the expected ICE mode numbers, beyond the loose bound discussed above. Hence, cross-validation with planned simulations of ICE in full tokamak geometry is a high priority for future work.

Appendix C

Initial high-frequency ICE measurements

HICE was implemented for initial conditioning of and assessing coupling for the high-power helicon system on DIII-D that took place in June of 2021 [131, 168, 167]. In these experiments, $n_{\parallel} = 3$, 476 MHz helicon waves ranging from $5 \sim 320$ kW were injected via a traveling wave system [167] into LSN L-mode plasmas, which had roughly $I_P = 0.98$ MA, $B_T = 2.0$ T, $n_e \sim 2.3 \times 10^{13}$ cm^{-3}, and $q_{95} \sim 4.85$ (example shot depicted in Fig. C.1). These plasmas were primarily heated with a combination of NBI and ECRH power, the former providing roughly 2.5 MW (via co-I_P, on-axis, near-tangential beams at 30° and 330°) and the latter ranging from 0.6–1.3 MW. NBI and helicon were heavily modulated throughout the experiment.

The HICE configuration used in these experiments was shown in chapter 3.4 and is depicted in an aerial view in Fig. C.1. The signal from both a centerpost loop at 262° and a long outer wall loop at 247.5° were each split and their high-frequency signals mixed down from the 400–500 MHz range before being digitized. The default 1–100 MHz range signals were also digitized to probe for waves excited in the ion cyclotron range of frequencies, alongside

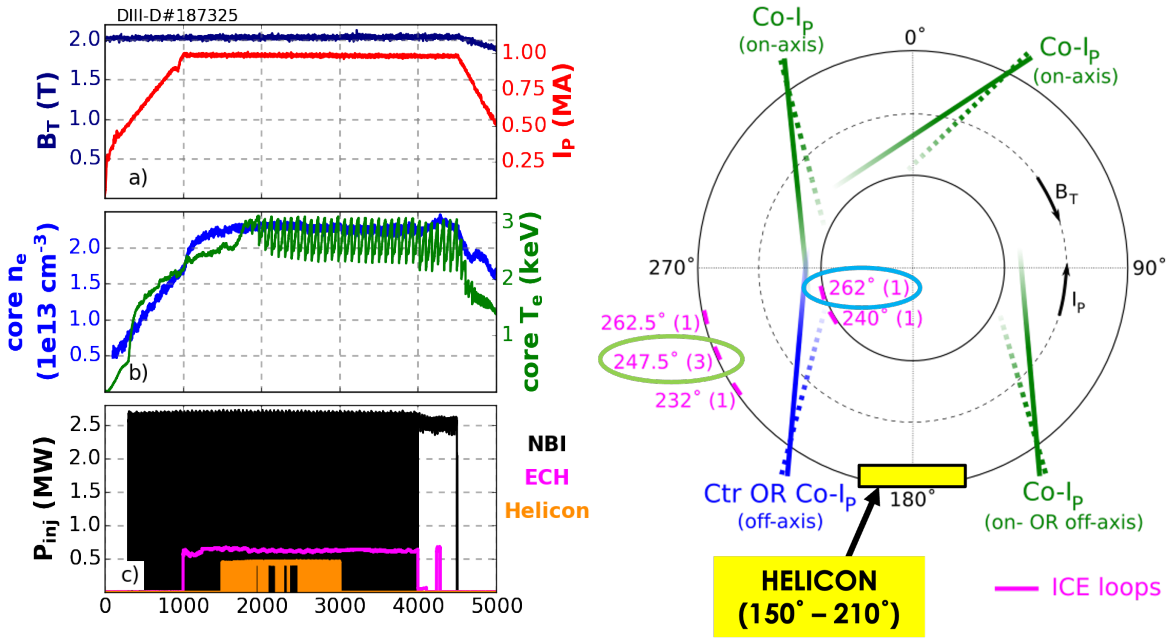

Figure C.1: Left: a) B_T (navy) and I_P (red), b) line-integrated n_e in the core (blue) and a core ECE channel indicating temperature (green), and c) injected power via NBI (black) and ECH (magenta) alongside forward helicon power (orange) for an example L-mode shot in these conditioning experiments. Right: Aerial view of DIII-D with the loops used for the HICE configuration highlighted by light green and blue circles, and the location of the helicon antenna marked in yellow near 150–210°.

signal from another long toroidal loop at 262° in the default range for comparison. Prior testing determined that helicon signal injected at $\lesssim$ 500 kW did not pose a substantial risk to the ICE/HICE system, so no attenuators were used for these particular experiments.

The injected helicon wave was clearly visible in the 400–500 MHz window throughout the experiments when forward power was applied, as depicted in Fig. C.2. Peaks roughly $\lesssim$ 5 MHz in width were observed alongside the injected helicon wave, centered about 476 MHz and occurring at intervals corresponding to f_{ci} of deuterium as evaluated at the midplane LCFS. These modes were observed both by the centerpost and outer wall loops, with the centerpost loop overall recording lower amplitudes for both the injected wave and associated sidebands. No peaks were present in this frequency range in the absence of helicon power, as seen in Fig. C.2.

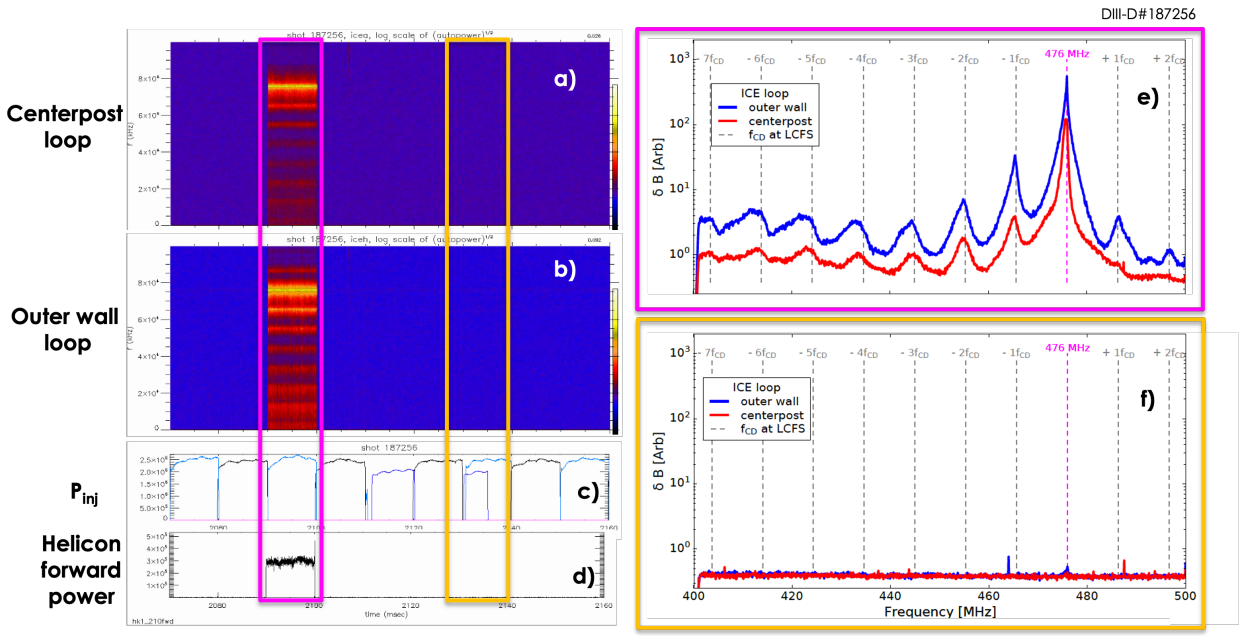

Figure C.2: a) Centerpost and b) outer wall autopower signals in the 400–500 MHz frequency range during periods where the NBI power was comparable (c) but the helicon signal was (magenta outlines) and was not (gold outlines) injected (d). These signals were time-averaged over these magenta and gold-outlined intervals in (e) and (f).

The spacing of these peaks changed with B_T as it was lowered from 2.0 T (blue in Fig. C.3) to 1.85 T (red), but the number and rough width of the peaks did not. In both cases, there appeared to be more modes excited on the lower side of the injected helicon signal, extending down to roughly 476 - $6f_{ci}$ = 406 MHz. N.B.: the time-averages of peaks in 400–500 MHz range are pictured and limited to the digitizer bandwidth of roughly 1–100 MHz, but many peaks below 476 MHz were excited, extending all the way down to the default 1–100 MHz ICE range, as seen in Fig. C.4(b)). Above 476 MHz, there appeared to be only two modes excited in this 400–500 MHz window, with their amplitudes rapidly decreasing as frequency increased from 476 MHz. The shape, and necessarily the size of the evanescent layer at the midplane (which has been seen to affect observed mode amplitudes in other high-frequency experiments on DIII-D [81]), did not change between these two shots.

To probe sideband mode dependence on the amplitude of the injected helicon wave, a scan

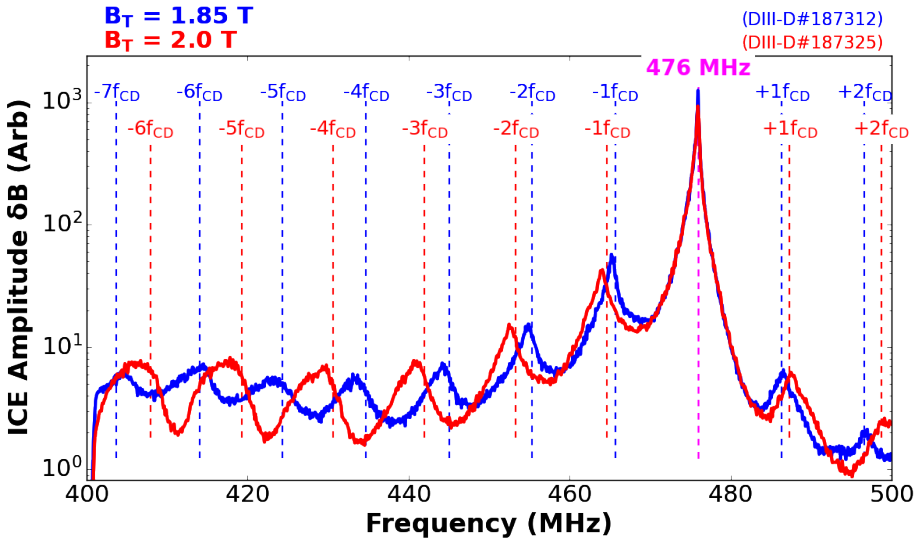

Figure C.3: Time-averaged HICE data from the outer wall loop probe during a helicon pulse with roughly 315 kW of forward power into plasmas with B_T of 2.0 (blue) and 1.85 T (red).

of helicon forward power was conducted over the course of four consecutive shots[1]. The resulting HICE time-averaged data is shown in Fig. C.4a), where very similar modes were excited for forward powers of 317 and 272 kW. There was a significant drop in forward helicon power to 30 and then 5 kW in the last two plasmas in the scan, and while sideband amplitudes in this range depreciated substantially, a clear peak at $476-1f_{ci}$ remained in both cases. In the default 1–100 MHz range (Fig. C.4(b)), there was not such an obvious decrease in the sidebands that were spaced according to f_{ci} at the LCFS, save for peaks at 1 and $2f_{ci}$, which have higher amplitudes at the higher forward helicon powers and then largely disappear at 30 and 5 kW. There also seems to be a narrowband mode excited $2f_{ci}$ corresponding to the magnetic axis, whose amplitude also diminishes with decreasing forward helicon power. This particular mode is suspected to be a fast ion-driven mode and is the subject of future study [160]. As was the case in the B_T comparison in Fig. C.3, neither the plasma shape nor the spacing between the plasma and the outer wall change in any of these

[1]Unfortunately, the last forward power value of 5.2 kW was in a dangerous regime for the vacuum feedthrough and significant multipacting resulted in substantial arcing shortly after injection began. The feedthrough was damaged, resulting in the immediate cessation of the experiment and no further values for the power scan depicted in Fig. C.4. Data in shot DIII-D#187328 was averaged over the course of a few ms before arcing.

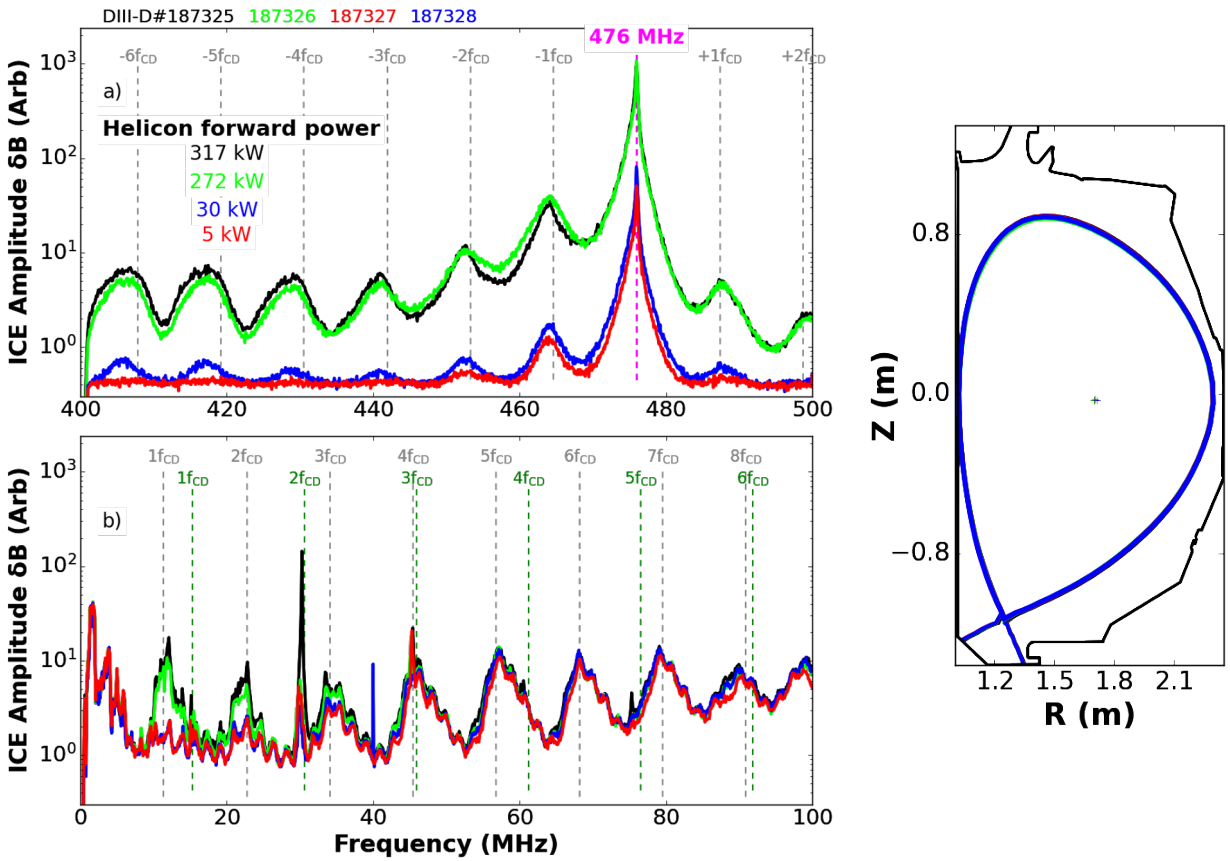

Figure C.4: Left: Time-averaged HICE data from outer wall loop probe during a pulses with 317 kW (black), 272 kW (lime green), 30 kW (blue), and 5 kW (red) of forward helicon power in $B_T = 2.0$ T plasmas. a) 400–500 MHz range, where $f_{CD} \simeq 11.4$ MHz is the deuterium cyclotron frequency calculated at the midplane LCFS and marked in gray. b) 1–100 MHz range, where additional green dashed lines mark the deuterium cyclotron frequency evaluated at the magnetic axis. Right: Equilibrium reconstructions for each shot corresponding to the start of the time windows evaluated in the figure at left, where the blue shape is the last shot in the scan and overlaps the others.

shots, as illustrated by the overlapping shapes in the right-most pane in Fig. C.4.

Finally, though these conditioning experiments centered primarily around L-mode plasmas, H-mode was briefly accessed and helicon was injected during this time. Fig. C.5 depicts signal from the centerpost loop in the 400–500 MHz frequency range, where the usual helicon signal and associated sidebands were observed and were very similar to the peaks observed in the absence of a pedestal. However, the concomitant ELMs (as pictured in the D-α signal in Fig. C.5(c)) disturbed the spectra briefly before the original signal is restored. The

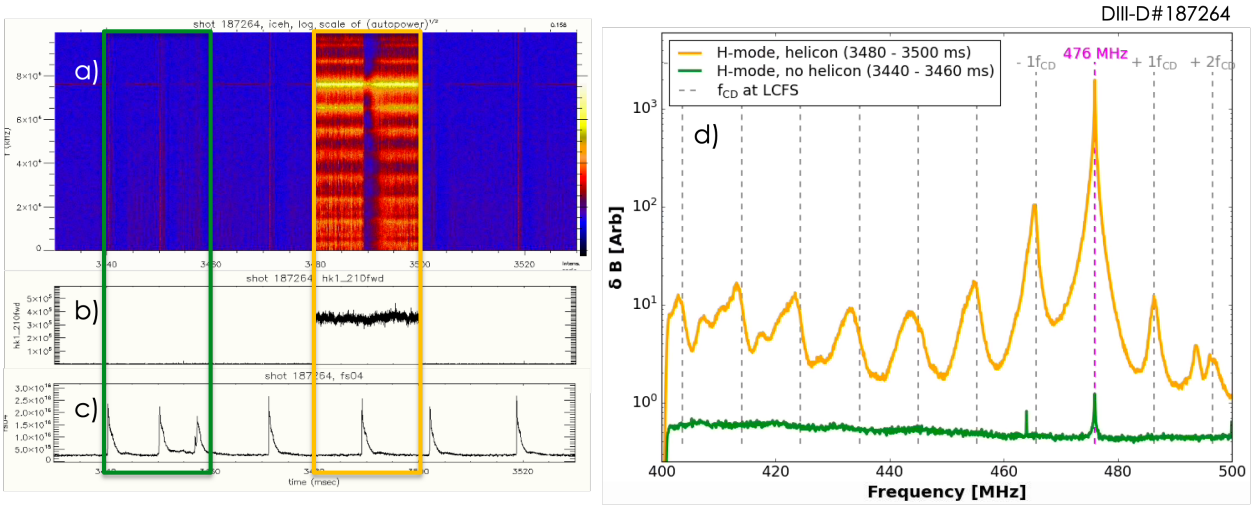

Figure C.5: (a) Autopower spectra from the outer wall loop during the H-mode period in DIII-D#187264, with forward helicon power depicted in (b) and D-α signal in (c). The autopower data averaged over time windows during negligible (green) and ∼350 kW (gold) of helicon forward power are presented in (d).

ELMs unsurprisingly did not affect the observed helicon peak at 476 MHz, but the sidebands' significantly depreciated in amplitude in the case of sidebands at -1 and -2f_{ci}, or disappeared completely.

This preliminary data was used as the basis for predictions of parametric decay instability (PDI) excitation and helicon edge absorption studies [133, 132]. PDI, in conjunction with lower frequency fast ion modes excited by helicon injection, are the subject of ongoing study [31, 160] as the helicon injection system is developed and used at full power (∼1 MW) in the next few years on DIII-D.